Transmission-Line Based Metamaterials in Antenna Engineering

Marco A. Antoniades, Hassan Mirzaei, and George V. Eleftheriades

Contents

M.A. Antoniades (✉)
Department of Electrical and Computer Engineering, University of Cyprus, Nicosia, Cyprus
e-mail: mantonia@ucy.ac.cy

H. Mirzaei • G.V. Eleftheriades
The Edward S. Rogers Sr. Department of Electrical and Computer Engineering, University of Toronto, Toronto, ON, Canada
e-mail: hasmir@ece.utoronto.ca; gelefth@waves.utoronto.ca

Z.N. Chen et al. (eds.), *Handbook of Antenna Technologies*,
DOI 10.1007/978-981-4560-44-3_21

Abstract

In this chapter, transmission-line-based metamaterials are presented, and their application to the design of passive and active antennas is outlined. Transmission-line metamaterials, also termed negative-refractive-index transmission-line (NRI-TL) metamaterials, are formed by periodically loading a transmission line with lumped-element series capacitors and shunt inductors, and it is shown that they can support both forward and backward waves, as well as standing waves with a zero propagation constant. These rich propagation characteristics form the underlying basis for their use in many antenna applications, including leaky-wave antennas, compact resonant antennas, and multiband antennas. The resonant characteristics of the NRI-TL metamaterial structures reveal how these structures can be designed to offer multiband responses whose resonant frequencies are not harmonically related while offering large degrees of miniaturization. Design equations for rapid prototyping are presented, enabling the simple design of metamaterial antennas to a given specification using standard microwave substrates and loading elements in either fully printed form or surface-mount chip components. A number of passive metamaterial antenna applications are presented, including examples of zeroth-order resonant antennas, negative-order resonant antennas, epsilon-negative antennas, mu-negative antennas, metamaterial dipole antennas, and metamaterial-inspired antennas. Active non-Foster matching networks for small antennas are also presented using negative impedance converters (NICs) and negative impedance inverters (NIIs), and it is demonstrated how these can be applied to metamaterial-inspired antennas. Finally, a new method of implementing reactive non-Foster elements using loss-compensated negative-group-delay (NGD) networks is presented that exhibits improved stability, dispersion, and achievable bandwidth.

Keywords

Negative-refractive-index transmission line (NRI-TL) • Metamaterials • Electrically small antennas • Compact antennas • Resonant antennas • Planar antennas • Multiband antennas • Dispersion engineering • Composite right-/left-handed (CRLH) materials • Active antennas • Active non-Foster matching networks • Negative impedance converters • Negative impedance inverters

Introduction

The emergence of a new class of engineered electromagnetic materials, known as negative-refractive-index (NRI) metamaterials, realized using either split-ring resonators and wires or reactively loaded transmission lines, has generated great interest

within the electromagnetics community, for their potential to create new devices that exhibit altogether new phenomena or improved performance characteristics compared to their conventional counterparts.

The term NRI derives from the fact that these materials can have simultaneously negative material parameters (permittivity ϵ and permeability μ), and therefore a negative-refractive index, and as such they exhibit phenomena that are not readily encountered in nature, hence the prefix "meta." More generally, the material parameters can be engineered to have positive, negative, and zero values by what is known as "dispersion engineering." Furthermore, by controlling the material parameters as a function of space, this allows the electric and magnetic fields, and therefore the power flow, to be arbitrarily directed within a structure, which has opened up an entirely new field of "transformation optics" (Pendry et al. 2006). Some examples of unusual phenomena that have been obtained using metamaterials are the creation of a completely flat perfect lens (Pendry 2000), sub-wavelength resolution imaging beyond the diffraction limit (Grbic and Eleftheriades 2004), electromagnetic cloaking (Pendry et al. 2006; Zedler and Eleftheriades 2011), and backward-wave and broadside radiation from a planar leaky-wave structure (Grbic and Eleftheriades 2002; Iyer and Eleftheriades 2004).

The recent growth in metamaterial research has also resulted in an analogous increase in the amount of publications in this area. Notable among these are several books that have been published recently on metamaterials, each with a different focus (Eleftheriades and Balmain 2005; Engheta and Ziolkowski 2006; Caloz and Itoh 2006; Marques et al. 2007; Capolino 2009; Cui et al. 2010), and several antenna-related textbooks and handbooks that contain dedicated sections on metamaterials (Balanis 2008, 2012; Volakis 2007; Volakis et al. 2010). In general, metamaterials can be designed for either guided-wave applications (e.g., phase shifters, couplers, power dividers, resonators, etc.) or radiating applications (leaky-wave antennas, small resonant antennas, and active variants of these). The focus of this contribution is on *transmission-line*-based metamaterials, as these pertain to the design of passive and active resonant antennas.

The *transmission-line* approach to synthesizing NRI metamaterials relies on periodically loading conventional microwave transmission lines with lumped-element series capacitors and shunt inductors. This approach was introduced in Eleftheriades et al. (2002), Antoniades and Eleftheriades (2003), Caloz and Itoh (2003), and Sanada et al. (2004), and subsequently the materials were termed negative-refractive-index transmission-line (NRI-TL) metamaterials to reflect the fact that a negative-refractive index can be achieved by reactively loading a host transmission line. An example of such a two-dimensional NRI-TL metamaterial unit cell is shown in Fig. 1.

NRI-TL metamaterials have since proven to be very practical due to their planar nature and the large negative-index bandwidth and low transmission losses that can be achieved. Furthermore, as will be subsequently shown in this chapter, NRI-TL metamaterials exhibit propagation characteristics with alternating stopbands and passbands, supporting backward waves in the left-handed band (NRI region),

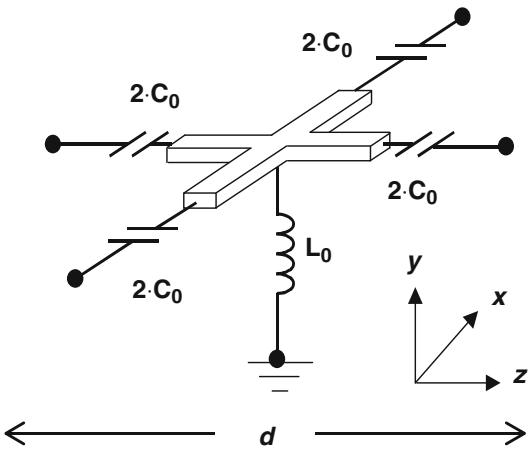

Fig. 1 Two-dimensional NRI-TL metamaterial unit cell (Iyer et al. 2003). © 2003 OSA

forward waves in the right-handed band (positive-refractive-index (PRI) region), and standing waves with a zero propagation constant between the left-handed and right-handed bands. These versatile propagation characteristics are a key element for the use of NRI-TL metamaterials in the design of multiband antennas, enabling the creation of tailored frequency responses. They also enable a large degree of miniaturization by exploiting the fact that the obtained zero propagation constant is independent of the length of the structure and the fact that in the backward-wave region, the propagation constant is inversely proportional to the frequency. The transmission-line approach to synthesizing NRI-TL metamaterials has also proven to be very useful for the integration of NRI-TL devices and antennas with other circuits on the same substrate, since they have a completely planar form factor.

Here, it should be noted that due to the relatively recent development of metamaterials, there are different terminologies that are used in the literature to denote these materials. Transmission-line based metamaterials have also been termed composite right-/left-handed (CRLH) materials (Lai et al. 2004), a terminology that reflects both their left-handed and right-handed propagation characteristics. Other designations for NRI media in which the effective permittivity and permeability are simultaneously negative include double-negative (DNG) media (Engheta and Ziolkowski 2006) and left-handed media (LHM) (Veselago 1968). Furthermore, single-negative (SNG) media denote media where one of the material parameters is negative and include two variants: epsilon-negative (ENG) media, where the permittivity ϵ is negative, and mu-negative (MNG) media where the permeability μ is negative. Finally, for epsilon-near-zero (ENZ) and epsilon-zero (EZR) media, the permittivity ϵ is near zero and zero, respectively, while for mu-near-zero (MNZ) and mu-zero (MZR) media, the permeability is near zero and zero, respectively.

Negative-Refractive-Index Transmission-Line Theory

NRI-TL Metamaterial Structure

In order to understand the operation of resonant antennas based on transmission-line metamaterials, the propagation and impedance properties of one-dimensional NRI-TL metamaterials will first be outlined. This allows the visualization of the different antenna modes that these metamaterials have to offer, while providing simple design equations for the design of single-band and multiband resonant antennas.

The one-dimensional NRI-TL metamaterial phase-shifting line shown in Fig. 2 has been constructed by periodically loading a host transmission line with a characteristic impedance of Z_0 with series capacitors C_0 and shunt inductors L_0. Here, $Z_0 = \sqrt{L/C}$, where L and C are the per unit length inductance and capacitance of the transmission line. It can be designed to occupy an arbitrary length and to provide an arbitrary phase shift, and has an inherent phase-compensating nature. This is because it incorporates both a transmission-line component with an equivalent low-pass topology that contributes a negative phase shift and a backward-wave component with a high-pass topology that contributes a positive phase shift.

The phase-shifting line consists of identical repeating symmetrical unit cells, where each of these unit cells can be considered to be a small NRI-TL metamaterial phase-compensating structure. Figure 3 shows two possible implementations of the elementary phase-compensating NRI-TL metamaterial unit cell; the T configuration was developed in Eleftheriades et al. (2002) and Antoniades and Eleftheriades (2003) and the Π configuration was subsequently developed in Elek and Eleftheriades (2005). It can be recognized that the T and Π unit cells are simply

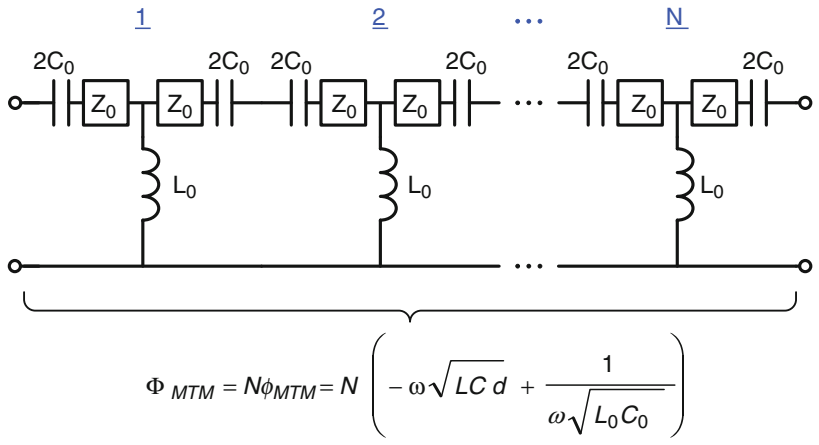

Fig. 2 *N*-stage NRI-TL metamaterial phase-shifting line

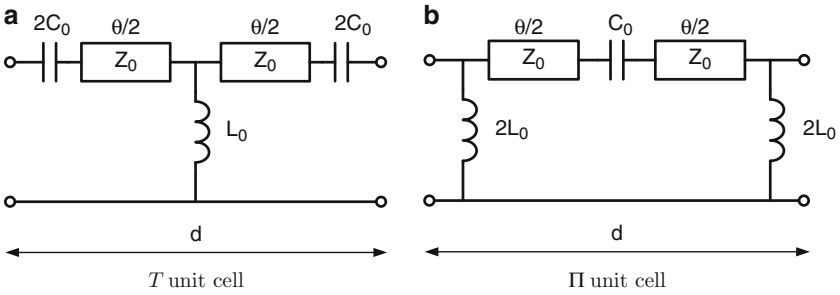

Fig. 3 NRI-TL metamaterial unit cells

related by a shift of the reference planes defining each unit cell within the larger periodic structure shown in Fig. 2. As such, it is expected that their propagation characteristics will be identical, something which will be subsequently verified in the following section. The *T* unit cell has a host transmission line with characteristic impedance Z_0 and length d that is loaded with two series capacitors $2C_0$ and a shunt inductor L_0, while the Π unit cell has a host transmission line also with characteristic impedance Z_0 and length d that is loaded with one series capacitor C_0 and two shunt inductors $2L_0$. The choice of which topology to use for a particular design mainly depends on the intended application and the technology in which the circuits are realized. Implementations of both unit cells will be shown in the section "Antenna Design Using TL-Metamaterials" for both microstrip and coplanar waveguide designs.

Propagation and Impedance Characteristics of the *T* Unit Cell

The propagation characteristics of a metamaterial line that consists of identical symmetric unit cells can be determined by conducting a periodic Bloch-Floquet analysis (Collin 1992) on each unit cell in Fig. 3. The details of the periodic analysis can be found in Antoniades (2004, 2009), and the key results are summarized here as these relate to the design of phase-shifting lines for antenna applications.

The dispersion relation for a periodic structure comprising an infinite number of metamaterial *T* unit cells as shown in Fig. 3a is

$$\cos(\beta_{\mathrm{BL}} d) = \left(1 - \frac{1}{4\omega^2 L_0 C_0}\right)\cos(\theta) + \left(\frac{1}{2\omega C_0 Z_0} + \frac{Z_0}{2\omega L_0}\right)\sin(\theta) - \frac{1}{4\omega^2 L_0 C_0}. \tag{1}$$

Here, β_{BL} is the Bloch propagation constant for the periodic structure with periodicity d, as shown in Fig. 3. The Bloch propagation constant therefore provides a complete picture of the propagation characteristics of the periodic structure, which are typically displayed as a function of frequency on a dispersion diagram.

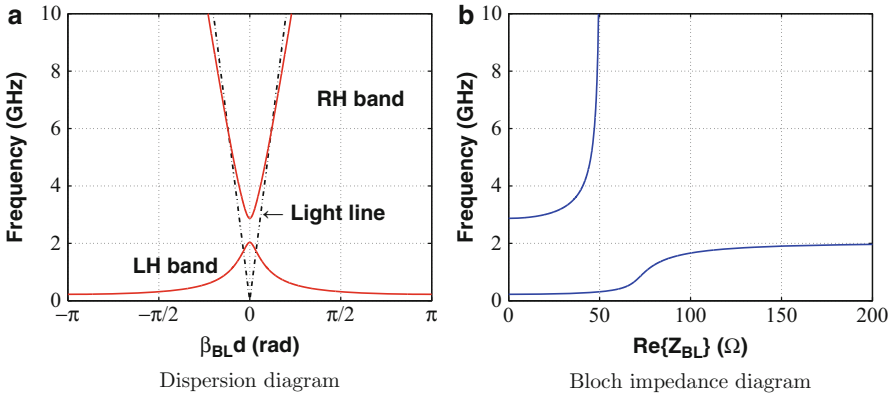

Fig. 4 Characteristics of a representative NRI-TL metamaterial T unit cell with parameters $C_0 = 5$ pF, $L_0 = 25$ nH, $Z_0 = 50$ Ω, $d = 3$ mm, and $\theta = 8.8°$ at 2 GHz. Note that in this case, $Z_{0,\mathrm{BW}} = \sqrt{L_0/C_0} > Z_0$

A representative dispersion diagram obtained using Eq. 1 is shown in Fig. 4a. It can be observed that the propagation characteristics of the structure exhibit alternating passbands and stopbands. The two passbands that are of interest are the lower left-handed (LH) band which supports backward waves and the upper right-handed (RH) band which supports forward waves. The light line is also shown in Fig. 4a, which demarcates the transition between slow-wave and fast-wave propagation. Therefore, the metamaterial structure supports backward and forward waves that can be either slow or fast. This indicates that the metamaterial can be used for either guided-wave applications in the slow-wave regions outside of the light cone (Islam and Eleftheriades 2007, 2012; Eleftheriades 2007; Lai et al. 2004) or leaky-wave antenna applications in the fast-wave region within the light cone (Antoniades and Eleftheriades 2008a; Mehdipour and Eleftheriades 2014; Hashemi and Itoh 2011). Furthermore, at the two frequency points where $\beta_{\mathrm{BL}}d = 0$, the metamaterial can also be used for resonant antenna applications. These, and additional resonant modes that can be excited on this structure, will be outlined in the section "Antenna Design Using TL-Metamaterials."

The characteristic impedance of the periodic structure, known as the Bloch impedance, is defined at the terminals of each unit cell and has positive and negative solutions, which correspond to the forward and reflected traveling waves, respectively. It should be noted that the Bloch impedance of a periodic structure is not unique and will depend on the location of the reference planes for each unit cell. Therefore it is expected that the two metamaterial unit cells of Fig. 3 will have different Bloch impedances. The Bloch impedance for the periodic structure comprising an infinite number of T metamaterial unit cells can be written as

$$Z_{\mathrm{BL,T}} = \pm \sqrt{\frac{\left(Z + \frac{Z^2 Y}{8} + \frac{YZ_0^2}{2}\right)\cos(\theta) + \frac{j}{2}\left(\frac{Z^2 Y_0}{2} + YZZ_0 + 2Z_0\right)\sin(\theta) + \frac{Z^2 Y}{8} - \frac{YZ_0^2}{2}}{\frac{Y}{2}\cos(\theta) + jY_0 \sin(\theta) + \frac{Y}{2}}}, \tag{2}$$

where

$$Z = \frac{1}{j\omega C_0} \quad \& \quad Y = \frac{1}{j\omega L_0}. \tag{3}$$

A representative Bloch impedance diagram for the metamaterial T unit cell obtained using Eq. 2 is shown in Fig. 4b. It can be observed that a real Bloch impedance exists only within the passbands of the periodic structure, while within the stopbands, the Bloch impedance is imaginary. It can also be observed that the Bloch impedance exhibits a large variation throughout the left-handed band and remains around 50 Ω for a very small frequency range. As such, the metamaterial structure will exhibit the undesirable feature of a very narrow impedance bandwidth when it is matched to a 50 Ω feed line, as is frequently done for antenna applications. On the contrary, in the right-handed band, the Bloch impedance converges to a constant value of 50 Ω as the frequency increases. This is a very desirable feature that enables broadband matching of the periodically loaded metamaterial line to a feed line or a terminating load.

In the design of the metamaterial unit cells, it is interesting to note that depending on the values of the elements loading the host transmission line, the Bloch impedance characteristics can be significantly different. In order to further understand the Bloch impedance behavior, the characteristic impedance of the host transmission line Z_0 must be compared with the characteristic impedance of the backward-wave line that loads the host TL, $Z_{0,\mathrm{BW}} = \sqrt{L_0/C_0}$. For the example shown in Fig. 4 with loading-element parameters of $C_0 = 5$ pF and $L_0 = 25$ nH, the characteristic impedance of the backward-wave line is $Z_{0,\mathrm{BW}} = 70.7$ Ω, which is greater than the characteristic impedance of the host transmission line, $Z_0 = 50$ Ω. Considering now the case where $Z_{0,\mathrm{BW}}$ is less than Z_0, the values of $C_0 = 15$ pF and $L_0 = 25$ nH are chosen, resulting in $Z_{0\ \mathrm{BW}} = 40.8$ Ω.

The dispersion and Bloch impedance diagrams for this second case are shown in Fig. 5. Here, it can be observed that even though the general dispersion characteristics are very similar to the ones shown in Fig. 4a, the Bloch impedance characteristics have changed significantly. Within the lower left-handed band, the Bloch impedance no longer passes through the 50 Ω point, but rather attains a maximum value of only 39 Ω, indicating that it is impossible to match the metamaterial line to 50 Ω within the lower left-handed band. This is an important consideration that should be taken into account when designing metamaterial lines using *T* unit cells with $Z_{0,\mathrm{BW}} < Z_0$. If, however, it is desired to match the line to 50 Ω within the upper right-handed band, then the *T* unit cell with $Z_{0,\mathrm{BW}} < Z_0$ is still an attractive option.

It can therefore be concluded that in order to obtain a Bloch impedance diagram of the form shown in Fig. 4b, where the metamaterial line consisting of *T* unit cells

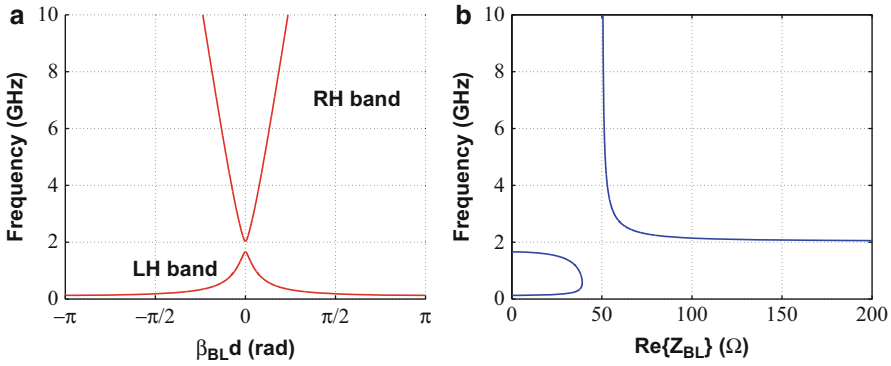

Fig. 5 Characteristics of a representative NRI-TL metamaterial T unit cell with parameters $C_0 = 15$ pF, $L_0 = 25$ nH, $Z_0 = 50\ \Omega$, $d = 3$ mm, and $\theta = 8.8°$ at 2 GHz. Note that in this case, $Z_{0,\mathrm{BW}} = \sqrt{L_0/C_0} < Z_0$

can be matched to a specific impedance (in this case $Z_0 = 50\ \Omega$) in both the lower left-handed and the upper right-handed bands, then the following condition must be satisfied:

$$Z_{0,\mathrm{BW}} > Z_0 \quad \text{or} \quad \sqrt{\frac{L_0}{C_0}} > \sqrt{\frac{L}{C}}. \tag{4}$$

Relation to Compact Resonant Antennas

One might wonder how the analysis of an infinitely long periodic structure relates to the design of compact, resonant antennas that typically would consist of only a few unit cells. The answer lies in the fact that even though the above analysis was carried out assuming an infinitely long periodic structure, the propagation and impedance characteristics can be retained even for a finite structure, by simply terminating it on both ends in its Bloch impedance. This eliminates any reflections at the source and load and allows the propagating waves along the line to effectively see an infinite periodic medium. The periodic structure can therefore be made arbitrarily small, and in the extreme case it can consist of a single unit cell, without affecting its propagation and impedance characteristics, simply by ensuring that it is excited and terminated in its Bloch impedance. For compact antennas, which are inherently one-port devices, the terminating impedance condition can be achieved by designing the structures such that the radiation resistance is as close as possible to the Bloch impedance, which for typical antennas is chosen to be 50 Ω. As will be seen in the section "Antenna Applications of TL-Metamaterials," antenna designs based on transmission-line metamaterials enable a high radiation resistance close to 50 Ω to be achieved even for very-low-profile antennas, which also translates into the additional benefit of providing a high radiation efficiency.

Propagation Characteristics of the Π Unit Cell

A similar procedure can be carried out for the analysis of the metamaterial Π unit cell of Fig. 3b. It has been found that the dispersion characteristics of the Π unit cell are identical to those of the T unit cell and are also given by Eq. 1 (Antoniades 2009). The Bloch impedance of the metamaterial Π unit cell is given by

$$Z_{\mathrm{BL},\Pi} = \pm \sqrt{\frac{\frac{Z}{2}\cos(\theta) + jZ_0 \sin(\theta) + \frac{Z}{2}}{\left(Y + \frac{ZY^2}{8} + \frac{ZY_0^2}{2}\right)\cos(\theta) + \frac{j}{2}\left(\frac{Y^2 Z_0}{2} + YZY_0 + 2Y_0\right)\sin(\theta) + \frac{ZY^2}{8} - \frac{ZY_0^2}{2}}}, \tag{5}$$

with the same expressions for Z and Y from Eq. 3.

Representative dispersion and Bloch impedance diagrams for the metamaterial Π unit cell are shown in Fig. 6 for the case where $Z_{0,\mathrm{BW}} > Z_0$ and in Fig. 7 for the case where $Z_{0,\mathrm{BW}} < Z_0$. As expected, the dispersion characteristics of the Π unit cell for the case where $Z_{0,\mathrm{BW}} < Z_0$ shown in Fig. 7a are identical to the dispersion characteristics of the T unit cell shown in Fig. 5a. The Bloch impedance of the two unit cells also has very similar characteristics in the upper right-handed band, as can be verified from Figs. 5b and 7b. In the lower left-handed band, however, the Bloch impedance for Π unit cell with $Z_{0,\mathrm{BW}} < Z_0$ has the additional advantage that it passes through 50 Ω, thus also enabling the matching of the metamaterial line within this band. For the Π unit cell operating under the condition that $Z_{0,\mathrm{BW}} > Z_0$ shown in Fig. 6, the Bloch impedance does not pass through the 50 Ω point in the left-handed band; therefore, it is not possible to match the line to 50 Ω within this band. Thus, in

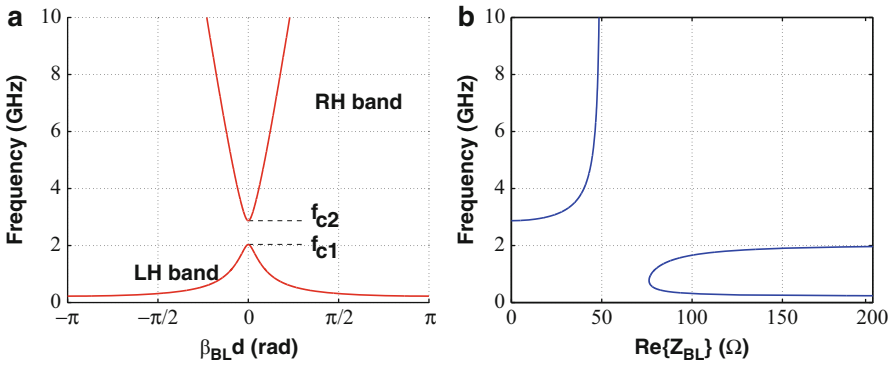

Fig. 6 Characteristics of a representative NRI-TL metamaterial Π unit cell with parameters $C_0 = 5$ pF, $L_0 = 25$ nH, $Z_0 = 50$ Ω, $d = 3$ mm, and $\theta = 8.8°$ at 2 GHz. Note that in this case, $Z_{0,\mathrm{BW}} = \sqrt{L_0/C_0} > Z_0$

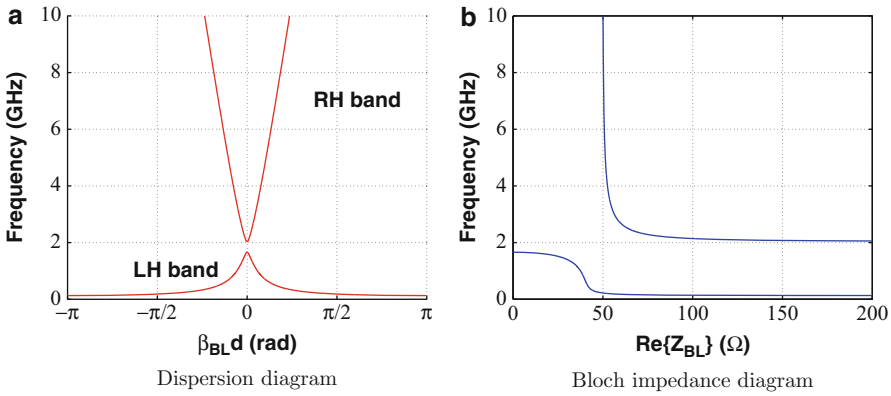

Fig. 7 Characteristics of a representative NRI-TL metamaterial Π unit cell with parameters $C_0 = 15$ pF, $L_0 = 25$ nH, $Z_0 = 50\ \Omega$, $d = 3$ mm, and $\theta = 8.8^\circ$ at 2 GHz. Note that in this case, $Z_{0,\mathrm{BW}} = \sqrt{L_0/C_0} < Z_0$

order to match the line to 50 Ω in both the left-handed and right-handed bands, the following condition for the Π unit cells must be satisfied:

$$Z_{0,\mathrm{BW}} < Z_0 \quad \text{or} \quad \sqrt{\frac{L_0}{C_0}} < \sqrt{\frac{L}{C}}. \tag{6}$$

Furthermore, the useful cases of the T unit cell with $Z_{0,\mathrm{BW}} > Z_0$ shown in Fig. 4 and the Π unit cell with $Z_{0,\mathrm{BW}} < Z_0$ shown in Fig. 7 can be compared. It can be observed that the dispersion characteristics of the Π unit cell are similar to the dispersion characteristics of the T unit cell; however, the Bloch impedances of the two unit cells exhibit complementary characteristics, as can be verified from Figs. 4b and 7b. These complementary characteristics can be attributed to the complementary forms of the Bloch impedances given by Eqs. 2 and 5.

By inspection of both Figs. 4b and 7b, it can also be observed that if the stopband were closed, then a metamaterial line that consists of either T or Π unit cells would not suffer from the rapid Bloch impedance changes around the vicinity of the stopband and would remain close to 50 Ω over a much wider bandwidth extending down to low frequencies. The method by which the stopband can be closed will be outlined in the following section, where it will be demonstrated that indeed when the stopband is closed, the Bloch impedance exhibits a significantly wider bandwidth.

Effective Medium Propagation Characteristics

The dispersion relation of Eq. 1 is sufficient to fully characterize the propagation characteristics of the NRI-TL metamaterial structure. For practical applications,

it is useful to consider the case where the periodically loaded metamaterial line can be considered an effective medium, thus providing further insight into its operation.

In order to consider a series of cascaded unit cells as an effective periodic medium, the physical length of the unit cell must be much smaller than a wavelength, translating into a small electrical length θ, i.e., $\theta \ll 1$. In addition, a small phase shift per unit cell is required in order to avoid the large phase shifts associated with the lower Bragg cutoff frequency, i.e., $\beta_{\mathrm{BL}} d \ll 1$. In order to reflect the effective nature of the periodic metamaterial medium, the Bloch propagation constant β_{BL} will be written as β_{MTM} henceforth. Thus, under the aforementioned assumptions that $\theta \ll 1$ and $\beta_{\mathrm{BL}} d \ll 1$ and considering a periodicity of d for each unit cell, the effective metamaterial propagation constant can be written as

$$\beta_{\mathrm{MTM}} = \pm\omega\sqrt{L_{\mathrm{eff}} C_{\mathrm{eff}}} = \pm\omega\sqrt{\left[L - \frac{1}{\omega^2 C_0 d}\right]\left[C - \frac{1}{\omega^2 L_0 d}\right]}. \tag{7}$$

Equation 7 demonstrates that the effective propagation constant of the metamaterial medium has a similar form to the propagation constant of a conventional transmission line but with effective inductance and capacitance terms, L_{eff} and C_{eff} given by the expressions in the square brackets of Eq. 7. Examining this equation, it can be observed how this medium can exhibit a positive, a negative, and a zero propagation constant, simply by changing the values of the loading parameters L_0 and C_0. When the loading reactance is negligible, the host transmission-line parameters L and C dominate and a forward wave is present on the structure. On the other hand, when the loading reactance is dominant and greater than the individual L and C values, L_{eff} and C_{eff} become negative, and thus the structure supports a backward wave. Finally, when the loading reactances are equal to the host transmission-line parameters L and C, then the effective propagation constant is zero, and there is no propagation along the structure. In this case, a standing wave is established along the structure that has a constant amplitude (i.e., no variation along the z-direction) that varies with time. The lumped-element equivalent circuit of the NRI-TL unit cell under the effective medium conditions $\theta \ll 1$ and $\beta_{\mathrm{BL}} d \ll 1$ is shown in Fig. 8, where L_{eff} can be considered the effective inductance of the series branch, while C_{eff} can be considered the effective capacitance of the shunt branch.

Setting each of the effective material parameters L_{eff} and C_{eff} equal to zero in Eq. 7 results in expressions for the cutoff frequencies of the lower and the upper edges of the stopband, f_{c1} and f_{c2}, respectively, as shown in Fig. 6a:

$$f_{c1} = \min\left\{\frac{1}{2\pi\sqrt{LC_0 d}}, \quad \frac{1}{2\pi\sqrt{L_0 C d}}\right\} = f_{-0}, \tag{8}$$

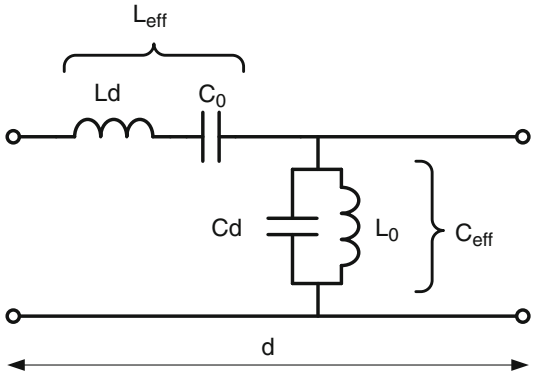

Fig. 8 Lumped-element equivalent circuit of the NRI-TL unit cell under the effective medium conditions $\theta \ll 1$ and $\beta_{\mathrm{BL}} d \ll 1$

$$f_{c2} = \max\left\{ \frac{1}{2\pi\sqrt{LC_0 d}}, \quad \frac{1}{2\pi\sqrt{L_0 Cd}} \right\} = f_{+0}. \tag{9}$$

Note that f_{c1} and f_{c2} also correspond to the zero-degree resonance frequencies f_{-0} and f_{+0}, respectively, discussed in the section "Resonant Characteristics of NRI-TL Metamaterials." Considering the scenario where $1/2\pi\sqrt{LC_0 d} < 1/2\pi\sqrt{L_0 Cd}$, the lower edge of the stopband, f_{c1}, is given by the series resonance between the total series inductance of the transmission line, Ld, and the loading capacitor C_0, while the upper edge of the stopband, f_{c2}, is given by the shunt resonance between the total shunt capacitance of the transmission-line section, Cd, and the loading inductance L_0.

By equating f_{c1} and f_{c2}, the stopband between the two cutoff frequencies can be closed, and a continuous band is formed between the lower left-handed and the upper right-handed bands. The impedance matching condition for closing the stopband in a NRI-TL metamaterial structure can therefore be written as (Eleftheriades et al. 2002)

$$Z_0 = \sqrt{\frac{L_0}{C_0}}. \tag{10}$$

The condition of Eq. 10 can also be written as

$$Z_{0,\mathrm{BW}} = Z_0 \quad \text{or} \quad \sqrt{\frac{L_0}{C_0}} = \sqrt{\frac{L}{C}}. \tag{11}$$

Thus, according to the above impedance matching condition, for a uniform transition between the left-handed band and the right-handed band, the characteristic impedance of the NRI backward-wave line components that load the line must be the same as the characteristic impedance of the PRI host transmission line.

Furthermore, under the effective medium conditions $\theta \ll 1$ and $\beta_{\mathrm{BL}} d \ll 1$, the Bloch impedances for both the T and the Π unit cells reduce to the characteristic impedance of the backward-wave line. Therefore, all three characteristic impedances are equal, resulting in a perfectly matched NRI-TL metamaterial structure:

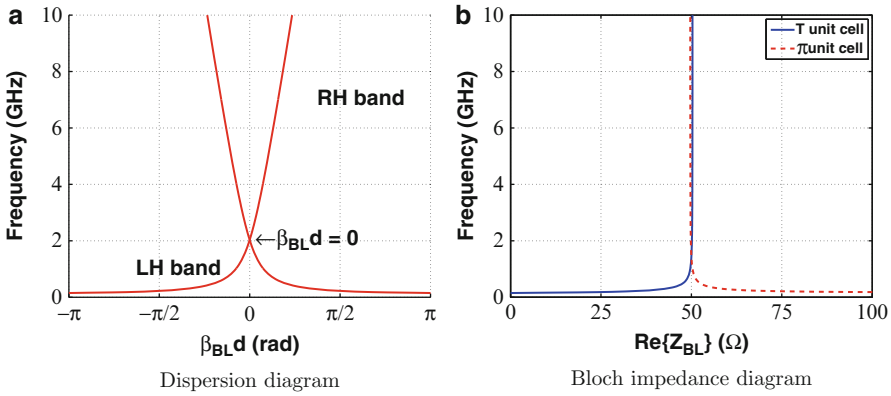

Fig. 9 Characteristics of representative NRI-TL metamaterial T and Π unit cells with parameters $C_0 = 10$ pF, $L_0 = 25$ nH, $Z_0 = 50\ \Omega$, $d = 3$ mm, and $\theta = 8.8°$ at 2 GHz. Note that in this case, the impedance matching condition of $Z_0 = \sqrt{L_0/C_0}$ is imposed, and the stopband is closed

$$Z_{\mathrm{BL}} = Z_{0,\mathrm{BW}} = Z_0. \tag{12}$$

Figure 9a shows a representative dispersion diagram obtained using Eq. 1 for either a T or a Π metamaterial unit cell when the impedance matching condition of Eq. 10 is imposed. It can be observed that compared to the open dispersion diagram of Fig. 6a, there is now a single passband comprising the lower left-handed band that smoothly transitions into the upper right-handed band at the design frequency of $f_0 = 2$ GHz. Thus, depending on the region of operation, Fig. 9a highlights the fact that the NRI-TL metamaterial structure can support forward and backward waves as well as the peculiar case of standing waves with a zero-degree phase shift ($\beta_{\mathrm{BL}} d = 0$) at the closed stopband point of $f_0 = 2$ GHz. Additionally, around the design frequency, the phase response is linear and broadband with frequency.

Figure 9b shows the Bloch impedance diagrams for both the T and π unit cells under the impedance matching condition of Eq. 10, which exhibit as expected complementary characteristics. From Fig. 9b, it can be observed that the Bloch impedance remains remarkably constant around 50 Ω for a much wider bandwidth compared to the open stopband cases of Figs. 4b and 7b, which suffer from rapid changes in the Bloch impedance around the vicinity of the stopbands.

The impedance matching condition of Eq. 10 can subsequently be used in Eq. 7 to derive an approximate expression for the effective propagation constant of the line, given as

$$\beta_{\mathrm{MTM}} = \omega\sqrt{LC} + \frac{-1}{\omega\sqrt{L_0 C_0} d} \tag{13}$$

$$\beta_{\mathrm{MTM}} = \beta_{\mathrm{H-TL}} + \beta_{\mathrm{BW}}. \tag{14}$$

This expression can be interpreted as the sum of the propagation constants of the host transmission line, $\beta_{\text{H-TL}}$, and a uniform backward-wave line, β_{BW}, formed by the loading elements L_0 and C_0. The analogous effective phase shift per unit cell can be written as

$$\phi_{\text{MTM}} = -\beta_{\text{MTM}} d. \tag{15}$$

Inserting Eq. 13 into Eq. 15, the effective phase shift per NRI-TL metamaterial unit cell under the impedance matching condition of Eq. 10 can be written as (Antoniades and Eleftheriades 2003)

$$\phi_{\text{MTM}} = -\omega\sqrt{LC}d + \frac{1}{\omega\sqrt{L_0 C_0}} \tag{16}$$

$$\phi_{\text{MTM}} = \phi_{\text{H-TL}} + \phi_{\text{BW}}. \tag{17}$$

Equation 16 can be recognized as the sum of the phases incurred by the host transmission line, $\phi_{\text{H-TL}}$, and the backward-wave line, ϕ_{BW}, which was described initially in Fig. 2. This equation succinctly describes the inherent phase-compensating nature of each NRI-TL metamaterial unit cell. By adjusting the values of the loading elements L_0 and C_0 while maintaining the impedance matching condition, the effective phase shift across each unit cell can be tailored to produce a net positive, negative, or even a 0° phase shift at a given frequency. It should be emphasized that the necessary conditions for the phase relationship presented in Eq. 16 to be valid are that the impedance matching condition of Eq. 10 must be satisfied, the physical length of the unit cell must be small compared to the wavelength, i.e., $|\phi_{\text{H-TL}}| \ll 1$, and the phase shift per unit cell must also be small, i.e., $|\phi_{\text{MTM}}| \ll 1$.

Multistage NRI-TL Metamaterial Phase-Shifting Lines

The propagation characteristics of a single metamaterial unit cell presented in the sections "Propagation and Impedance Characteristics of the T Unit Cell" and "Propagation Characteristics of the Π Unit Cell" can be used to design multistage metamaterial lines, provided that the metamaterial line is terminated in its Bloch impedance. In this manner, each unit cell within the finite metamaterial line will effectively see an infinite periodic medium and will thus retain its propagation characteristics. Consequently, the phase expressions derived assuming an infinite periodic medium can be used in order to characterize the phase response of a finite metamaterial structure.

If the source and load terminations are equal to the characteristic impedance of the metamaterial line in the matched case (Eq. 12), then from Eq. 16, the total phase incurred by an N-stage metamaterial line as shown in Fig. 2 can be written as the sum of the phase incurred by each constituent unit cell:

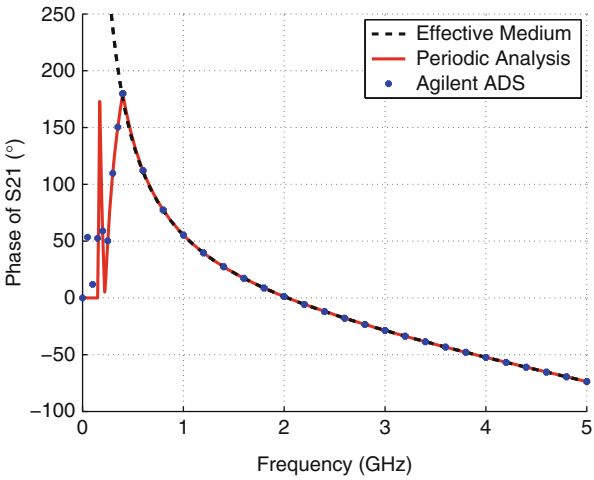

Fig. 10 Phase responses of a four-stage NRI-TL metamaterial line obtained using the effective medium phase shift of Eq. 18, periodic analysis, and the simulator Agilent-ADS. Parameters used: $Z_{\text{term}} = 50\ \Omega$, $C_0 = 10$ pF, $L_0 = 25$ nH, $Z_0 = 50\ \Omega$, $d = 3$ mm, and $\theta = 8.8°$ at 2 GHz

$$\Phi_{\text{MTM}} = N\phi_{\text{MTM}} = N\left(-\omega\sqrt{LC}d + \frac{1}{\omega\sqrt{L_0C_0}}\right). \tag{18}$$

In order to verify the validity of the above arguments, the phase response of a representative four-stage metamaterial line was obtained using the effective medium phase shift of Eq. 18, periodic analysis of a cascade of four identical T unit cells, and the Agilent-ADS circuit simulator, and the results are shown in Fig. 10.

It can be observed that the phase responses obtained from the effective medium analysis, from the periodic analysis, and from Agilent-ADS are identical within the passband of the structure. As expected, the effective medium response of Eq. 18 does not exhibit a low-frequency cutoff. At low frequencies below 0.15 GHz, the structure has a stopband, and therefore the periodic analysis is not able to predict the phase. Nevertheless, these results confirm that the propagation characteristics derived for the infinitely periodic case can also be used to design finite-length metamaterial phase-shifting lines, provided that the lines are terminated in their Bloch impedance.

Antenna Design Using TL Metamaterials

Resonant Characteristics of NRI-TL Metamaterials

Multiband Operation

The rich dispersion characteristics of metamaterials form the underlying basis for their use in many antenna applications. In this section, the resonant characteristics of NRI-TL metamaterial structures are analyzed by considering their dispersion diagrams. These can be used to visualize how these structures can be designed to offer multiband responses whose resonant frequencies are not harmonically related while offering large degrees of miniaturization.

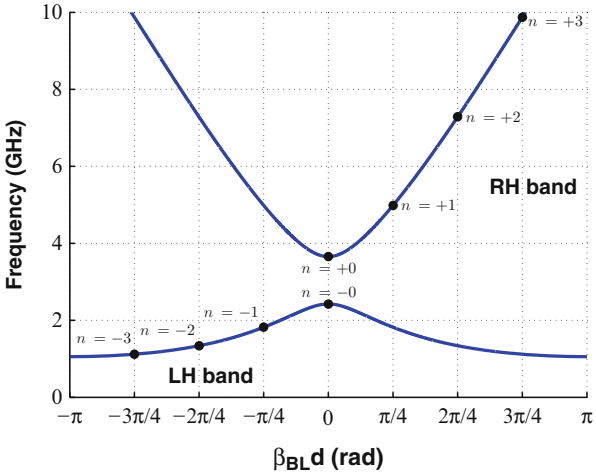

Fig. 11 Typical dispersion diagram for a NRI-TL metamaterial unit cell with parameters $C_0 = 0.14$ pF, $L_0 = 30$ nH, $Z_0 = 300\ \Omega$, $d = 12.5$ mm, and $\theta = 45°$ at 3 GHz. Superimposed are the locations of the nth order resonances for a metamaterial structure that consists of a cascade of $N = 4$ unit cells. Note the contraction of the resonant frequencies in the left-handed (LH) band compared to the right-handed (RH) band and the fact that the resonant frequencies are not harmonically related

Figure 11 shows a representative dispersion diagram obtained using Eq. 1, where the propagation characteristics of the metamaterial can be observed. When investigating the resonant properties of this structure, of particular interest are the frequencies where the total electrical length is equal to zero and integer multiples of π (Eleftheriades 2009), i.e.,

$$\beta_{\mathrm{BL}}\ell_{\mathrm{TOT}} = n\pi \quad ; \quad n = \pm 0, \quad \pm 1, \quad \pm 2 \ldots \tag{19}$$

Thus, for resonant antenna applications, effective radiation can be achieved from the metamaterial structure when its total length ℓ_{TOT} is equal to integer multiples of half a wavelength (Schussler et al. 2004a; Caloz and Itoh 2006):

$$\ell_{\mathrm{TOT}} = n\frac{\lambda}{2} \quad ; \quad n = \pm 0, \quad \pm 1, \quad \pm 2 \ldots \tag{20}$$

In the general case where N unit cells are used in order to implement the metamaterial structure with a total length of $\ell_{\mathrm{TOT}} = Nd$, then the analogous electrical length per unit cell becomes

$$\beta_{\mathrm{BL}}d = \frac{n\pi}{N} \quad ; \quad n = \pm 0, \quad \pm 1, \quad \pm 2 \ldots \pm (N-1) \tag{21}$$

An N-stage metamaterial structure can therefore support negative-order ($n < 0$) resonances in the left-handed band, zeroth-order ($n = 0$) resonances at the

$\beta_{BL}d = 0$ point, and positive-order ($n > 0$) resonances in the right-handed band. This is in contrast to conventional right-handed structures that can support only positive-order resonances within the right-handed region of their respective dispersion diagram.

The resonances that are achievable with a metamaterial structure are depicted graphically on the dispersion diagram of Fig. 11 for the representative case of $N = 4$ unit cells. Thus, within the irreducible Brillouin zone of $-\pi < \beta_{BL}d < \pi$ on the dispersion diagram, there are potentially $2N$ resonances that can be excited. For every nth resonance that occurs at each of the $\beta_{BL}d = \frac{n\pi}{N}$ points along the horizontal axis, there is an analogous resonance frequency, f_n, along the vertical axis. In general, the total number of resonances that are excited within a metamaterial structure will be less than $2N$ and will depend on the excitation mechanism and the terminal impedances. Since each nth resonance corresponds to a particular mode, i.e., a particular field distribution on the structure, the excitation mechanism will determine which modes are coupled to and therefore which modes appear in the resulting frequency response. In practical antenna applications, it is not in general possible to couple to all of the modes simultaneously using a single feed; therefore, the number of resonances that will typically appear will be less than $2N$. This can be observed in many of the examples subsequently shown in the section "Antenna Applications of TL-Metamaterials."

In order to keep the antenna size small, typically only the $n = \pm 0$ and $n = \pm 1$ resonances are employed in the design of metamaterial antennas, i.e., when $\beta_{BL}\ell_{TOT} = \pm 0$ and $\beta_{BL}\ell_{TOT} = \pm\pi$. At these frequencies, resonant standing waves are excited on the structure. Two conventional applications which employ a $+\pi$ resonance are a $\lambda/2$ dipole antenna whose current distribution has a phase shift of π along the length of the dipole and a $\lambda/2$ patch antenna which also establishes a π phase shift between its two radiating edges. As has been outlined above, structures that employ NRI-TL metamaterial loading also have the ability to excite the $+\pi$ resonance but have the additional benefit and flexibility of exciting the $\pm$zero and the $-\pi$ resonances at nonharmonic frequencies.

Compact Designs with a Small Number of Unit Cells, *N*

The $n = \pm 0$ zeroth-order resonances (ZOR) are independent of the total number of unit cells N in the structure (Antoniades and Eleftheriades 2003), since each constituent unit cell incurs in and of itself 0°. This can be seen by setting $n = 0$ in Eq. 21. Thus, any number of unit cells can be chosen in order to implement the $n = \pm 0$ resonances, including the limiting case of $N = 1$. The zeroth-order resonances are therefore well suited for antenna miniaturization purposes, as will be outlined in the subsequent section. For the general case of a dispersion relation with an open stopband, as shown in Fig. 11, the zero-degree resonance will occur at two resonant frequencies, f_{-0} and f_{+0}. Note that these two frequencies are the same as the cutoff frequencies f_{c1} and f_{c2} in Fig. 6a. Note also that in terms of nomenclature, the $n = \pm 0$ zeroth-order resonance (ZOR) frequencies are also known as zero-degree frequencies, zero-index frequencies, infinite-wavelength frequencies, epsilon-zero (EZR) frequencies, and mu-zero (MZR) frequencies.

The $\pm\pi$ resonances will depend on the total number of unit cells comprising the metamaterial structure. Thus, for a structure consisting of N unit cells, the $\pm\pi$ resonances will be excited when the electrical length per unit cell is equal to $\beta_{\mathrm{BL}}d = \pm\ \pi/\mathrm{N}$, from Eq. 21. It should be noted that the number of unit cells used to implement the metamaterial structure is in theory arbitrary; however, in practice it is limited by the space that is available to implement the host transmission line and the loading elements L_0 and C_0 for each metamaterial unit cell.

As will be shown in the section "Design Equations for Rapid Prototyping," a larger number of unit cells results in larger loading-element values L_0 and C_0 required in order to implement the desired phase shift per unit cell. From Eqs. 24 and 25, if N unit cells are used in order to implement the structure, then the values of the required loading elements will be N times larger than the implementation with a single unit cell. Thus, N should be kept small in order to facilitate the physical realization of the loading elements L_0 and C_0, especially if these are implemented in fully printed form. Additionally, if the loading elements L_0 and C_0 are implemented using off-the-shelf surface-mount chip components, then it is advantageous to keep their values low since these generally come in smaller packages and have higher self-resonant frequencies (see for example the Coilcraft Inc. chip inductor datasheet (Coilcraft Inc 2015)). Finally, a single unit cell realization of the $\pm\pi$ resonances should be avoided, since this corresponds to operation at the onset of the lower and upper stopband regions, which are associated with high insertion losses.

Antenna Miniaturization

Negative-Order Resonant Modes, $n < 0$

For the purpose of antenna miniaturization, the resonant frequencies that lie within the lower left-handed band on the dispersion diagram of Fig. 11 are of most interest. This is because these negative-order resonant modes with $n < 0$ are associated with large propagation constants at low frequencies and a contraction of the guided wavelength as the frequency decreases (Schussler et al. 2004a; Lee et al. 2006; Iizuka and Hall 2007; Eleftheriades 2009).

Within the lower left-handed band, the backward-wave propagation constant $\beta_{\mathrm{BW}} = -1/\omega\sqrt{L_0C_0}d$ is dominant (see Eq. 13), which is inversely proportional to the frequency. Therefore, the propagation constant increases as the frequency decreases, allowing large propagation constants to be achieved at low frequencies, facilitating the realization of the $-\pi$ resonance. Furthermore, the propagation constant is also inversely proportional to the loading-element values L_0 and C_0, therefore enabling large propagation constants to be achieved with small loading-element values. This enables the design of compact resonant antennas with loading elements that can be easily realized in printed form, while maintaining the overall antenna size much smaller than $\lambda/2$.

The above scenario is in contrast to conventional right-handed lines, where the propagation constant is directly proportional to the frequency, therefore necessitating antenna sizes that are on the order of $\lambda/2$ in order to create resonant antennas.

The size of resonant right-handed antennas can be reduced by employing slow-wave low-pass loading; however, since the propagation constant is proportional to the loading-element values, the required loading-element values are significantly larger than the ones required for the metamaterial-loaded antennas with the same size reduction.

With reference to Fig. 11, note that in the left-handed band, the resonant frequencies are spaced much closer together compared to the resonances in the right-handed band, and they are *not* harmonically related. This can again be attributed to the fact that the dominant backward-wave propagation constant in this band is inversely proportional to the frequency. In the right-handed band, the propagation constant of the host transmission line $\beta_{\mathrm{H-TL}} = \omega\sqrt{LC}$ is dominant; therefore, the propagation constant is directly proportional to the frequency, and the resonant frequencies *are* harmonically related. Thus, the metamaterial structure exhibits a contraction of the resonant frequencies in the left-handed (LH) band compared to the right-handed (RH) band. Furthermore, the locations of the resonant frequencies can be directly controlled by adjusting the loading-element values L_0 and C_0, through a process called "dispersion engineering."

Zeroth-Order Resonant (ZOR) Modes, $n = \pm 0$

Antenna miniaturization can also be achieved at the two points on the dispersion diagram where the propagation constant is zero, i.e., for the $n = \pm 0$ ZOR frequencies of f_{-0} and f_{+0}. In the closed stopband case shown in Fig. 9, these two frequencies merge into one ZOR frequency, $f_{\pm 0}$. Note that the two ZOR frequencies are not harmonically related and can be easily adjusted by changing the metamaterial structure's transmission line and loading parameters (see Eqs. 8 and 9). This provides great flexibility when designing ZOR antennas, since it allows the ZOR frequencies to be placed arbitrarily.

At the two ZOR frequencies, the phase shift that each metamaterial unit cell incurs is 0° and is independent of the unit cell's physical length. Therefore, any number of unit cells, N, can be cascaded together, and the resulting overall phase shift that the metamaterial structure incurs will still be 0°. Thus, in theory the zero-degree metamaterial structures can be made infinitesimally small, enabling large degrees of antenna miniaturization. In practice, the size of the zero-degree unit cells is limited by the available space required to implement the host transmission line and the loading elements L_0 and C_0, especially if these are realized in printed form. In order to achieve the equivalent -2π phase shift from a conventional transmission line, its length must be one guided wavelength, λ_g. Consequently, the physical size of the zero-degree metamaterial structures can be made significantly smaller than that of a λ_g transmission line and in the limiting case can be simply a single zero-degree metamaterial unit cell.

Note that for antenna applications, a single unit cell realization of the zero-degree resonances is not problematic, as was the case for the $\pm\,\pi$ resonances described in the section "Compact Designs with a Small Number of Unit Cells, N." This is because for the case of a closed stopband, the $\beta_{\mathrm{BL}}d = \pm 0$ point is not at the edge of a

stopband region, and in the open stopband case, even though the two $\beta_{\mathrm{BL}}d = \pm 0$ points are at the edge of the central stopband, the impedance seen at the terminals of the antenna primarily consists of the radiation resistance of the structure. For the latter case, if the radiation resistance of a single unit cell is not high enough, this could necessitate the use of additional unit cells in order to increase the overall antenna radiation resistance.

Design Equations for Rapid Prototyping

When designing compact antennas, a designer will typically try to achieve a targeted performance within a specified antenna volume or the targeted performance could be sought while attempting to minimize the antenna volume. Alternatively, the maximum antenna performance could be sought for a specified volume. Performance metrics could include input impedance bandwidth, multiband operation, polarization, directive properties, and radiation efficiency.

For the design of compact antennas based on transmission-line metamaterials, once the mode of operation is chosen based on the analysis of the section "Resonant Characteristics of NRI-TL Metamaterials," e.g., $n = 0$ or $n = -1$, the primary concern is to obtain the loading-element values L_0 and C_0 required to realize the metamaterial. Thus, for a given antenna volume, the designer must choose the number of metamaterial unit cells N that will be used in the realization of the antenna, as well as the technology that the transmission lines will be implemented in (e.g., microstrip, coplanar waveguide, etc.). Typically, based on the volume constraints and the system impedance, the designer will also choose the parameters of the host transmission line, namely, the characteristic impedance Z_0 and the propagation constant $\beta_{\text{H-TL}}$, and the length of each unit cell d. This will in turn define the electrical length of each transmission-line section $\theta = \beta_{\text{H-TL}}d$ and the corresponding phase that each transmission-line section incurs $\phi_{\text{H-TL}} = -\theta = -\beta_{\text{H-TL}}d$. These parameters will subsequently allow the designer to calculate the loading-element values required to achieve a specific phase shift for each metamaterial unit cell. Below are outlined two methods for obtaining these loading-element values: the first method provides simple and intuitive approximate design equations derived from the effective medium case of the section "Effective Medium Propagation Characteristics," and the second method provides exact design equations derived for the periodic medium case of the sections "Propagation and Impedance Characteristics of the T Unit Cell" and "Propagation Characteristics of the Π Unit Cell."

Approximate Expressions for NRI-TL Metamaterials

For the effective medium outlined in the section "Effective Medium Propagation Characteristics," closed-form expressions can be derived for the values of the loading elements L_0 and C_0 required to produce a desired phase shift per unit cell ϕ_{MTM} at a given frequency ω_0, given a section of host transmission line with parameters Z_0 and $\phi_{\text{H-TL}}$. Approximate expressions for the loading elements can

be obtained by substituting the impedance matching condition of Eq. 10 into Eq. 16 and solving for L_0 and C_0

$$L_0 = \frac{Z_0}{\omega_0(\phi_{\mathrm{MTM}} - \phi_{\mathrm{H-TL}})}, \tag{22}$$

$$C_0 = \frac{1}{\omega_0 Z_0(\phi_{\mathrm{MTM}} - \phi_{\mathrm{H-TL}})}. \tag{23}$$

It should be noted that since the impedance matching condition of Eq. 10 was used in the derivation of Eqs. 22 and 23, these are only valid when the stopband is closed and in the effective medium limit of $|\phi_{\mathrm{MTM}}| \ll 1$ and $|\phi_{\mathrm{H-TL}}| \ll 1$. Nonetheless, these expressions are very simple and intuitive and clearly highlight the factors that affect the values of the loading elements.

The loading-element values can also be expressed in terms of the total phase shift that the metamaterial structure incurs. If the metamaterial structure consists of N unit cells, and the total phase shift that it incurs is $\Phi_{\mathrm{MTM}} = N\phi_{\mathrm{MTM}}$ given by Eq. 18, while the total phase shift that the host transmission line incurs is $\Phi_{\mathrm{H\text{-}TL}} = N\phi_{\mathrm{H\text{-}TL}}$, then from Eqs. 22 and 23 the loading-element values can be written as

$$L_0 = N\left(\frac{Z_0}{\omega_0(\Phi_{\mathrm{MTM}} - \Phi_{\mathrm{H-TL}})}\right), \tag{24}$$

$$C_0 = N\left(\frac{1}{\omega_0 Z_0(\Phi_{\mathrm{MTM}} - \Phi_{\mathrm{H-TL}})}\right). \tag{25}$$

These expressions reveal that from a design point of view, it is advantageous to keep N small, i.e., use a small number of unit cells, resulting in smaller values for the required loading-element values.

Exact Expressions for NRI-TL Metamaterials

For the periodic medium of the sections "Propagation and Impedance Characteristics of the T Unit Cell" and "Propagation Characteristics of the Π Unit Cell," the exact expressions for the loading elements can be obtained by employing the full dispersion relation of Eq. 1 for the general case where the stopband can be either open or closed. In both cases, it is desired to calculate the loading elements for a given phase shift per unit cell, $\phi_{\mathrm{MTM}} = -\beta_{\mathrm{BL}}d$, and Bloch impedance, Z_{BL}.

Closed Stopband

Considering first the case when the stopband is closed, recall from Fig. 9 that the Bloch impedance remains very close to the value of Z_0 over a large frequency range. Thus, a very good approximation for the Bloch impedance for a large range of frequencies is actually the value of Z_0. Therefore, the impedance matching condition of Eq. 10 is rearranged to obtain an expression of the loading inductance L_0 in terms of C_0 and Z_0:

$$L_0 = C_0 Z_0^2. \tag{26}$$

By substituting Eq. 26 into Eq. 1, a quadratic equation in terms of C_0 is obtained:

$$(\cos(\beta_{\mathrm{BL}} d) - \cos(\theta)) C_0^2 - \left(\frac{\sin(\theta)}{\omega_0 Z_0}\right) C_0 + \frac{1 + \cos(\theta)}{4\omega_0^2 Z_0^2} = 0. \tag{27}$$

The solution to the above quadratic equation can be written as

$$C_0 = \frac{\left(\frac{\sin(\theta)}{\omega_0 Z_0}\right) \pm \sqrt{\left(\frac{\sin(\theta)}{\omega_0 Z_0}\right)^2 - 4(\cos(\beta_{\mathrm{BL}} d) - \cos(\theta))\left(\frac{1 + \cos(\theta)}{4\omega_0^2 Z_0^2}\right)}}{2(\cos(\beta_{\mathrm{BL}} d) - \cos(\theta))}. \tag{28}$$

The positive solution of the quadratic equation is sought, therefore resulting in unique values for L_0 and Co from Eqs. 26 and 28. A particular case of Eq. 27 arises when $\beta_{\mathrm{BL}} d$ is equal to θ (or equivalently $|\phi_{\mathrm{MTM}}| = |\phi_{\mathrm{H\text{-}TL}}|$). In this case, the first term of Eq. 27 is equal to zero, and the loading capacitance C_0 can be simply expressed as

$$C_0 = \frac{1 + \cos(\theta)}{4\omega_0 Z_0 \sin(\theta)}. \tag{29}$$

Open Stopband

The open stopband case is the most general case and proceeds in a similar, yet slightly more complicated manner. The two design parameters in this case are the phase shift per unit cell, given by the dispersion relation of Eq. 1, and the Bloch impedance given by Eq. 2 or 5. Both the dispersion and Bloch impedance relations are functions of L_0 and C_0; however, an attempt to find a closed-form expression for these reveals that the expression quickly becomes very complicated. A simple way to overcome this problem is to solve for L_0 and C_0 graphically by expressing C_0 in terms of L_0 through the general form of the dispersion relation of Eq. 1, given in terms of Z and Y. Therefore, Eq. 1 can be written as

$$Z = \frac{\cos(\beta_{\mathrm{BL}} d) - \cos(\theta) - j\frac{YZ_0}{2}\sin(\theta)}{\frac{Y}{4}\cos(\theta) + j\frac{Y_0}{2}\sin(\theta) + \frac{Y}{4}} = \frac{1}{j\omega C_0}. \tag{30}$$

Recall from Eq. 3 that $Z = 1/j\omega C_0$ and $Y = 1/j\omega L_0$. Substituting Eq. 30 into the Bloch impedance expressions of Eq. 2 or 5 and by sweeping the value of L_0, a range of values for the Bloch impedance is obtained. The final value of L_0 is obtained by selecting the value that corresponds to the desired Bloch impedance. The loading capacitance C_0 is subsequently found by substituting the value of L_0 into $\mathrm{Y} = 1/\mathrm{j}\omega\mathrm{L}_0$ and then into Eq. 30.

In summary, NRI-TL metamaterial structures have the ability to support negative-order resonances, positive-order resonances, and zeroth-order resonances, meaning that they can incur a positive, negative, or zero phase shift depending on the values of the loading elements while maintaining a small physical size. In addition, only a few unit cells are required in order to achieve the resonant characteristics necessary to implement compact resonant antennas. Furthermore, antenna miniaturization can be achieved for structures that support negative-order resonances and/or zeroth-order resonances. With these in mind, the following section focuses on various antenna applications that have exploited the beneficial properties of metamaterials to create multiband, compact, and efficient antennas.

Antenna Applications of TL Metamaterials

Zeroth-Order Resonant Antennas, $n = \pm 0$

A Zero-Index NRI-TL Metamaterial Folded-Monopole Antenna

The first antenna described herein that employs the $n = 0$ zeroth-order resonance of NRI-TL metamaterials is an electrically small folded-monopole antenna, as shown in Fig. 12 (Antoniades and Eleftheriades 2008b). This is also referred to as a zero-index

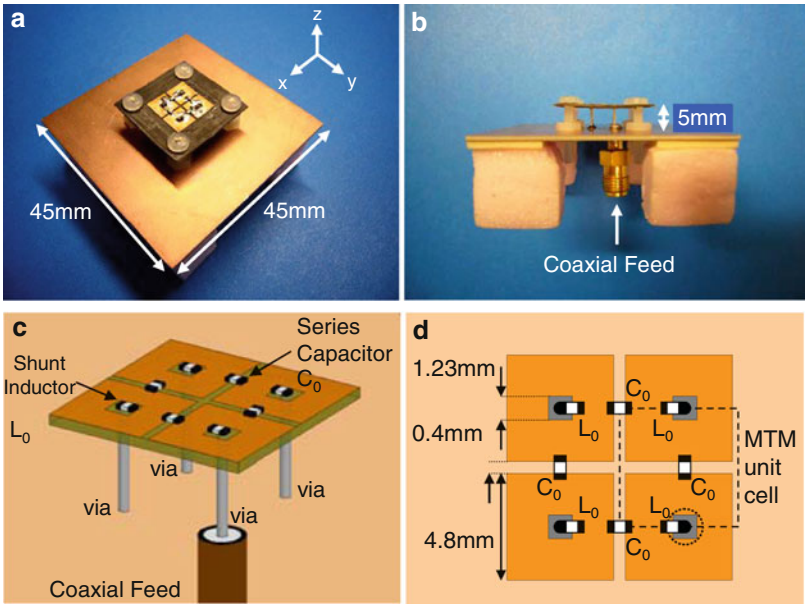

Fig. 12 Electrically small zero-index metamaterial folded-monopole antenna: (**a**) perspective view, (**b**) side view, (**c**) three-dimensional diagram, and (**d**) top view diagram. Ideal metamaterial parameters used: $N = 4$, $f_0 = 3$ GHz, $\phi_{\mathrm{MTM}} = 0°$, $\phi_{\mathrm{H\text{-}TL}} = -17.69°$, $Z_0 = 126.15\ \Omega$, $C_0 = 1.36$ pF, $L_0 = 21.67$ nH (Antoniades and Eleftheriades 2008b) © 2008 IEEE

metamaterial antenna, since at the $\beta_{\mathrm{BL}}d = 0$ point, the refractive index is equal to zero. This antenna was first presented in Eleftheriades et al. (2004) and subsequently in Eleftheriades et al. (2007) using fully printed loading elements, and variations using surface-mount lumped-element components were presented in Qureshi et al. (2005) and Eleftheriades (2007).

The metamaterial antenna consists of $N = 4$ microstrip NRI-TL metamaterial unit cells that are arranged in a 2×2 configuration over a ground plane. Each metamaterial unit cell was designed to excite the $n = 0$ zeroth-order resonant mode under a closed stopband condition at a design frequency of $f_0 = 3$ GHz. The antenna was designed based on the symmetric NRI-TL metamaterial Π unit cell shown in Fig. 3b. The Π topology was chosen because it reveals the natural monopole folding effect that the circuit provides, which is achieved by feeding the antenna from the base of one of the inductors.

In order to feed each of the vertical vias of the antenna in phase, it is required that each metamaterial unit cell incurs 0° at the design frequency, f_0. Therefore, for a chosen unit cell size, Eqs. 22 and 23 were used to design metamaterial unit cells that incurred a phase shift of $\phi_{\mathrm{MTM}} = 0°$ at 3 GHz, under the closed stopband condition of Eq. 10.

Even-Odd Mode Analysis

The proposed zero-index metamaterial antenna of Fig. 12 can be analyzed by decomposing the antenna current into a superposition of an even mode (I_e) and an odd mode (I_o). Since the antenna is symmetrical, analysis of a single unit cell that contains two vias will reveal the general characteristics of the entire antenna, namely, that the even-mode current is dominant on the structure. Even though the analysis of a single unit cell only models two folded arms (vias), nevertheless this provides a qualitative measure of the antenna performance. Furthermore, Goubau has analyzed the case of an N-element folded monopole where only one of the monopoles is excited and has demonstrated that the results can be generalized from the two-element case (Goubau 1976; Vaughan and Bach-Andersen 2003, pp. 515–518).

Beginning with the even-mode excitation, two equal voltages (V/2) are applied to each end of the metamaterial unit cell of Fig. 3b as shown in Fig. 13a. Due to the symmetry of the unit cell, this effectively places an open circuit (OC) at the center of the structure, thus producing two identical decoupled circuits. Note that in the circuit of Fig. 13a, the vertical vias connecting the inductors to ground have been explicitly included in order to highlight their importance as the main radiating elements in the structure.

Each via can then be replaced with its corresponding radiation resistance R_r and its associated inductance L_{via} can be added to the lumped inductor value L_0', resulting in a total inductance of L_0. By replacing the short transmission-line sections with their equivalent series inductance $L' = Ld$ and capacitance $C' = Cd$, the circuit of Fig. 13b is obtained. No current will pass through the series resonator formed by $L'/2$ and $2C_0$ because it is open circuited on one end; therefore, these components can be removed from the circuit. At resonance (when $\phi_{\mathrm{MTM}} = 0°$), the series resonator formed by $2L_0$ and $C'/2$ will become a short circuit, therefore resulting in the final

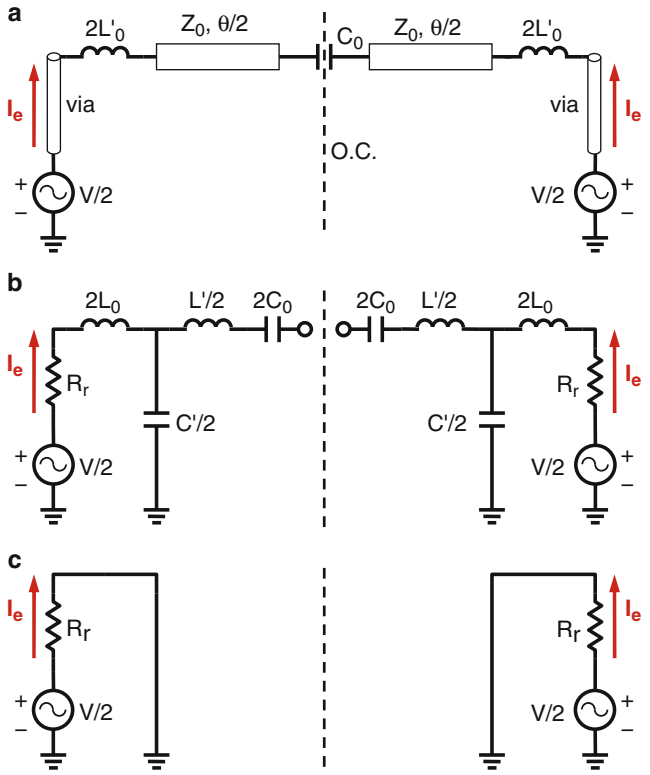

Fig. 13 Even-mode equivalent circuits for a single unit cell of the zero-index metamaterial antenna: (**a**) TL-based metamaterial unit cell, (**b**) lumped-element equivalent circuit, and (**c**) simplified lumped-element circuit at resonance (Antoniades and Eleftheriades 2008b) © 2008 IEEE

simplified circuit of Fig. 13c. Since no other impedances are present in the circuit other than R_r, maximum current will be delivered to the radiation resistance, given by $I_e = (V/2)/R_r$.

Considering now the odd-mode excitation, an equal and opposite voltage is applied to each end of the metamaterial unit cell as shown in Fig. 14a. Due to the symmetry of the unit cell, this effectively places a short circuit (SC) at the center of the structure, thus producing two identical decoupled circuits with equal and opposite excitations. If the vias are then replaced with their corresponding radiation resistance R_r and inductance L_{via} and the short transmission-line sections with their equivalent series inductance $L' = Ld$ and capacitance $C' = Cd$, the circuit of Fig. 14b is obtained. At resonance, the series resonator formed by $L'/2$ and $2C_0$ will become a short circuit, thus shorting out $C'/2$ and therefore resulting in the final simplified circuit of Fig. 14c. It can now be observed that the odd-mode current will be given by $I_o = (V/2)/(R_r + j\omega 2L_0)$. Therefore, the $2L_0$ inductor plays a pivotal role

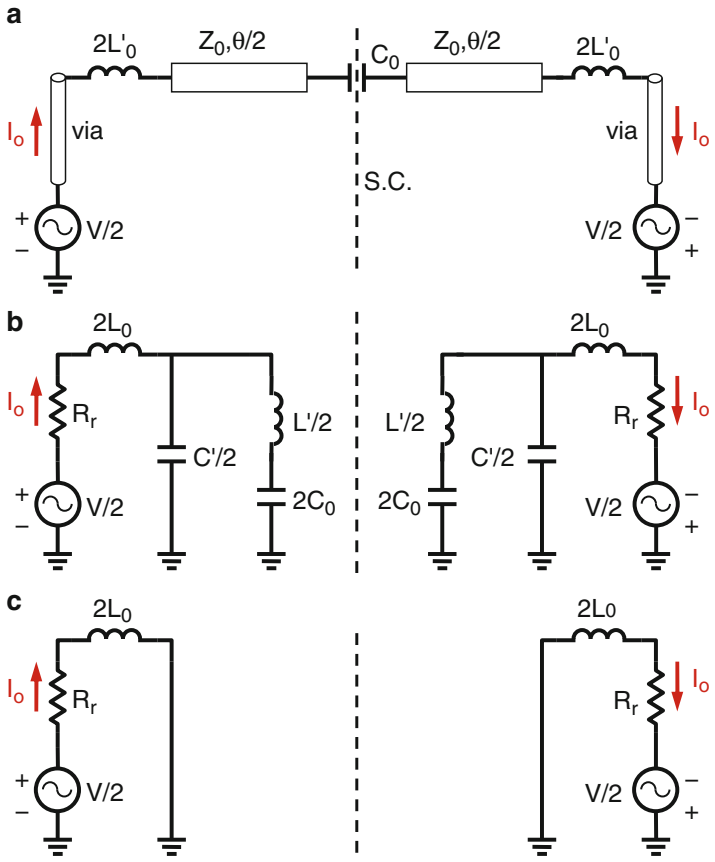

Fig. 14 Odd-mode equivalent circuits for a single unit cell of the zero-index metamaterial antenna: (**a**) TL-based metamaterial unit cell, (**b**) lumped-element equivalent circuit, and (**c**) simplified lumped-element circuit at resonance (Antoniades and Eleftheriades 2008b) © 2008 IEEE

in adjusting the odd-mode current, and for any value of the loading inductor $2L_0$, I_e will always be greater than I_o.

Considering some representative values, a short monopole with a uniform current distribution will have a radiation resistance of (Schelkunoff and Friis 1952)

$$R_r = 160\pi^2(h/\lambda)^2. \tag{31}$$

A close approximation to a uniform current distribution can be achieved by top loading the monopole with a metal plate, something that is inherently achieved in the microstrip design shown in Fig. 12. Therefore, for a monopole with $h/\lambda = 1/20$, the radiation resistance from Eq. 31 will be $R_r = 4\ \Omega$. Assuming that the excitation voltage is V = 1 volt, for a typical value of $L_0 = 20$ nH, at 3 GHz the magnitude of the odd-mode current is $|I_o| = 0.66$ mA. The corresponding even-mode current is

$|I_e| = 127$ mA, which is approximately 190 times greater than $|I_o|$. Therefore, since the majority of the current flowing on the vertical vias lies in the even mode, this enables the metamaterial structure to act as a good radiator.

From the above discussion, it can be seen that a short monopole has a radiation resistance in the range of a few ohms, which makes it hard to match to 50 Ω. A simple way to increase the input impedance of a resonant antenna is to use a multiple folding technique (Best 2005), which relies on the fact that the currents in each arm of the antenna are in phase. As has been demonstrated with the even-odd mode analysis, this is naturally achieved with the NRI-TL metamaterial unit cell. For an antenna with N folded arms, the input impedance is given by (Best 2005)

$$R_{\text{in}} \approx N^2 R_r. \tag{32}$$

Thus, an antenna with $N = 4$ folded arms that are each $\lambda/20$ long and have $R_r = 4\ \Omega$ would have an input impedance of $R_{\text{in}} = 64\ \Omega$. This is sufficiently close to 50 Ω to provide a good match; therefore, the height of the antenna was chosen to be $h = \lambda/20 = 5$ mm.

Having established through the even-odd mode analysis that at the design frequency the zero-index metamaterial antenna maximizes the even-mode current, this enables it to be modeled as a folded monopole, thus exhibiting a substantial increase in the radiation resistance from Eq. 32. Consequently, all four vias of the antenna are excited with equal currents in terms of their magnitude and phase. Figure 15a, b shows the geometry and the simulated current distribution of the metamaterial antenna obtained using a full-wave simulator, where it can be observed that indeed all four vias are excited with equal currents. The four-unit-cell design was further extended to a design with eight unit cells as shown Fig. 15c, d, where it can again be observed that all eight vias are excited equally.

Figure 15e, f compares the input impedance of the two antennas, which verifies that indeed the radiation resistance increases according to N^2. For the four-via antenna of Fig. 15a, the full-wave simulated input resistance at resonance is $R_{\text{in}} = 70.6\ \Omega$, which is very close to the theoretical value of 64 Ω that was calculated above using Eq. 32. For the eight-via antenna of Fig. 15c, the full-wave simulated input resistance at resonance is as expected approximately four times that of the four-via antenna, i.e., $R_{\text{in}} \approx 8^2(70.6/4^2) = 282\ \Omega$. It can be noted that this result is different than the one presented in Best (2014), where the driven via is out of phase with the remaining vias. Here, all the vias are excited in phase and the folding effect of Eq. 32 is fully realized.

The final antenna of Fig. 12 has dimensions of $\lambda_0/10 \times \lambda_0/10 \times \lambda_0/20$ over a $0.45\lambda_0 \times 0.45\lambda_0$ ground plane, and it exhibits a 53 MHz −10 dB measured $|S_{11}|$ bandwidth around 3.1 GHz, as shown in Fig. 16a, and a relatively high radiation efficiency of 70 %. The radiation patterns shown in Fig. 16b, c verify that this antenna radiates a vertically polarized linear electric field vector, consistent with a vertically oriented folded-monopole geometry.

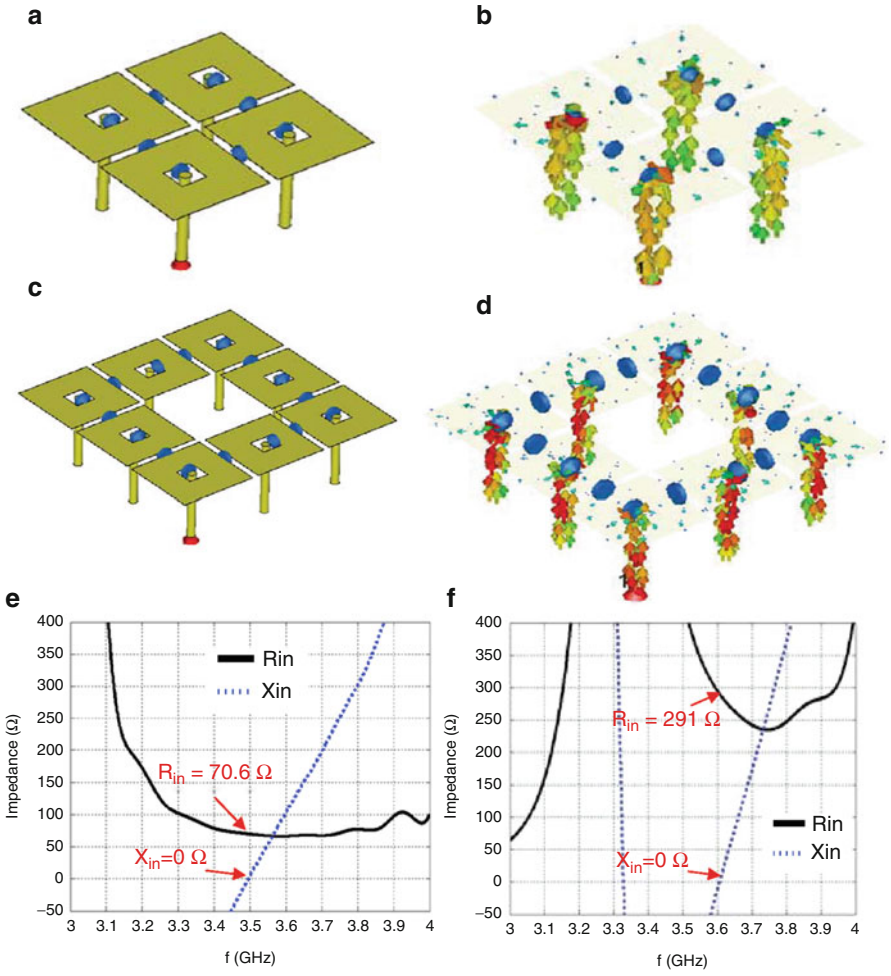

Fig. 15 (**a**) Zero-index metamaterial antenna geometry from Antoniades and Eleftheriades (2008b) with N = 4 unit cells, (**b**) current distribution at the resonant frequency of the antenna with N = 4 unit cells (all vias are in-phase), (**c**) antenna with N = 8 unit cells, (**d**) current distribution at the resonant frequency of the antenna with N = 8 unit cells (all vias are in-phase), (**e**) input impedance of the antenna with N = 4 unit cells, and (**f**) input impedance of the antenna with N = 8 unit cells. Note that the radiation resistance increases according to $R_{in} = N^2 R_r$ (Simulations courtesy of Dr. Aidin Mehdipour)

A Planar Dual-Mode NRI-TL Metamaterial-Loaded Monopole Antenna

In order to increase the bandwidth of the metamaterial antenna shown in the section "A Zero-Index NRI-TL Metamaterial Folded-Monopole Antenna," a natural extension is to create the aforementioned zero-index folded-monopole topology within the

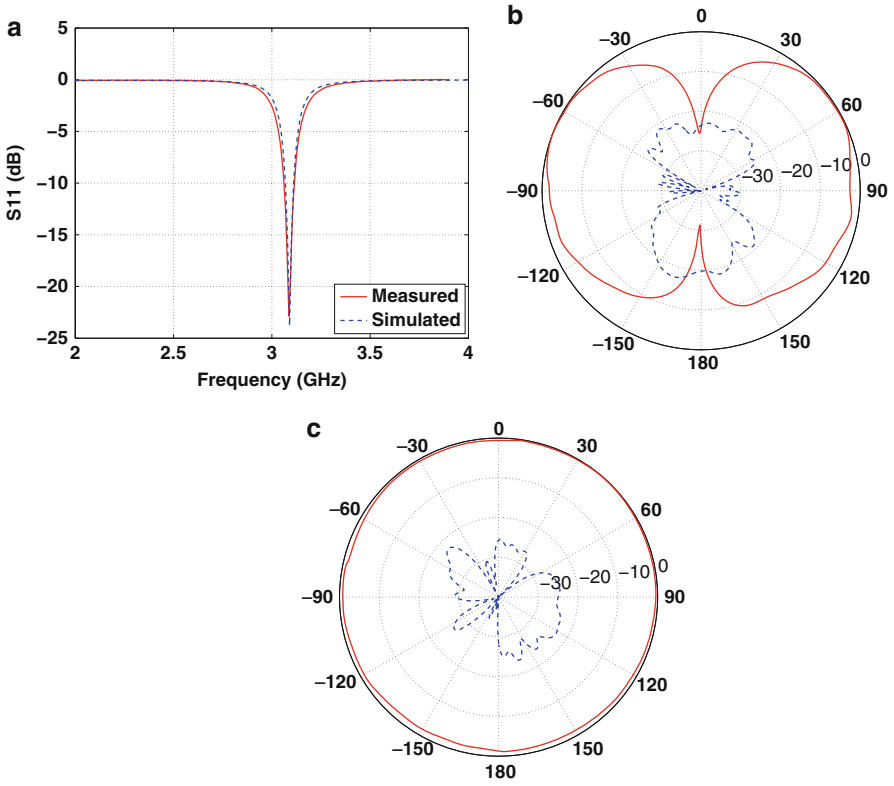

Fig. 16 (**a**) $|S_{11}|$ responses for the zero-index metamaterial antenna of Fig. 12. (**b**) E-plane (*xz*-plane) and (c) H-plane (*xy*-plane) measured radiation patterns at 3.1 GHz. *Solid line*: co-polarization, *dashed line*: cross-polarization (Antoniades and Eleftheriades 2008b) © 2008 IEEE

widely popular printed monopole structure. This suggests that the corresponding vertical monopole geometry of Fig. 12 is flattened into a single horizontal plane in line with the feed, which reduces significantly the height of the antenna. Figure 17 shows such a metamaterial-loaded antenna, where a single NRI-TL metamaterial unit cell has been integrated directly onto a printed monopole (Antoniades and Eleftheriades 2009).

The metamaterial unit cell was designed to operate at the $n = 0$ zeroth-order resonance under a closed stopband condition at a design frequency of $f_0 = 5.5$ GHz. Thus, at 5.5 GHz, the antenna acts as a folded monopole in the *x*-direction, while at 3.55 GHz, the metamaterial loading enables the top edge of the ground plane to act as a half-wavelength dipole in the orthogonal *y*-direction, effectively creating an additional $n = -1$ resonant mode. By virtue of the orthogonality between the two radiating modes, the metamaterial antenna exhibits an $|S_{11}|$ response with a dual resonance, as seen in Fig. 17b, and therefore a very wide measured -10 dB impedance bandwidth of 4.06 GHz.

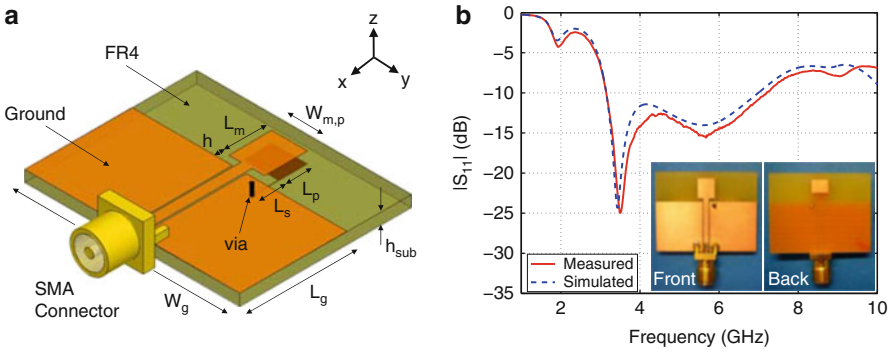

Fig. 17 (**a**) Planar dual-mode NRI-TL metamaterial-loaded monopole antenna. Dimensions (mm): $L_m = 6$, $W_m = 5$, $L_g = 15$, $W_g = 30$, h = 1, $L_p = 4$, $W_p = 5$, $L_s = 3.45$, $W_s = 0.1$, $h_{sub} = 1.59$, $S_{cpw} = 0.2$, $W_{cpw} = 1.55$, via diameter = 0.5. (**b**) $|S_{11}|$ responses for the metamaterial-loaded monopole antenna shown in the inset photographs (Antoniades and Eleftheriades 2009), © 2009 IEEE

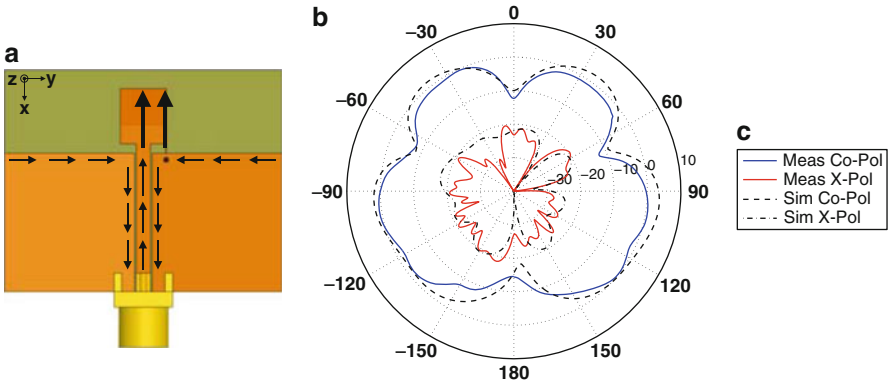

Fig. 18 (**a**) Simulated current distributions on the conductors of the metamaterial-loaded monopole antenna. (**b**) Radiation patterns in the *xy*-plane at 5.5 GHz. (**c**) Legend (Antoniades and Eleftheriades 2009), © 2009 IEEE

The dual-mode operation of the antenna can be explained by considering the current distribution on the metamaterial-loaded antenna at each of the resonant frequencies, as shown in Figs. 18a and 19a. At 5.5 GHz, the metamaterial-loaded monopole was designed to achieve a zero phase shift, $\phi_{\mathrm{MTM}} = 0°$; therefore, the currents along the monopole and along the bottom thin inductive strip were in phase. Thus, at this frequency, the metamaterial loading was used to create a two-arm folded monopole, similar to the four-arm folded monopole of the section "A Zero-Index NRI-TL Metamaterial Folded-Monopole Antenna." As was outlined above, by adjusting the value of the loading inductance L_0, it is possible to effectively eliminate the odd-mode current on the monopole, enabling the even-mode current along the *x*-direction to radiate, as shown in Fig. 18a. Additionally, at 5.5 GHz, the

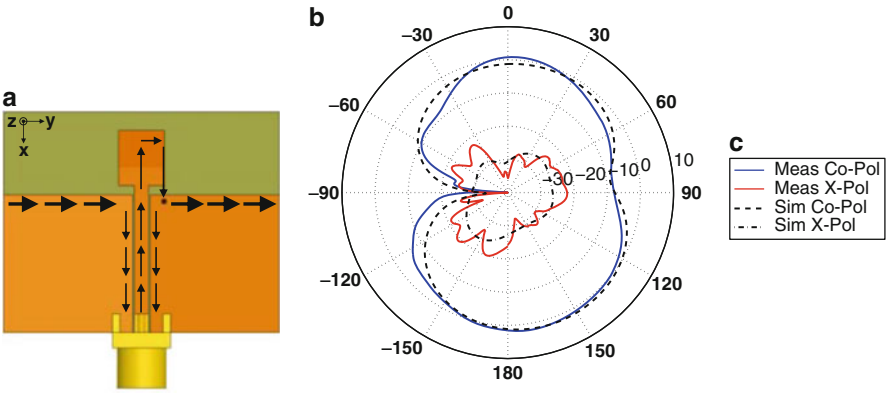

Fig. 19 (**a**) Simulated current distributions on the conductors of the metamaterial-loaded monopole antenna. (**b**) Radiation patterns in the *xy*-plane at 3.55 GHz. (**c**) Legend (Antoniades and Eleftheriades 2009), © 2009 IEEE

currents on the two ground planes are out of phase and the balanced CPW mode is preserved; therefore, these currents do not contribute to any radiation.

The radiation patterns in the *xy*-plane for the metamaterial-loaded antenna at 5.5 GHz are shown in Fig. 18b. Here, it can be observed that the antenna exhibits radiation patterns with a horizontal *x*-directed linear electric field polarization, consistent with *x*-directed currents along the monopole and the bottom thin inductive strip, shown in Fig. 18a. Thus, the radiation patterns verify that at 5.5 GHz the metamaterial loading of the monopole antenna enables it to operate as a short folded monopole.

At 3.55 GHz, the antenna no longer acts as a folded monopole along the *x*-axis, but rather as a dipole oriented along the *y*-axis. At this frequency, the metamaterial-loaded monopole acts as a balun for the ground plane currents, resulting in co-phased currents along the top edges of both the left and right ground plane sections, as shown in Fig. 19a. This renders the ground plane as the main radiating element at this frequency.

The radiation patterns in the *xy*-plane for the metamaterial-loaded antenna at 3.55 GHz are shown in Fig. 19b. At this frequency, the antenna exhibits radiation patterns with a horizontal *y*-directed linear electric field polarization, consistent with a *y*-directed current along the ground plane of the structure, as shown in Fig. 19a. Thus, the radiation patterns verify that at 3.55 GHz, the ground plane acts as the main radiating element for the antenna, providing an orthogonal polarization to the one observed at 5.5 GHz.

Thus, the metamaterial-loaded monopole antenna achieves a very-wide-band $|S_{11}|$ response by merging the resonances of the $n = 0$ zeroth-order resonant mode with the $n = -1$ resonant mode, which each provide orthogonal radiation patterns. The total size of the antenna is only $22 \times 30 \times 1.59$ mm, and the measured radiation efficiency is on the order of 90 % at both 3.55 GHz and 5.5 GHz. Furthermore, its

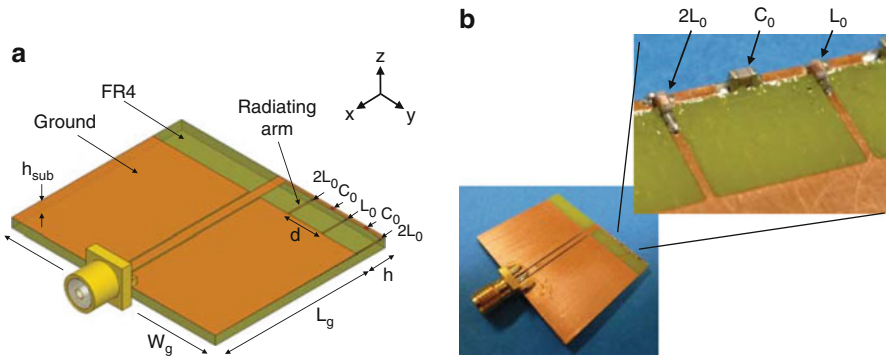

Fig. 20 Planar multi-mode NRI-TL metamaterial folded-monopole antenna. Dimensions (mm): $W_g = 36$, $L_g = 25$, $h = 5$, $d = 6$, $W_{cpw} = 1.55$, $S_{cpw} = 0.2$, $h_{sub} = 1.59$. Loading: $C_0 = 0.4$ pF, $L_0 = 12$ nH (Antoniades et al. 2013), © 2013 IEEE

compact and low-profile design is fully printed and does not require the use of any chip lumped-element components or an external matching network.

A Planar Multi-mode NRI-TL Metamaterial Folded-Monopole Antenna

Another related antenna that is based on a fully planar topology, but which is designed to excite multiple modes, is the folded-monopole antenna shown in Fig. 20 (Antoniades et al. 2013). Here, a coplanar waveguide (CPW) transmission line has been used to feed two NRI-TL metamaterial Π unit cells that are placed asymmetrically at the top right-hand side of the structure and which are implemented using surface-mount chip components. The shunt connections to the CPW ground plane form the thin radiating arms when the antenna is excited at its zero-index folded-monopole frequency.

The metamaterial unit cells were designed to operate under an open stopband condition with a $n = 0$ zeroth-order resonance frequency around 4 GHz. At this frequency, the currents are in phase on the thin radiating arms of each unit cell, and this allows the antenna to be treated as a short multi-arm folded monopole, enabling it to be matched to 50 Ω, even though the height of each arm is only $\lambda_0/14$. Similar to the antenna presented in the section "A Planar Dual-Mode NRI-TL Metamaterial-Loaded Monopole Antenna," Fig. 21a (top) shows the current distribution at 4.18 GHz, where it can be observed that indeed at this zero-index frequency, the currents on all of the radiating arms of the metamaterial unit cells, as well as the CPW feed line, are in phase and are along the x-direction. Figure 21a (bottom) shows the current distribution at 1.92 GHz, where it can be observed that at this frequency an orthogonal dipolar mode is excited along the y-direction, equivalent to the $n = -1$ resonant mode. These two resonances can be observed in the $|S_{11}|$ response shown in Fig. 21b, in addition to another two resonances at 0.98 GHz and 1.43 GHz. The resonance at 1.43 GHz is equivalent to the $n = -2$ mode, while the resonance at 0.98 GHz is a mode created by the CPW ground plane.

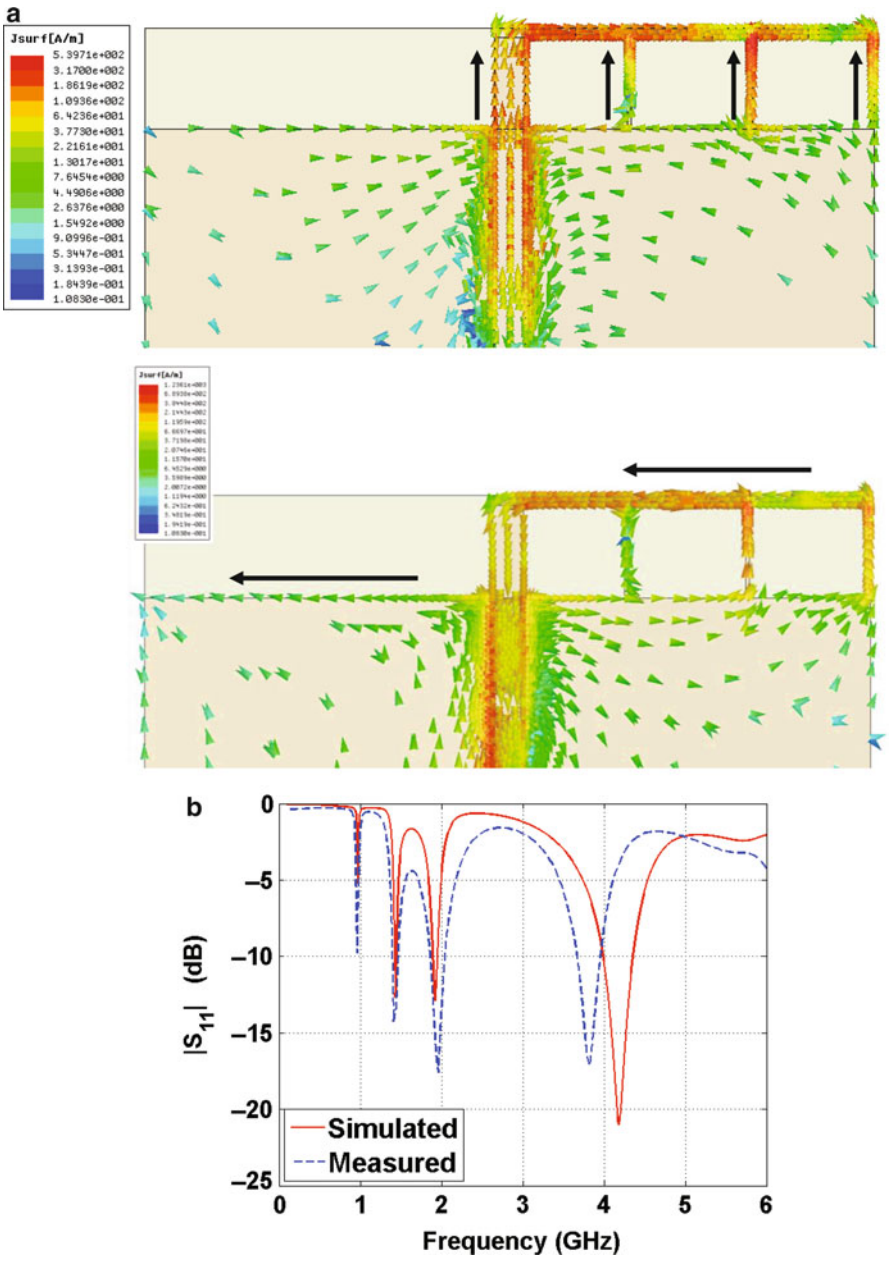

Fig. 21 (**a**) Simulated current distributions: (*top*) at 4.18 GHz, (*bottom*) at 1.92 GHz. (**b**) $|S_{11}|$ responses for the multi-mode folded-monopole antenna of Fig. 20 (Antoniades et al. 2013), © 2013 IEEE

The planar metamaterial folded-monopole antenna of Fig. 20 has a total size of $30 \times 36 \times 1.59$ mm^3, while the height of each radiating arm is only 5 mm. It exhibits three resonances that are matched below -10 dB, at 1.43 GHz, 1.95 GHz, and 3.81 GHz, with associated bandwidths of 25 MHz, 110 MHz, and 405 MHz, respectively, with measured radiation efficiencies in the range of 70–92 %.

Other Zeroth-Order Resonant Antennas

There are numerous other examples of antennas reported in the literature that have used the $n = 0$ zeroth-order resonance in their design to achieve beneficial characteristics such as size reduction, monopolar radiation, and multiband performance. Notable among these are the designs outlined below.

Among the fully printed designs, a compact monopole antenna with single-cell metamaterial loading is described in Zhu et al. (2010), in which a planar monopole antenna is loaded with a via-less NRI-TL metamaterial unit cell, similar to the antenna described in the section "A Planar Dual-Mode NRI-TL Metamaterial-Loaded Monopole Antenna," and a defected ground plane is used in order to achieve a tri-band response with high radiation efficiencies. A zeroth-order resonant antenna is presented in Lee (2011) that comprises two fully printed metamaterial unit cells implemented in an asymmetric coplanar waveguide configuration. The antenna achieves in-phase horizontally directed currents on both of its shunt inductive strips at the ZOR frequency, which results in radiation patterns with a horizontal linear electric field polarization analogous to that of a short dipole directed along the axis of the inductive strips. A compact zeroth-order resonant antenna based on a fully printed dual-arm spiral configuration is presented in Liu et al. (2012), which is very compact and also exhibits dipole-like radiation patterns, albeit with a narrow bandwidth. In Bertin et al. (2012), three versions of fully printed metamaterial-loaded monopoles are presented, which exhibit monopolar radiation patterns and multiband responses that cover the DCS-1800, UMTS, Wi-Fi, and part of the LTE frequency bands.

Several designs have also been reported that are based on the Sievenpiper mushroom structure (Sievenpiper et al. 1999). In Lai et al. (2007), a microstrip mushroom structure is used to implement one-dimensional infinite-wavelength resonant antennas with monopolar radiation patterns, which exhibit resonances at both the $n = -1$ and $n = 0$ ZOR frequencies. The mushroom structure of Lai et al. (2007) was further miniaturized in Baek and Lim (2009) by etching a spiral slot in the ground plane, thus increasing the value of the shunt inductive loading at the expense of degraded radiation patterns. A two-dimensional version of the mushroom structure is presented in Lee and Lee (2007), seen in Fig. 22a, and it is shown that this structure emulates a horizontal magnetic loop current over a perfect electric conductor, thus producing monopolar radiation patterns at its ZOR frequency. The $|S_{11}|$ response of the antenna, shown in Fig. 22b, exhibits a $n = 0$ zeroth-order resonance at around 7.8 GHz, in addition to $n = -2$, $n = -1$, $n = 1$, and $n = 2$ resonances.

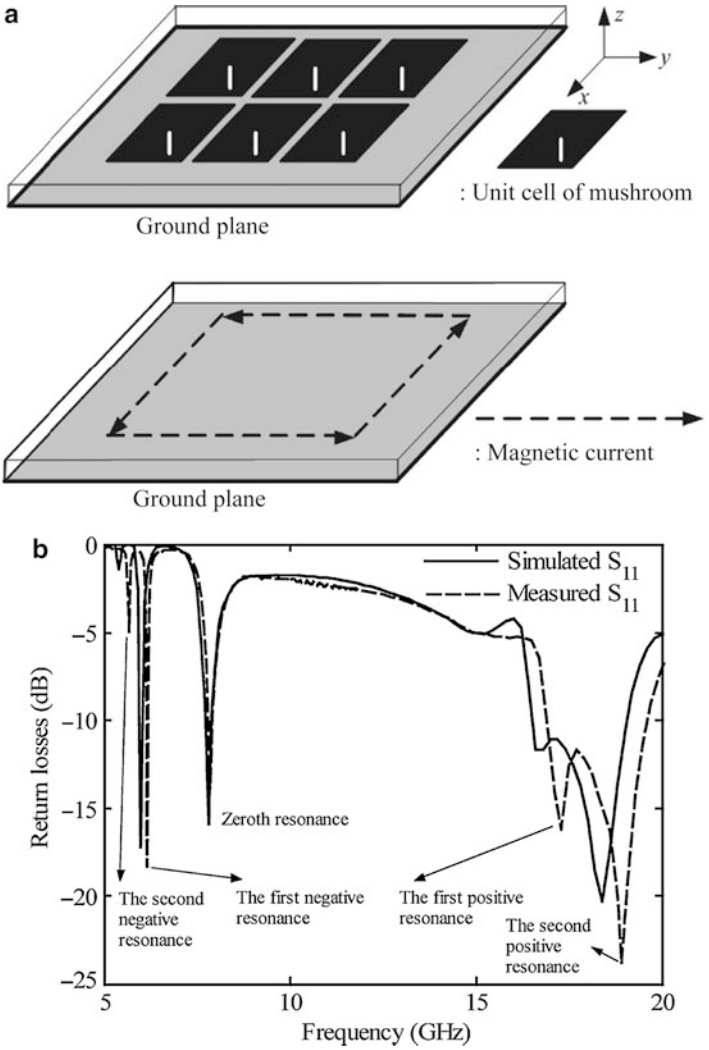

Fig. 22 (**a**) Proposed 3 × 2 mushroom ZOR antenna: (*top*) layout, (*bottom*) equivalent magnetic loop current. (**b**) $|S_{11}|$ responses (Lee and Lee 2007) © 2007 IEEE

Negative-Order Resonant Antennas, $n < 0$

A Compact Metamaterial-Loaded Patch Antenna

As outlined in the section "Resonant Characteristics of NRI-TL Metamaterials," when operated in the left-handed band, i.e., with negative-order resonances, NRI-TL metamaterials can be used to miniaturize the size of conventional antennas that

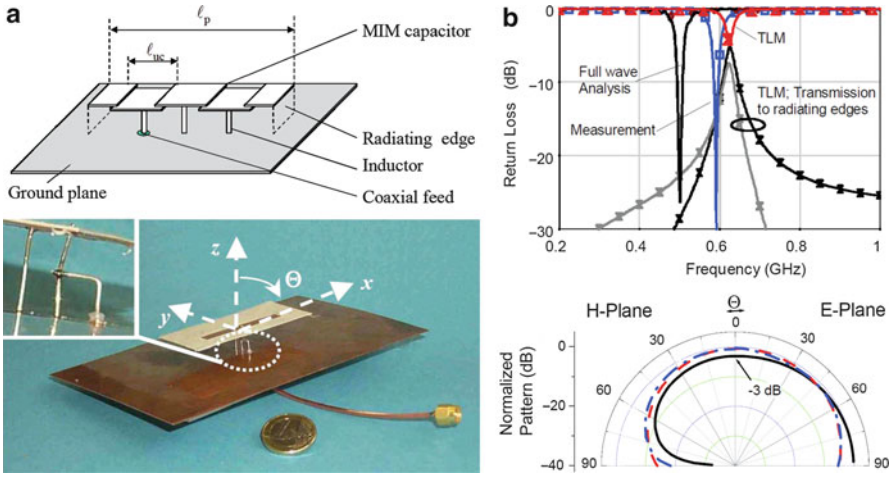

Fig. 23 (**a**) Compact metamaterial-loaded patch antenna. (**b**) (*Top*) $|S_{11}|$ response (*bottom*) normalized radiation patterns. *Black solid line*, simulated on an infinite ground plane; *red dotted line*, simulated on a finite ground plane; *blue dash-dot line*, measured on a finite ground plane (Schussler et al. 2004a) © 2004 IEEE

would normally require a resonant length of $\lambda/2$ to achieve a π phase shift across their length. Thus, the size of a conventional patch antenna that has a π phase shift between its two radiating edges can be significantly reduced by using NRI-TL metamaterials to achieve the equivalent $-\pi$ phase shift between its two radiating edges or equivalently the $n = -1$ resonant mode.

The first antenna described herein that employs the $n = -1$ resonant mode of NRI-TL metamaterials to shrink the physical size of a microstrip patch antenna is presented in Schussler et al. (2004a, b) and is shown in Fig. 23a. The fabricated prototype shown in Fig. 23a consists of two microstrip unit cells that are fed using a tapped-inductor feeding technique. Here, the shunt loading inductor L_0 has been realized using vertical wires and the series loading capacitor C_0 has been realized using a metal-insulator-metal (MIM) capacitor structure. The configuration of Fig. 23a can also be recognized as the one-dimensional version of the Sievenpiper mushroom structure, albeit with different loading compared to the $n = 0$ designs outlined in the section "Other Zeroth-Order Resonant Antennas."

The fabricated prototype of the metamaterial patch antenna has dimensions of $\lambda_0/40 \times \lambda_0/15 \times \lambda_0/40$ over a 0.6×0.6 mm^2 ground plane, and the $|S_{11}|$ response shown in Fig. 23b shows that the metamaterial patch antenna exhibits a simulated $n = -1$ resonance at 0.5 GHz with a -10 dB bandwidth of 1.5 %, while the measured resonance occurs at approximately 0.6 GHz. The measured radiation patterns in the E-plane (*xz*-plane) and the H-plane (*yz*-plane), also shown in Fig. 23b, indicate that the antenna radiates in the same manner as a conventional patch antenna, but with reduced efficiency and gain.

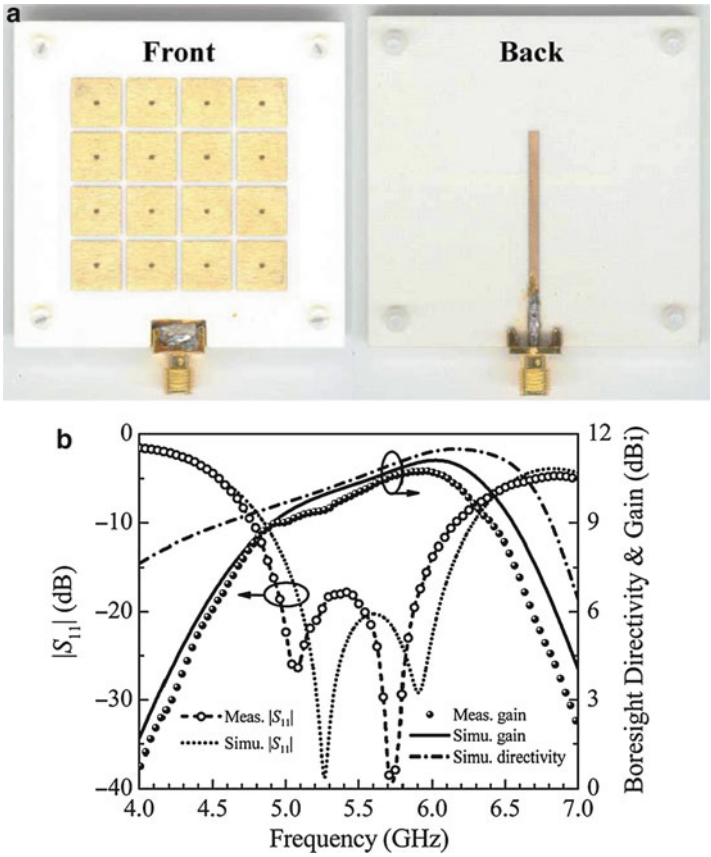

Fig. 24 (**a**) Photograph of the slot-fed metamaterial mushroom antenna. (**b**) $|S_{11}|$, directivity, and gain responses (Liu et al. 2014) © 2014 IEEE

A Metamaterial-Based Low-Profile Broadband Mushroom Antenna

A two-dimensional antenna that uses a negative-order resonance in order to achieve a π phase shift between its radiating edges is presented in Liu et al. (2014). The antenna, shown in Fig. 24a, is a Sievenpiper mushroom structure that consists of a 4 × 4 array of unit cells over a ground plane that is fed by a microstrip line through a slot cut into the ground plane. The distinguishing feature of this antenna is that by placing the feeding slot directly beneath the center gap between the mushroom cells, both the TM_{10} and the TM_{20} modes can be excited simultaneously at nonharmonic adjacent frequencies, thus providing a broadband $|S_{11}|$ response, as shown in Fig. 24b, while maintaining radiation at broadside throughout the operating band.

Figure 25a shows the simulated electric field distribution for the mushroom antenna at 4.97 GHz, where it can be observed that the field distribution resembles the TM_{10} mode of a conventional patch antenna. A notable difference, however, is

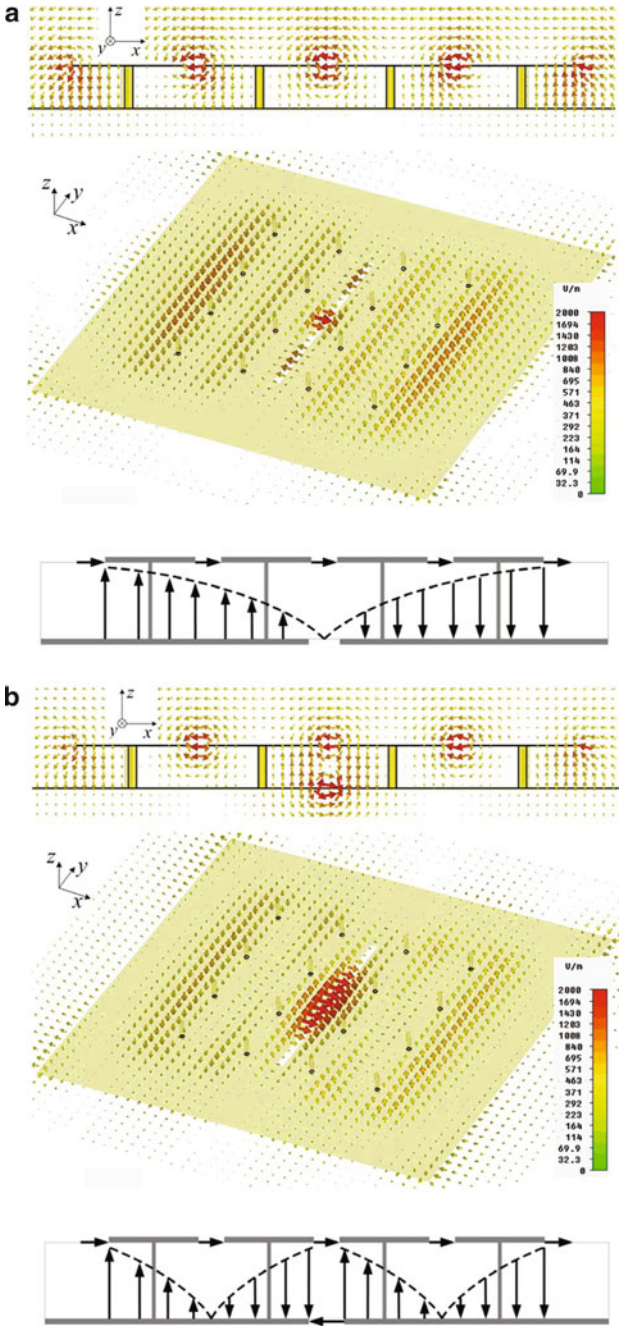

Fig. 25 (**a**) TM_{10} mode and (**b**) antiphase TM_{20} mode: (*top*) simulated E-field distribution, (*bottom*) sketch of the operating mechanism (Liu et al. 2014) © 2014 IEEE

that the electric fields in the gaps between the mushroom cells and at the radiating edges at the two open ends of the antenna are in phase, therefore producing radiation. Thus, the quality factor of the mushroom antenna decreases compared to the conventional patch antenna, leading to a bandwidth enhancement.

Figure 25b shows the simulated electric field distribution for the mushroom antenna at 5.98 GHz, where it can be observed that the field distribution resembles the antiphase TM_{20} mode of a conventional patch antenna. The slot excitation on the ground plane beneath the central mushroom gap enforces opposite electric fields across the central slot region, thus exciting the antiphase TM_{20} mode with out-of-phase E_z components in the central region. This, in turn, results in co-phased electric fields in the gaps between the mushroom cells and at the radiating edges at the two open ends of the antenna, therefore also producing radiation.

The metamaterial mushroom antenna of Fig. 24a has an overall size of $60 \times 60 \times 4.1$ mm^3 and attains a measured -10 dB bandwidth of 25 %, from 4.77 to 6.16 GHz, with an average gain of 9.9 dBi. Across the bandwidth, the measured antenna efficiency is greater than 76 %, and the cross-polarization levels are less than 20 dB.

Metamaterial-Loaded Substrate Integrated Waveguide Slot Antennas

Another type of antenna that uses negative-order resonances in order to achieve size miniaturization is shown in Fig. 26a (Dong and Itoh 2010). The miniaturized waveguide slot antenna consists of a substrate integrated waveguide (SIW) that has a slot etched on its surface. The slot acts as a series loading capacitor C_0 and forms the main radiating element, while the shunt inductive posts of the SIW provide the shunt inductive loading L_0, thus enabling this type of antenna to exhibit NRI-TL metamaterial characteristics. By operating the antenna at its negative-order resonant frequencies, which are well below the initial waveguide cutoff frequency, this leads to a significant degree of miniaturization. Two different versions of the antenna are presented, one which is open ended and one which is short ended, as shown in the prototypes on the bottom of Fig. 26a. The short-ended antenna, which represents a quasi-quarter-wavelength resonator, is essentially a cavity-backed slot antenna and therefore exhibits a high gain, while the open-ended antenna has a small size owing to its quasi-half-wavelength operation in the left-handed region.

The characteristics of a two-stage open-ended slot antenna are shown in Fig. 26b. From the $|S_{11}|$ responses, the multiband nature of the antenna can be observed, where the five resonances $n = -2$, $n = -1$, $n = 0$, $n = 1$, and $n = 2$ can be identified. The field distributions and radiation patterns for the $n = -2$ and $n = -1$ modes shown on the bottom of Fig. 26b indicate that the antenna can exhibit both dipolar and patch-type radiation characteristics at closely spaced resonant frequencies. The measured bandwidths of the antennas range from 1.5 % to 2.6 %, the measured gain from 3.2 to 6.8 dBi, and the measured efficiencies from 77 % to 91 %. The overall sizes of the antennas range from $0.265\lambda_0 \times 0.318\lambda_0 \times 0.03\lambda_0$ to $0.506\lambda_0 \times 0.343\lambda_0 \times 0.03\lambda_0$.

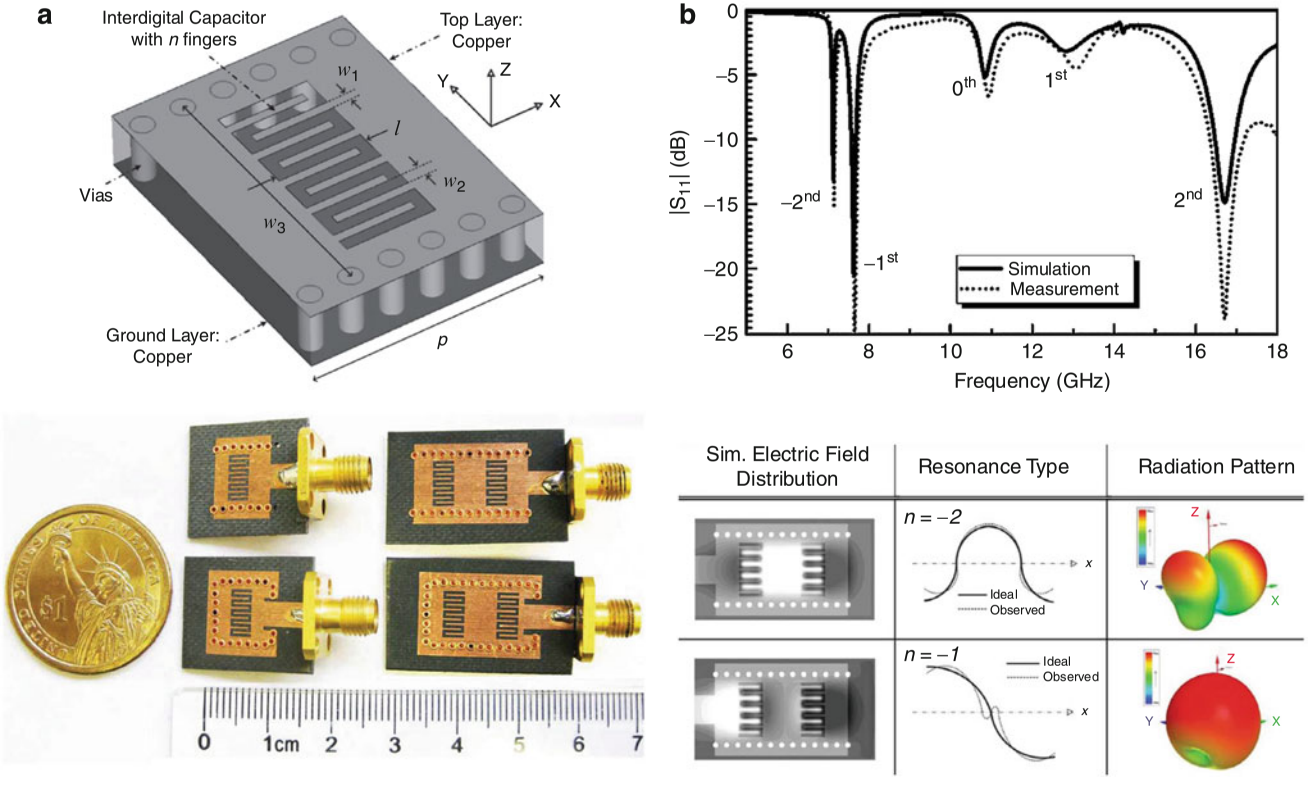

Fig. 26 (**a**) Metamaterial-loaded substrate integrated waveguide slot antennas, (**b**) $|S_{11}|$ responses, simulated electric field distributions, and radiation patterns at the $n = -2$ and $n = -1$ resonances (Dong and Itoh 2010) © 2010 IEEE

Other Negative-Order Resonant Patch Antennas

Various other metamaterial patch antennas have been reported in the literature that exploit the advantages of negative-order resonances that NRI-TL metamaterials have to offer (Lee et al. 2006; Tretyakov and Ermutlu 2005; Alu et al. 2007; Herraiz-Martinez et al. 2008a; Wang et al. 2010; Dong et al. 2011). One- and two-dimensional versions of metamaterial patch antenna designs that have used negative-order resonances to achieve size reduction and multiband responses have been shown in Lee et al. (2006). Additionally, in Tretyakov and Ermutlu (2005), a theoretical analysis has been presented on the benefits of using transmission-line-based metamaterials to create patch antennas with enhanced bandwidth characteristics and reduced size. Finally, in Alu et al. (2007), the possibility of designing sub-wavelength resonant patch antennas using metamaterials has been theoretically analyzed, and it is demonstrated that these designs may exhibit in principle an arbitrarily low resonant frequency for a fixed dimension, but they may not necessarily radiate efficiently when their size is electrically small. By employing a circular patch geometry, it has been shown that specific modes can be selected that enable the patch antenna to be compact, but yet exhibit comparable radiation performance to that of a conventional patch antenna of standard dimensions.

Epsilon-Negative (ENG) Antennas

Another transmission-line-based metamaterial structure that supports a zeroth-order resonant mode is the so-called epsilon-negative (ENG) structure shown in Fig. 27a in its distributed form and in Fig. 27b in its lumped-element form. It can be observed that this topology is simply an NRI-TL metamaterial unit cell from Fig. 3 with the series loading capacitor C_0 removed, resulting in a shunt inductor-loaded transmission line.

Considering the dispersion diagram of Fig. 11, it has been outlined in the section "Resonant Characteristics of NRI-TL Metamaterials" that the NRI-TL metamaterial structure exhibits two $n = \pm 0$ zeroth-order resonant frequencies f_{-0} and f_{+0}, which can be adjusted by changing the values of the loading elements L_0 and C_0, according

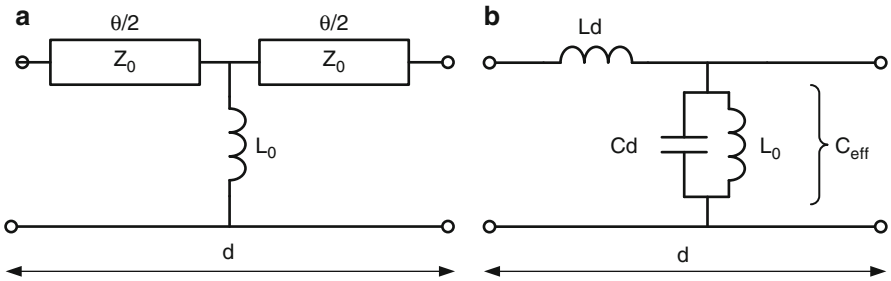

Fig. 27 Epsilon-negative (ENG) metamaterial unit cell: (**a**) symmetric distributed equivalent circuit, (**b**) lumped-element equivalent circuit

to Eqs. 8 and 9. Removing the series loading capacitor C_0 is equivalent to letting its value go to infinity, $C_0 = \infty$; therefore, the zeroth-order resonant frequencies become

$$f_{-0} = 0, \tag{33}$$

$$f_{+0} = \frac{1}{2\pi\sqrt{L_0(Cd)}}. \tag{34}$$

These results indicate that the ENG metamaterial structure has only one zeroth-order resonant frequency, which is determined by the values of the shunt elements in the unit cell of Fig. 27b. Therefore, for a fixed length of host transmission line, the zeroth-order resonant frequency f_{+0} can be easily tuned by simply adjusting the value of the loading inductance L_0. Additionally, like the NRI-TL metamaterial structure, the zeroth-order resonant frequency of the ENG structure is also independent of its physical length; however, since the loading capacitor C_0 has been eliminated, this allows larger degrees of antenna miniaturization to be achieved.

The dispersion relation for the ENG metamaterial structure of Fig. 27a can be obtained by setting $C_0 = \infty$ in the dispersion relation of the NRI-TL metamaterial structure given by Eq. 1 and can be written as

$$\cos(\beta_{\mathrm{BL}}d) = \cos(\theta) + \left(\frac{Z_0}{2\omega L_0}\right)\sin(\theta). \tag{35}$$

Under the effective medium conditions $\theta \ll 1$ and $\beta_{\mathrm{BL}}d \ll 1$, Eq. 35 becomes

$$\cos(\beta_{\mathrm{BL}}d) \approx 1 - \frac{1}{2}\left(\omega^2 LCd^2 - \frac{Ld}{L_0}\right). \tag{36}$$

Using Eq. 7, the effective propagation constant of the ENG metamaterial structure can be written as

$$\beta_{\mathrm{ENG}} = \omega\sqrt{L_{\mathrm{eff}}C_{\mathrm{eff}}} = \omega\sqrt{L\left[C - \frac{1}{\omega^2 L_0 d}\right]}, \tag{37}$$

$$\beta_{\mathrm{ENG}} = \sqrt{\omega^2 LC - \frac{L}{L_0 d}}. \tag{38}$$

Equation 37 demonstrates that with the appropriate value of the shunt inductor L_0, the effective shunt capacitance C_{eff} of the ENG structure (see Fig. 27b) can be made equal to zero, resulting in a zero propagation constant and therefore a zeroth-order resonance. Exactly at the zeroth-order resonance frequency f_{+0}, the effective permittivity of the structure is equal to zero and is therefore termed the epsilon-zero (EZR) point.

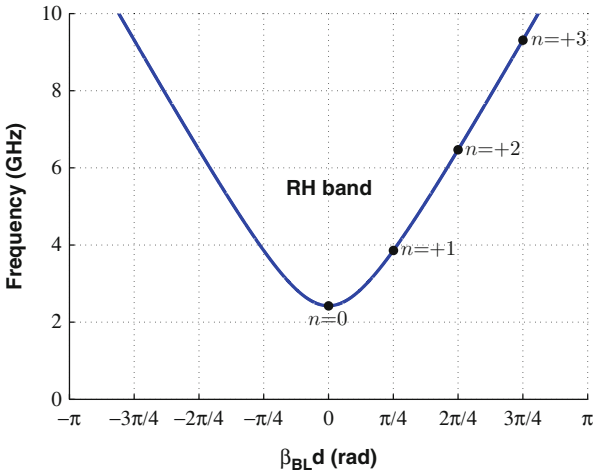

Fig. 28 Typical dispersion diagram for an ENG metamaterial unit cell with parameters $L_0 = 30$ nH, $Z_0 = 300\ \Omega$, $d = 12.5$ mm, and $\theta = 45^\circ$ at 3 GHz. Superimposed are the locations of the nth order resonances for an ENG metamaterial structure that consists of a cascade of $N = 4$ unit cells

A representative ENG dispersion diagram is shown in Fig. 28, which was obtained using Eq. 35 and the same parameters as the NRI-TL metamaterial structure in Fig. 11. It can be observed that the ENG structure exhibits a lower stopband and a forward right-handed propagation band, and the backward left-handed band has been eliminated. Thus, unlike the NRI-TL structure which supports both forward and backward waves, the ENG structure supports only forward propagating waves, similar to a conventional transmission line. However, unlike a transmission line, propagation on the ENG structure begins above the zeroth-order resonance frequency of f_{+0} given approximately by Eq. 34; therefore, it exhibits a high-pass behavior with a DC offset.

In the general case where N unit cells are used in order to implement the ENG metamaterial structure with a total length of $\ell_{\mathrm{TOT}} = Nd$, then the electrical length per unit cell, analogous to Eq. 21, becomes

$$\beta_{\mathrm{ENG}} d = \frac{n\pi}{N} \quad ; \quad n = 0, 1, 2 \ldots (N-1) \tag{39}$$

An N-stage ENG metamaterial structure can therefore support a zeroth-order ($n = 0$) resonance at the $\beta_{\mathrm{BL}} d = 0$ point, as well as positive-order ($n > 0$) resonances in the right-handed band, as shown in Fig. 28.

A Double-Resonant ENG Metamaterial Folded-Monopole Antenna

An example of an ENG metamaterial-based compact antenna is shown in Fig. 29 (Zhu and Eleftheriades 2009b). It uses the same folding technique and has a similar form to the NRI-TL metamaterial folded-monopole antenna described in the section "A Zero-Index NRI-TL Metamaterial Folded-Monopole Antenna"; however, it is implemented using ENG metamaterial unit cells. Recall that for the NRI-TL folded monopole, the shunt loading inductor L_0 was responsible for maximizing the even-mode current, and the series loading capacitor C_0 did not play a pivotal role in this

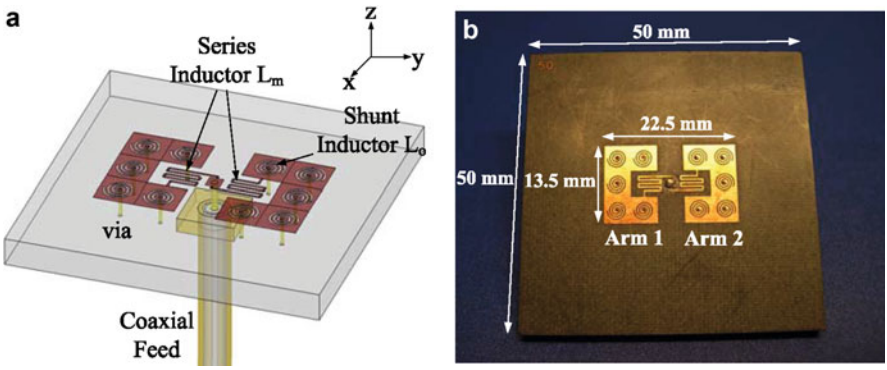

Fig. 29 Double-resonant ENG metamaterial folded-monopole antenna: (**a**) three-dimensional diagram, (**b**) photograph of the fabricated prototype (Zhu and Eleftheriades 2009b) © 2009 IEEE

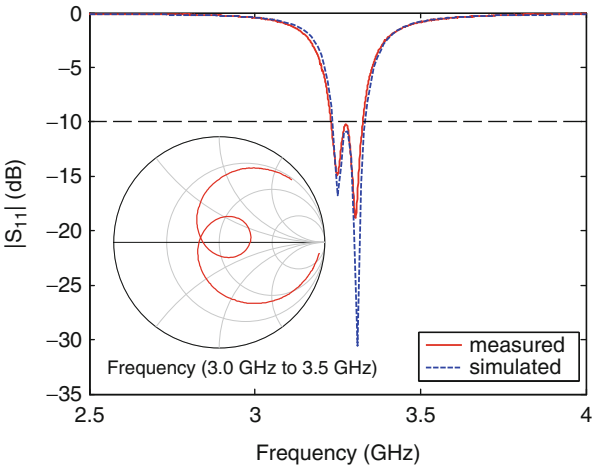

Fig. 30 $|S_{11}|$ responses for the ENG metamaterial antenna of Fig. 29 (Zhu and Eleftheriades 2009b) © 2009 IEEE

process. Therefore, the elimination of the series loading capacitor C_0 in the ENG structure does not affect the ability of the antenna to act as a folded monopole, and the even-mode current is still maximized. Moreover, the ENG folded-monopole antenna of Fig. 29 employs a doubly resonant metamaterial structure in order to increase its bandwidth. The antenna consists of two ENG metamaterial arms, and each arm is designed to exhibit zeroth-order resonances at two closely spaced frequencies. Each arm comprises a microstrip transmission line loaded with five shunt spiral inductors, whose zero-index frequency can be tuned by adjusting the value of the loading inductors. A wideband performance is achieved by merging the corresponding two resonances together into a single passband.

The antenna has dimensions of $\lambda_0/4 \times \lambda_0/7 \times \lambda_0/29$ over a $0.55\lambda_0 \times 0.55\lambda_0$ ground plane. A series meander-line inductor is employed at the feed point to compensate the capacitive input impedance, thus achieving a good impedance match to 50 Ω over a 100 MHz −10 dB measured $|S_{11}|$ bandwidth around 3.3 GHz, as shown in Fig. 30.

The antenna also exhibits a vertical linear electric field polarization, similar to that of a short monopole over a small ground plane, a measured gain of 0.79 dBi, and a measured radiation efficiency of 66 %.

Other Epsilon-Negative (ENG) Antennas

Various other ENG metamaterial antennas have been reported in the literature (Lai et al. 2007; Park et al. 2007; Park and Lee 2011; Niu et al. 2013; Niu and Feng 2013; Kim et al. 2009). In Lai et al. (2007), an inductor-loaded transmission line, essentially a one-dimensional microstrip mushroom structure without the series gaps between each of the unit cells, is used to implement a one-dimensional infinite-wavelength resonant antenna with monopolar radiation patterns at the $n = 0$ ZOR frequency. This antenna was then extended to a two-dimensional version in order to increase the gain and to reduce asymmetries in the radiation patterns. In Park et al. (2007), also a one-dimensional mushroom structure without the series gaps is investigated for different unit cell sizes with good gain performance. Finally, in Niu et al. (2013), a fully planar ENG antenna is presented that is implemented in asymmetric coplanar waveguide technology and which achieves dual-band and wideband performance by exciting both the $n = 0$ and the $n = 1$ resonant modes.

Mu-Negative (MNG) Antennas

Another transmission-line-based metamaterial structure that supports a zeroth-order resonant mode, which is also a variation of the NRI-TL metamaterial structure, is the so-called mu-negative (MNG) structure shown in Fig. 31a in its distributed form and in Fig. 31b in its lumped-element form. It can be observed that this topology is simply an NRI-TL metamaterial unit cell from Fig. 3 with the shunt loading inductor L_0 removed, resulting in a series capacitor-loaded transmission line.

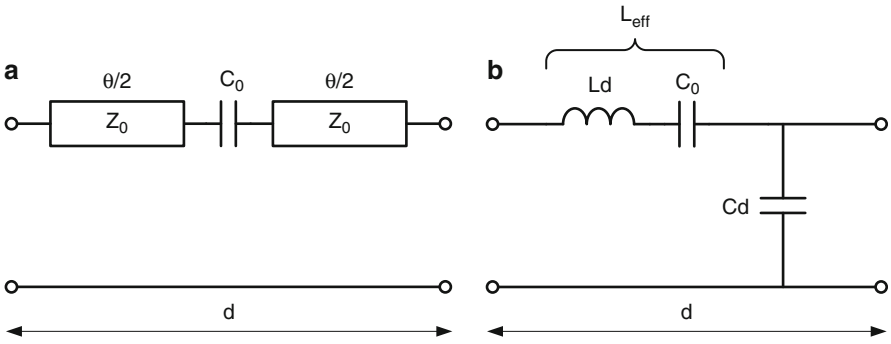

Fig. 31 Mu-negative (MNG) metamaterial unit cell: (**a**) symmetric distributed equivalent circuit, (**b**) lumped-element equivalent circuit

Removing the shunt loading inductor L_0 from the NRI-TL metamaterial structure is equivalent to letting its value go to infinity, $L_0 = \infty$; therefore, from Eqs. 8 and 9, the zeroth-order resonant frequencies for the MNG metamaterial become

$$f_{-0} = 0, \tag{40}$$

$$f_{+0} = \frac{1}{2\pi\sqrt{(Ld)C_0}}. \tag{41}$$

These results indicate that the MNG metamaterial structure, like the ENG structure, has only one zeroth-order resonant frequency, which is determined by the values of the series elements in the unit cell of Fig. 31b. Therefore, for a fixed length of host transmission line, the zeroth-order resonant frequency f_{+0} can be easily tuned by simply adjusting the value of the loading capacitance C_0. Additionally, like the NRI-TL metamaterial structure, the $n = 0$ zeroth-order resonant frequency of the MNG structure is also independent of its physical length; however, since the loading inductor L_0 has been eliminated, this allows larger degrees of antenna miniaturization to be achieved.

The dispersion relation for the MNG metamaterial structure of Fig. 31a can be obtained by setting $L_0 = \infty$ in the dispersion relation of the NRI-TL metamaterial structure given by Eq. 1 and can be written as

$$\cos(\beta_{\mathrm{BL}}d) = \cos(\theta) + \left(\frac{1}{2\omega C_0 Z_0}\right)\sin(\theta). \tag{42}$$

Under the effective medium conditions $\theta \ll 1$ and $\beta_{\mathrm{BL}}d \ll 1$, Eq. 42 becomes

$$\cos(\beta_{\mathrm{BL}}d) \approx 1 - \frac{1}{2}\left(\omega^2 LCd^2 - \frac{Ld}{C_0}\right). \tag{43}$$

Using Eq. 7, the effective propagation constant of the MNG metamaterial structure can be written as

$$\beta_{\mathrm{MNG}} = \omega\sqrt{L_{\mathrm{eff}}C_{\mathrm{eff}}} = \omega\sqrt{\left[L - \frac{1}{\omega^2 C_0 d}\right]C}, \tag{44}$$

$$\beta_{\mathrm{MNG}} = \sqrt{\omega^2 LC - \frac{C}{C_0 d}}. \tag{45}$$

Equation 44 demonstrates that with the appropriate value of the series capacitor C_0, the effective series inductance L_{eff} of the MNG structure (see Fig. 31b) can be made equal to zero, resulting in a zero propagation constant and therefore a zeroth-order resonance. Exactly at the zeroth-order resonance frequency f_{+0}, the effective permeability of the structure is equal to zero and is therefore termed the mu-zero (MZR) point.

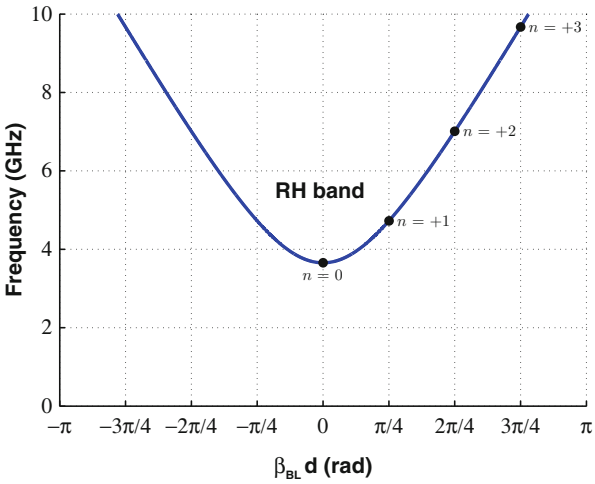

Fig. 32 Typical dispersion diagram for an MNG metamaterial unit cell with parameters $C_0 = 0.14$ pF, $Z_0 = 300\ \Omega$, $d = 12.5$ mm, and $\theta = 45^\circ$ at 3 GHz. Superimposed are the locations of the nth order resonances for an MNG metamaterial structure that consists of a cascade of $N = 4$ unit cells

A representative MNG dispersion diagram is shown in Fig. 32, which was obtained using Eq. 42 and the same parameters as the NRI-TL metamaterial structure in Fig. 11. It can be observed that the MNG structure exhibits a very similar response to the ENG structure, with a lower stopband and a forward right-handed propagation band, and the backward left-handed band has been eliminated. Thus, unlike the NRI-TL structure which supports both forward and backward waves, and similar to the ENG structure, the MNG structure supports only forward propagating waves, similar to a conventional transmission line. However, unlike a transmission line, propagation on the MNG structure begins above the zeroth-order resonance frequency of f_{+0} given approximately by Eq. 41; therefore, it exhibits a high-pass behavior with a DC offset. Note also that by comparing the three dispersion diagrams shown in Figs. 11, 28, and 32, the location of the $n = -0$ resonance for the NRI-TL structure corresponds to the $n = 0$ resonance of the ENG structure, and the location of the $n = +0$ resonance for the NRI-TL structure corresponds to the $n = 0$ resonance of the MNG structure.

In the general case where N unit cells are used in order to implement the MNG metamaterial structure with a total length of $\ell_{\mathrm{TOT}} = Nd$, then the electrical length per unit cell, analogous to Eq. 21, becomes

$$\beta_{\mathrm{MNG}} d = \frac{n\pi}{N} \quad ; \quad n = 0, 1, 2, \ldots (N-1) \tag{46}$$

An N-stage MNG metamaterial structure can therefore support a zeroth-order ($n = 0$) resonance at the $\beta_{\mathrm{BL}} d = 0$ point, as well as positive-order ($n > 0$) resonances in the right-handed band, as shown in Fig. 32.

A Dual-Band MNG Metamaterial Loop Antenna

An example of a dual-band MNG metamaterial loop antenna is shown in Fig. 33a (Park et al. 2010). It uses a microstrip transmission line that is loaded with series

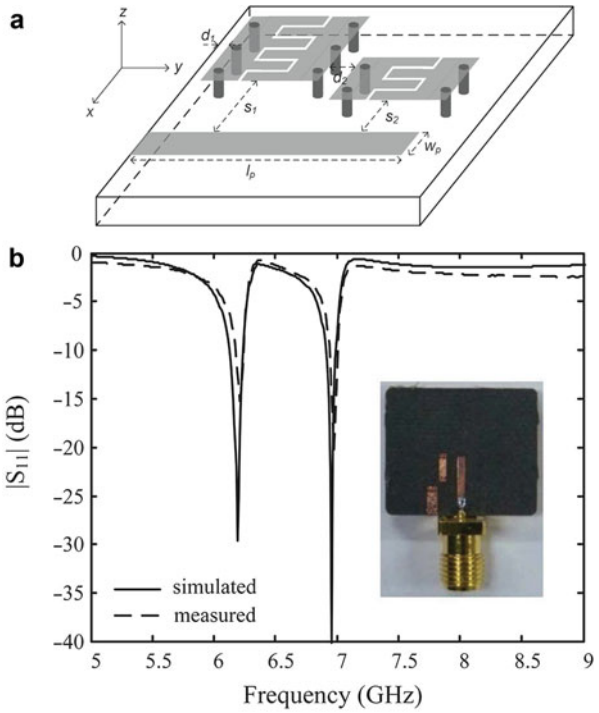

Fig. 33 (**a**) Dual-band MNG metamaterial loop antenna, (**b**) $|S_{11}|$ responses (Park et al. 2010) © 2010 IEEE

interdigital capacitors in order to implement the MNG metamaterial unit cells. Interdigital capacitors with different finger numbers were investigated, and it was found that ones with a higher number of fingers result, as expected, in a larger series loading capacitance, C_0, and therefore a lower zeroth-order resonance frequency. However, the trade-off of implementing a larger loading capacitance is a larger size.

It is noted that because the zeroth-order resonance for the MNG structure is obtained at the resonant frequency of the series branch of the MNG structure of Fig. 31b, short-circuit boundary conditions are necessary at the ends of an MNG resonant structure in order to support a resonance. This is in contrast to ENG resonant structures, which require open-circuit boundary conditions in order to support a zeroth-order resonance, which is due to the shunt branch of the ENG structure, as seen in Fig. 27b. The MNG antenna is therefore formed by short-circuiting a capacitively loaded microstrip transmission line at its two ends with metallic vias, and it is fed using a microstrip line that magnetically couples into the resulting loop. The microstrip feed line is open ended and is designed to have a length equal to a quarter wavelength at the antenna's zeroth-order resonant frequency. The use of the microstrip feed line therefore limits the minimum achievable size for the MNG antenna to a quarter wavelength.

A dual-band antenna is created by adding a second MNG structure with a different size, and therefore a different zeroth-order resonance, to the same feed line, as shown in Fig. 33a. In this design, the first MNG structure consists of a single

unit cell that has an interdigital capacitor with six fingers that resonate at a frequency of 6.2 GHz, and the second MNG structure also consists of a single unit cell that has an interdigital capacitor with four fingers that resonate at a frequency of 7 GHz. The distance between each of the MNG structures and the feed line was optimized in each case in order to maximize the coupling to each of the resonators.

The $|S_{11}|$ response of the antenna is shown in Fig. 33b, where the dual-band performance can be observed. The MNG antenna achieves 1.03 % and 0.95 % fractional bandwidths at 6.2 GHz and 7 GHz, respectively, with associated measured gains of 2.3 dBi and 3.3 dBi and efficiencies of 83 % and 84 %. The size of the antenna is $0.108\lambda_0 \times 0.175\lambda_0$ at 6.2 GHz and $0.121\lambda_0 \times 0.197\lambda_0$ at 7 GHz.

Other Mu-Negative (MNG) Antennas

Various other MNG metamaterial antennas have been reported in the literature (Bilotti et al. 2008; Wei et al. 2012a, b). In Bilotti et al. (2008), the size reduction of a circular patch antenna that is printed on a substrate that is partially with an MNG metamaterial is theoretically investigated. It is shown that a sub-wavelength metamaterial patch antenna can be achieved with satisfactory matching and radiating performance by employing split-ring resonators as the magnetic inclusions beneath the patch antenna. In Wei et al. (2012a, b), two versions of MNG loop antennas are presented, which consist of circular loop antennas that are periodically loaded with capacitors. This configuration enables uniform, in-phase current along the loop, therefore achieving a horizontally polarized omnidirectional radiation pattern, similar to a magnetic dipole antenna, even though the perimeter of the loop is comparable to the operating wavelength. Additionally, the capacitive loading enables a wide impedance bandwidth to be achieved.

NRI-TL Metamaterial Dipole Antennas

Most of the metamaterial antenna applications that have been described so far have been based on folded monopoles, printed monopoles, and patch antennas. Another type of antenna that can be designed based on metamaterial techniques, and which exhibits negative-order, zeroth-order, and positive-order resonances, is the differentially fed dipole antenna.

Some examples of metamaterial-loaded dipole antennas that have been reported in the literature are Ziolkowski and Erentok (2006), Jin and Ziolkowski (2010), Herraiz-Martinez et al. (2008b, 2011), Iizuka and Hall (2007), Liu et al. (2009), and Antoniades and Eleftheriades (2011a, b, 2012). In Ziolkowski and Erentok (2006), an electrically small electric dipole antenna was surrounded by a negative-permittivity shell, and it was demonstrated that the distributed inductance of the shell could be resonantly matched to the capacitive electrically small dipole. Thus, a resonant system was achieved which was matched to the source impedance, therefore leading to high overall efficiencies. Metamaterial-engineered planar dipole antennas have also been presented in Jin and Ziolkowski (2010), which have linear or circular polarizations. Another idea presented in Herraiz-Martinez

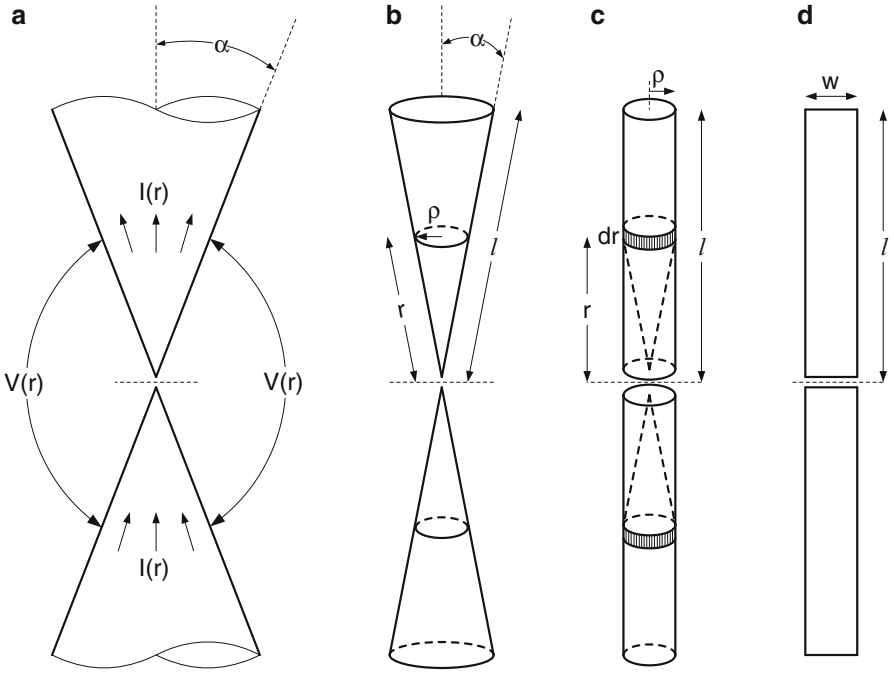

Fig. 34 The evolution of Schelkunoff's infinite biconical antenna into a planar dipole antenna. (**a**) Infinite biconical antenna, (**b**) finite biconical antenna, (**c**) cylindrical dipole antenna, and (**d**) planar dipole antenna (Antoniades and Eleftheriades 2012) © 2012 IEEE

et al. (2008b) demonstrated that a printed dipole antenna that is loaded with split-ring resonators can achieve a dual-band $|S_{11}|$ response.

The authors in Iizuka and Hall (2007) and Liu et al. (2009) have demonstrated that creating a dipole antenna from an asymmetrically loaded left-handed transmission line leads to a difference in the amplitudes of the out-of-phase currents on each of the transmission-line conductors. Therefore, the two currents do not completely cancel each other out in the far field, enabling the structure to radiate. Even though a multiband $|S_{11}|$ response is achieved, the reported efficiency and gain of the antennas in Iizuka and Hall (2007) are quite low, due to the partial cancelation of the current, combined with the presence of material losses in the printed components. In Liu et al. (2009), the authors have optimized the design of the left-handed dipoles in order to improve the efficiency of their antennas.

Herein, a technique is adopted for the design of a metamaterial-loaded dipole antenna that does not rely on an asymmetrically loaded transmission line in order to create an unbalanced radiating current. Instead, in an approach initially proposed by Schelkunoff, the two arms of a dipole antenna are modeled as the two conductors of a biconical transmission line. The biconical transmission line can subsequently be transformed into its equivalent dipole counterpart through the process shown in Fig. 34. This allows the dipole antenna to be treated as the host transmission line in a

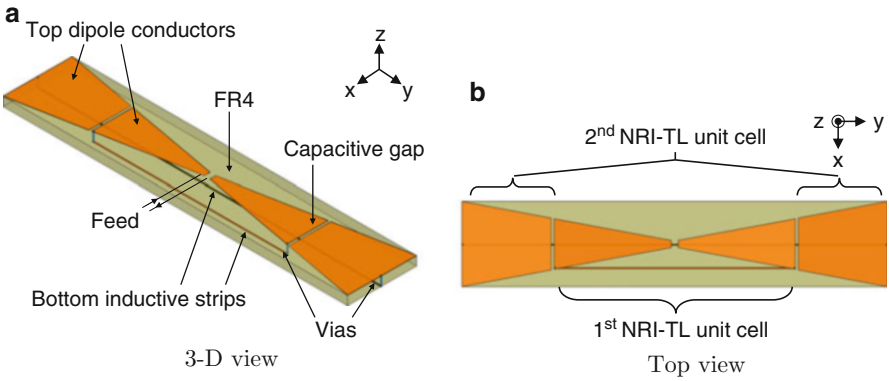

Fig. 35 NRI-TL metamaterial-loaded dipole antenna, consisting of two NRI-TL unit cells loading a printed dipole antenna (Antoniades and Eleftheriades 2012) © 2012 IEEE

conventional NRI-TL metamaterial structure and provides a suitable medium for the placement of the loading elements. As such, the NRI-TL properties of the structure are maintained, while still creating an efficient radiator.

The proposed NRI-TL metamaterial-loaded dipole antenna is shown in Fig. 35 (Antoniades and Eleftheriades 2012). It consists of a planar dipole antenna on an FR4 substrate in the shape of a bow tie with a small flare angle, two series capacitive gaps forming the loading capacitance C_0, and two shunt inductive strips forming the loading inductance L_0, resulting a two-unit-cell metamaterial-loaded dipole antenna.

Referring to Fig. 35, the first NRI-TL unit cell is formed by the two central dipole conductors connected to the feed, which are joined at their ends through two vias to a thin inductive strip on the bottom of the substrate. Thus, the two central dipole conductors effectively form a transmission line with a characteristic impedance Z_{01} and length l_1 which is inductively loaded at its end with a thin inductive strip with an inductance L_{01}. Since the dipole arms have a finite length, Schelkunoff showed that this can be modeled as a terminal impedance, Z_{t1}, connected to the end of the transmission line. Therefore, this terminal impedance must be added in parallel to the impedance of the thin inductive strip. The transmission line is also connected to a series capacitance $2C_{01}$, formed in part due to the capacitive gaps in each of the dipole arms.

The second NRI-TL unit cell is formed by the two outer dipole conductors, which are also joined at their ends through two vias to a longer thin inductive strip, which was centered on the bottom of the board. Thus, the two outer dipole conductors effectively form another transmission line with a characteristic impedance Z_{02} and length l_2, which is inductively loaded at its end with a longer inductive strip with an inductance L_{02}. To the impedance of the thin inductive strip, the terminal impedance, Z_{t2}, of the finite dipole arms must be added as with the first unit cell. The transmission line is also connected at its input to a series capacitance $2C_{02}$, formed in part due to the capacitive gaps in each of the dipole arms.

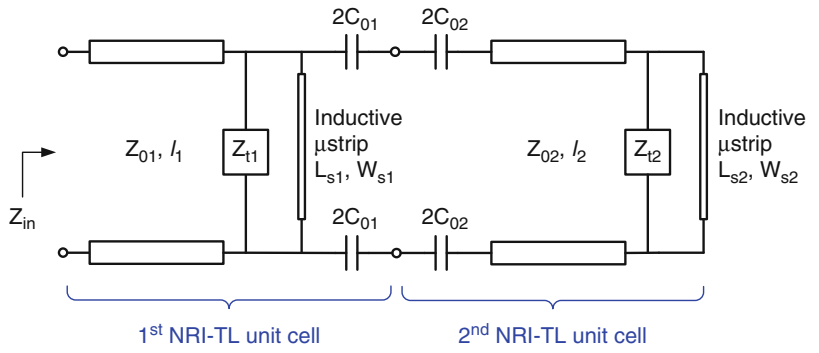

Fig. 36 Equivalent circuit of the NRI-TL dipole antenna of Fig. 35 (Antoniades and Eleftheriades 2012) © 2012 IEEE

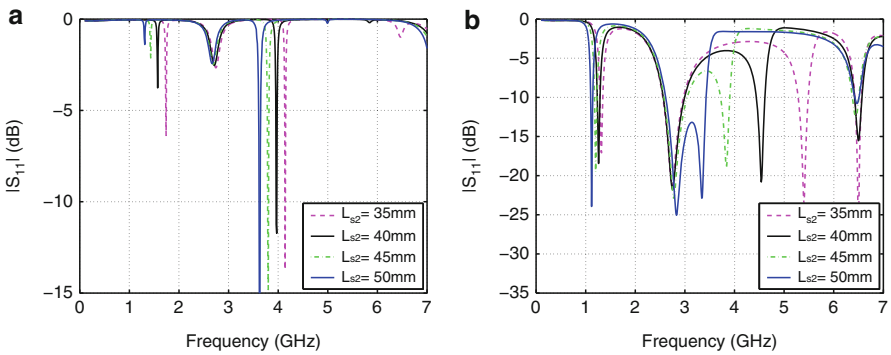

Fig. 37 (**a**) ADS simulated $|S_{11}|$ responses of the equivalent circuit of the NRI-TL dipole antenna of Fig. 36 for different values of the inductive strip length L_{s2}, using the equivalent circuit parameters extracted from Fig. 35. Parameters: $C_{01} = C_{02} = 0.2$ pF, $L_{s1} = 28$ mm, $W_{s1} = 0.1$ mm, $L_{s2} = 35 \rightarrow 50$ mm, $W_{s2} = 0.1$ mm, $Z_{01} = 312.6\ \Omega$, $Z_{02} = 355.2\ \Omega$, $l_1 = 13.6$ mm, $l_2 = 10.9$ mm, and $\beta l_1 = 49^\circ$ and $\beta l_2 = 39.2^\circ$ at 3 GHz. (**b**) HFSS simulated $|S_{11}|$ responses of the multiband NRI-TL metamaterial-loaded dipole antenna of Fig. 35 for different values of the bottom inductive strip length, $L_{s2} = 35 \rightarrow 50$ mm (Antoniades and Eleftheriades 2012) © 2012 IEEE

In this manner, the equivalent circuit of the NRI-TL dipole antenna shown in Fig. 36 is formed, which consists of two cascaded asymmetric NRI-TL metamaterial unit cells. Figure 37a shows the $|S_{11}|$ responses obtained from the Agilent-ADS circuit simulator for the equivalent circuit of the dipole antenna of Fig. 36 for different values of the inductive strip length L_{s2}. Note that while L_{s2} was varied, the total length of the antenna was kept at $L_2 = 50$ mm, and all of the other geometrical parameters were also kept constant. Figure 37b shows the full-wave simulated $|S_{11}|$ responses obtained from Ansoft-HFSS for the NRI-TL dipole antenna of Fig. 35 for different values of the bottom inductive strip L_{s2}. It can be observed that the general performance of the antenna equivalent circuit matches well with the

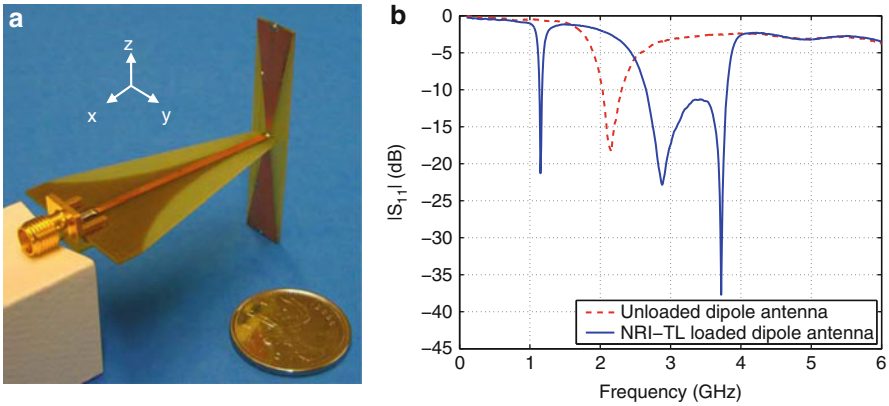

Fig. 38 Photograph of the NRI-TL metamaterial-loaded dipole antenna of Fig. 35 with $L_{s2} = 50$ mm, fed using a broadband transition. (**b**) Measured $|S_{11}|$ response of the antenna in (**a**), compared with the measured $|S_{11}|$ response of a reference unloaded dipole antenna fed using the same transition and with the same overall dimensions (Antoniades and Eleftheriades 2012) © 2012 IEEE

performance obtained from the full-wave HFSS results, thus validating the antenna equivalent circuit. It can also be observed that all of the antenna responses exhibit multiband characteristics, with four distinct resonances in the frequency range shown.

The fabricated prototype of the NRI-TL dipole antenna is shown in Fig. 38a. The measured $|S_{11}|$ response of the antenna is shown in Fig. 38b, compared to the measured $|S_{11}|$ response of a reference unloaded dipole antenna. It can be observed that the NRI-TL dipole antenna exhibits three distinct resonances corresponding to the $n = -1$, $n = -0$, and $n = +0$ resonances at 1.15 GHz, 2.88 GHz, and 3.72 GHz, with associated -10 dB bandwidths of 37 MHz and 1150 MHz, while the unloaded antenna exhibits only a single resonance at 2.15 GHz with a bandwidth of 275 MHz. Thus, the NRI-TL dipole antenna exhibits a 47 % reduction of the lowest resonant frequency compared to the reference unloaded dipole antenna. Furthermore, at 1.15 GHz, the length of the antenna, $L_2 = 50$ mm, is $0.19\lambda_0$, which represents a miniaturization factor of approximately two compared to the unloaded dipole antenna which has a length of $0.36\lambda_0$ at its resonant frequency of 2.15 GHz. Throughout the bands of operation, the antenna maintains a linear electric field polarization, and the measured gain and radiation efficiency vary from 0.11 dBi to 3.26 dBi and 49.5–95.6 %, respectively.

Metamaterial-Inspired Antennas

The numerous antenna designs that have been published on transmission-line-based metamaterials, as well as volumetric metamaterials based on split-ring resonators and wires, have also led to the creation of many antenna designs that are not metamaterial-based per se but that have been inspired by metamaterial concepts.

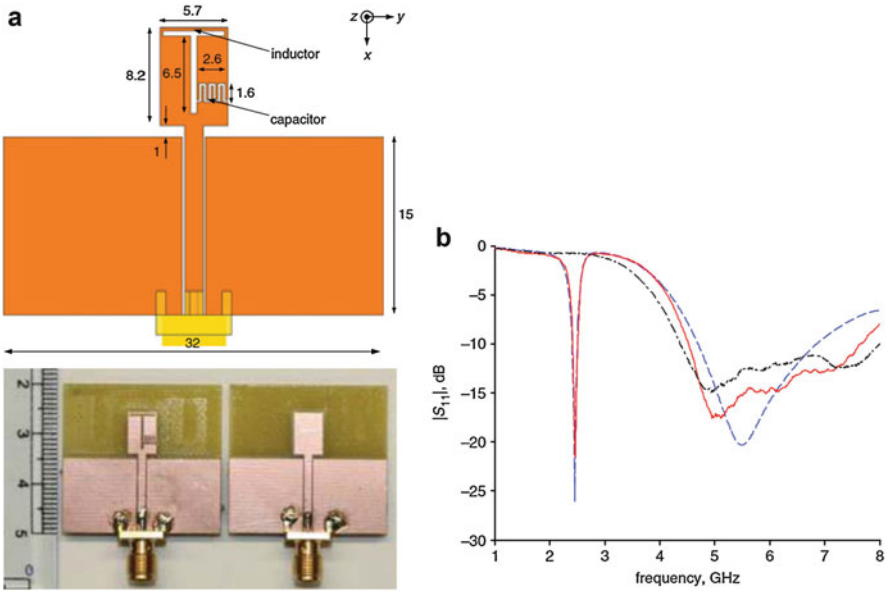

Fig. 39 (**a**) Dual-band metamaterial-inspired small monopole antenna for Wi-Fi applications, (**b**) $|S_{11}|$ responses: *red solid line*, measured results for the metamaterial-inspired antenna; *blue dashed line*, simulated results for the metamaterial-inspired antenna; and *black dash-dot line*, measured results for the unloaded monopole antenna (Zhu and Eleftheriades 2009a) © 2009 IET

Thus, metamaterials have provided a conceptual route for implementing many small resonant antennas (Zhu and Eleftheriades 2009a, 2010; He and Eleftheriades 2012; Ryan and Eleftheriades 2012).

A dual-band monopole antenna that employs metamaterial-inspired reactive loading is shown in Fig. 39a (Zhu and Eleftheriades 2009a). It comprises a two-arm fork-like CPW-fed monopole with a thin-strip inductor loaded on top of the monopole and an interdigital capacitor loaded on the right-side arm. Alternatively, it can be seen as a T-shaped slot cut out of the rectangular patch with a capacitor loaded on its right. This metamaterial-inspired loading enables the antenna to operate in two modes, covering the lower Wi-Fi band of 2.40–2.48 GHz and the upper Wi-Fi band of 5.15–5.80 GHz. The first mode is a monopole mode that operates at the upper Wi-Fi band, where the capacitor becomes a short circuit and the inductor becomes an open circuit. In addition to the monopole resonance at the upper Wi-Fi band, the metamaterial-inspired reactive loading introduces a second resonant mode the lower Wi-Fi band. At this frequency, the antenna no longer acts as a monopole along its axis, but rather as a slot along this axis.

Figure 39b shows the $|S_{11}|$ response of the metamaterial-inspired antenna, compared to the $|S_{11}|$ response of a reference unloaded antenna, where a dual-band performance of the metamaterial-inspired antenna can be clearly seen compared to the unloaded CPW-fed monopole antenna. The antenna exhibits a measured −10 dB bandwidth of 90 MHz at the lower Wi-Fi band from 2.42 to 2.51 GHz and a

bandwidth of 3.2 GHz from 4.52 to 7.72 GHz for the upper Wi-Fi band, with measured efficiencies of 89.2 % at 5.50 GHz and 64.0 % at 2.46 GHz and measured gains of 1.53 at 5.50 GHz and 0.71 at 2.46 GHz. The measured radiation patterns confirm the operation of the antenna as a conventional printed monopole in the upper band and a slot in the lower band.

Active Non-Foster Matching Networks for Small Antennas

Having described numerous passive antenna applications of transmission-line metamaterials in the previous section, the focus of this section shifts to active devices and specifically how these can be used in the design of compact and broadband antennas.

Antenna matching for receivers improves the received signal-to-noise ratio (SNR) and, for transmitters, enhances the radiated power efficiency. However, for electrically small antennas, because of their high-quality factor (high-Q), matching becomes a challenging task. In fact, a fundamental limit on the quality factor of a linearly polarized antenna with a radiation efficiency of η and an electrical size of ka, due to Wheeler (1947), Chu (1948), and Harrington (1960), is given by

$$Q = \eta\left(\frac{1}{k^3a^3} + \frac{1}{ka}\right). \tag{47}$$

The Chu limit above inversely relates the minimum achievable Q of an antenna to its electrical size; therefore, a small antenna assumes a high-Q. In turn, to match a high-Q electrically small antenna with a lossless passive matching network, the achievable matching bandwidth is constrained by another fundamental limit – namely, the Bode-Fano limit (Bode 1947; Fano 1950). This limit inversely relates the matching bandwidth to the Q of the load to be matched (here the antenna). All previously discussed small metamaterial antennas in this chapter were passive and thus subject to these matching limitations. The employment of active components, including reactive non-Foster elements, in the antenna or in the matching network, is sought to overcome either of these fundamental limits, and this will be the subject of this section. But, what are reactive non-Foster elements?

Zobel and Foster established that passive, non-dissipative, two-terminal reactances exhibit a positive slope with frequency (Zobel 1923; Foster 1924) – that is, the reactance X and the susceptance B of such networks for all frequencies satisfy:

$$\frac{\partial X}{\partial \omega} > 0 \quad \text{and} \quad \frac{\partial B}{\partial \omega} > 0\,. \tag{48}$$

Nonetheless, one can think of reactive elements with an anomalous behavior which, in contrast to Eq. 48, exhibit a negative slope with frequency; hence, they are called non-Foster reactive elements. For the reactances X_{NF} and susceptances B_{NF} of such networks and at least in part of the frequency spectrum:

$$\frac{\partial X_{NF}}{\partial \omega} < 0 \quad \text{and} \quad \frac{\partial B_{NF}}{\partial \omega} < 0\,. \tag{49}$$

Simple representative examples of non-Foster elements include negative capacitors and negative inductors.

Implementation of Reactive Non-Foster Elements

The networks employed for synthesizing non-Foster reactive elements must inevitably lack the condition of Foster's reactance theorem in Eq. 48. Therefore, these elements need to be designed using lossy (Mirzaei and Eleftheriades 2013c) or non-passive – i.e., active – networks (Linvill 1953). Traditionally, non-Foster reactive elements are implemented by two groups of circuits called negative impedance converters (NICs) and negative impedance inverters (NIIs). The operation of these circuits is schematically shown in Fig. 40.

According to Fig. 40a, NICs are two-port networks terminated at one port to an impedance, and looking into the other port, the negative of the termination impedance, with a scaling factor, is seen. For example, terminating such a network to a capacitor results in a negative capacitor. This property remains invariant by interchanging the input and output ports. Moreover, NICs change either the direction of the load current or invert the polarity of the load voltage, as seen from the input terminals. These two types are, respectively, named current-inversion NICs (INICs) and voltage-inversion NICs (VNICs). Furthermore, NIC circuits are usually open-circuit stable (OCS) at one port and short-circuit stable (SCS) at the other port (Brownlie 1966). A port is said to be OCS (SCS), if for any arbitrary passive impedance Z connected to the other port, the network obtained by open-circuiting (short-circuiting) the OSC (SCS) port remains stable. However, the knowledge of

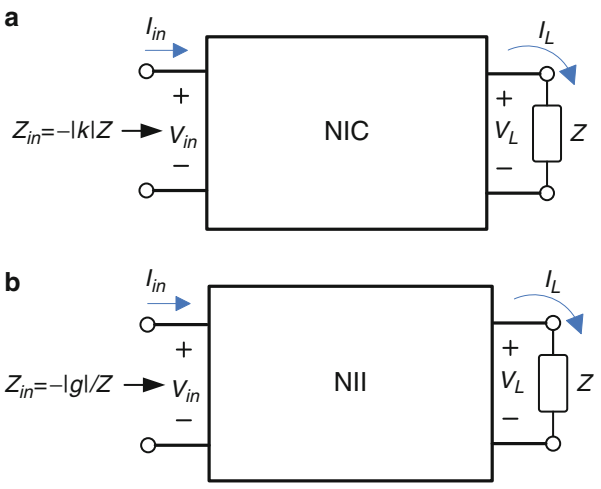

Fig. 40 The operation of (**a**) a negative impedance converter (NIC) and (**b**) a negative impedance inverters (NII) as two-port networks

OCS and SCS ports does not provide enough information about the stability of a given NIC circuit terminated to arbitrary loads except for an open or short circuit (Stearns 2011).

On the other hand, according to Fig. 40b, for terminated NIIs, the driving-point impedance at the input port is the inverse of the termination impedance, with a negative scaling factor. The operation of NIIs is similar to gyrators, but with a difference that NIIs have a negative gyration resistance (or conductance). As such, terminating an NII to a capacitor results in a negative inductor, as seen from the input port.

An inventory of some of the NIC circuits has been gathered in Sussman-Fort (1998) and Stearns (2011). These circuits include Linvill's single-ended and balanced VNICs (Linvill 1953), Larky's INIC (Larky 1956, 1957), Yanagisawa's INIC (Yanagisawa 1957), Sandberg and Nagata's INIC (Sandberg 1960; Nagata 1965), Hakim's VNICs and INIC (Hakim 1965), and Myers' VNICs and INICs (Myers 1965). In addition to these NIC circuits, a popular NII realization that uses two FET devices can be found in Brucher et al. (1995) and Kolev et al. (2001).

It should be noted that different NIC and NII circuits perform differently in terms of stability margin, noise, nonlinear behavior, and sensitivity to the transistor parameters. More importantly, the stability issues of a selected NIC or NII need to be carefully treated for a successful implementation of non-Foster reactive elements. The difficulty of this treatment becomes more obvious by noticing that all numerical port-based stability tests, including Rollet's k factor and μ test, which work sufficiently well in many microwave amplifier design tasks, widely fail in predicting the stability of non-Foster circuits (Stearns 2011, 2012, 2013).

A complete assessment of the network poles, by calculating the zeros of the network determinant (or its normalized determinant), can be a comprehensive way of determining the stability of non-Foster circuits, where a stable circuit must have no right-hand plane (RHP) poles (Bode 1947). In this regard, by building up on the concept of the normalized determinant function (NDF) and a simple way of calculating the NDF using "return ratios" (Bode 1947), Struble and Platzker implemented a method to evaluate the NDF using CAD tools (Struble and Platzker 1993; Platzker and Struble 1994). These days, the NDF method can be found integrated into commercial microwave simulation tools. The NDF analysis takes into account the effects of all loops in the network and is a reliable method. Nevertheless, it requires access and control over the internal linear-dependent sources in the models of the active devices used in the design. Therefore, when having access only to the S-parameters or the compiled linear models with no control over the active dependent sources inside the model, this method cannot be employed. In these situations, the Nyquist test applied to an accurate estimation of the loop gain in the feedback network can be a compelling choice (Middlebrook 1975; Tian et al. 2001).

More recently, an alternative approach for implementing reactive non-Foster elements using loss-compensated negative-group-delay (NGD) networks has been presented (Mirzaei and Eleftheriades 2013c). This approach naturally leads to stable implementations. It is developed by observing that non-Foster reactive elements and loss-compensated NGD networks influence propagating waves in a similar fashion.

Antennas with External Non-Foster Matching Networks

A brief review of the early applications of non-Foster reactive elements in small antenna matching networks can be found in Sussman-Fort and Rudish (2009). In this regard, the early works of Harris et al. (Harris and Myers 1968) and Perry (Albert 1973), which are briefly explained below, remarkably stand out. Other related works have been reported in Albee (1976), Bahr (1977), Sussman-Fort and Rudish (2009), Stearns (2011, 2013), White et al. (2012) and Xu et al. (2012). These applications can be explained with the help of a representative equivalent-circuit model.

An electrically small dipole or monopole antenna can be modeled with a simple series-*RC* equivalent circuit, where the radiation resistance is proportional to the square of frequency – i.e., $R_r = R_0(f/f_0)^2$. In this relation, R_0 represents the radiation resistance at a given frequency f_0.

Assuming that one has access to non-Foster inductances and capacitances, the antenna can be perfectly matched to the characteristic impedance of the system Z_0 as shown in Fig. 41a, where a negative capacitor tunes out the capacitance of the antenna and a step-up non-Foster T-transformer is used to cancel out the quadratic frequency dependence of R_r and match it to Z_0 (Skahill et al. 1998).

This scheme is too complicated, and considering all practical trade-offs, including difficulty of implementation, biasing, and noise, usually a much simpler approach involving only one series or parallel non-Foster capacitor at the terminals of the antenna is adopted. The scheme using a series floating negative capacitor is the same as the one in Fig. 41a without the non-Foster T-transformer. Using this approach, the antenna reactance is effectively eliminated, but the input resistance remains small and highly frequency dependent. Thereby, the antenna is not matched to the characteristic impedance of the system. Another scheme using one parallel capacitor, due to Harris et al. (Harris and Myers 1968), can be explained by converting the equivalent circuit of the small monopole antenna from a series *RC* to parallel *RC* as shown in Fig. 41b. This equivalent circuit is valid because of the large Q of an

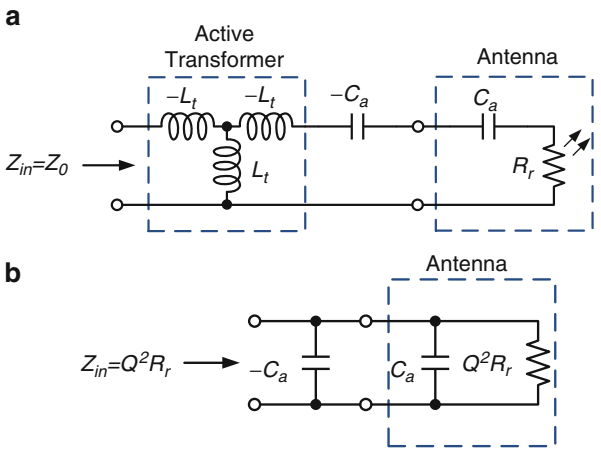

Fig. 41 (**a**) Perfect matching and (**b**) a more practical approach for matching an electrically small monopole using reactive non-Foster elements

electrically small antenna. Then, by placing a single-negative capacitor parallel to the terminals of the antenna, the reactive part of the input admittance can be effectively eliminated over a broad frequency range, but the remaining resistive part is highly frequency dependent, assumes very large values, and is not matched to the characteristic impedance of the system. Nevertheless, overall improvements in gain (Harris and Myers 1968; Albert 1973) and SNR (Sussman-Fort and Rudish 2009) in a wide frequency range have been reported using such simple schemes involving one series or parallel non-Foster capacitor.

These ideas of matching have attracted strong interest over the past few decades; however, the actual implementations have remained challenging due to the difficulty of realizing high-Q reactive non-Foster elements – mainly due to the stability issues which were previously discussed. In addition, in a practical implementation, other relevant issues, including the total power consumption, nonlinearity, and noise, need to be addressed.

Antennas with Embedded Non-Foster Matching Networks

Small antennas internally augmented by non-Foster reactive elements can provide a wider matching bandwidth at the input terminals compared to their passive counterparts. In fact, augmentation with reactive non-Foster elements is an extension to the antenna loading with passive Foster reactive elements which is widely employed for controlling the antenna parameters. Non-Foster reactive elements can potentially replace these Foster elements, leading to broadband operation. In particular, for broadband matching applications, the starting point is an antenna whose resonant frequency can be configured with a passive reactive Foster element, and herein a procedure is presented for replacing it with reactive non-Foster elements to make it broadband at the antenna terminals.

To explain the idea, it is assumed that a certain frequency-reconfigurable antenna around the resonant frequency can be modeled with a simple resonant equivalent circuit – say, a *series-RLC* circuit – and the resonant frequency of the antenna can be tuned using a variable capacitor C_t, as shown in Fig. 42a. It is also assumed that the antenna has a large radiation resistance close to the characteristic impedance of the system. This implies that, if electrically small, the antenna provides a very narrow bandwidth due to its large Q.

Subsequently, by assuming access to ideal non-Foster reactive elements, C_t can be replaced with a parallel combination of $-C_a$ and $-L_a$ to cancel out the antenna reactances, as shown in Fig. 42b, and the antenna will be matched over the entire frequency range where the model is valid. Note that such a simple model cannot represent the general complicated model of most antennas over a broad bandwidth, but it simply and sufficiently motivates the idea. Besides, for the actual design, as explained next in this section, the antenna tuning data, rather than its exact model, is required.

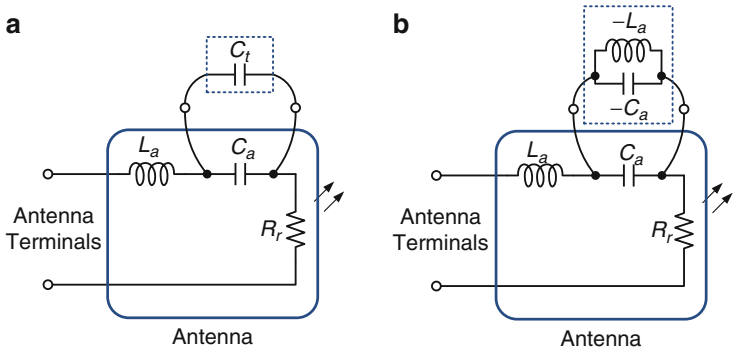

Fig. 42 (**a**) A simple series resonant model for an antenna for which the resonant frequency can be tuned using a tuning capacitor C_t. (**b**) C_t can ideally be replaced with a combination of non-Foster reactive elements to satisfy the resonance condition over a broad frequency range and to obtain a broadband matching at the antenna input terminals

Practical Design of Embedded Non-Foster Matching Networks

The design of an embedded non-Foster matching network can be performed totally based on the frequency reconfigurability of the underlying passive antenna. The design process leads to the synthesis of a two-terminal network which can replace the tuning capacitor or inductor, C_t or L_t, in the passive antenna to achieve a broadband operation. In this section, the design procedure is explained in three steps:

Step I: Selecting a Suitable Passive Antenna

Suitable antennas for the purpose of embedding non-Foster matching networks include frequency-reconfigurable (or frequency-agile) antennas for which the resonant frequency can be swept over a broad range using a variable capacitor C_t or an inductor L_t.

An example of such an antenna is shown in Fig. 43, which is a metamaterial-inspired monopole patch loaded with a varactor and fed by a coplanar waveguide (CPW), as shown in the section "Metamaterial-Inspired Antennas" (Mirzaei and Eleftheriades 2011b; Zhu and Eleftheriades 2009a). Other examples include a PIFA antenna (Di Nallo et al. 2007; Bit-Babik et al. 2007), as well as antennas presented in Zhu and Ziolkowski (2012a, b) and Ziolkowski et al. (2013). In fact, there is no limitation on the size of a suitable antenna as long as the non-Foster circuit can be fitted into the space provided. Therefore, this method can be attractive for matching electrically small antennas.

Step II: Obtaining the Frequency Reconfigurability and Tuning Behavior

The resonant frequency of the selected antenna can be tuned by the tuning element loading the antenna (C_t or L_t). The tuning behavior is a graph of $B_t = \omega C_t$ or

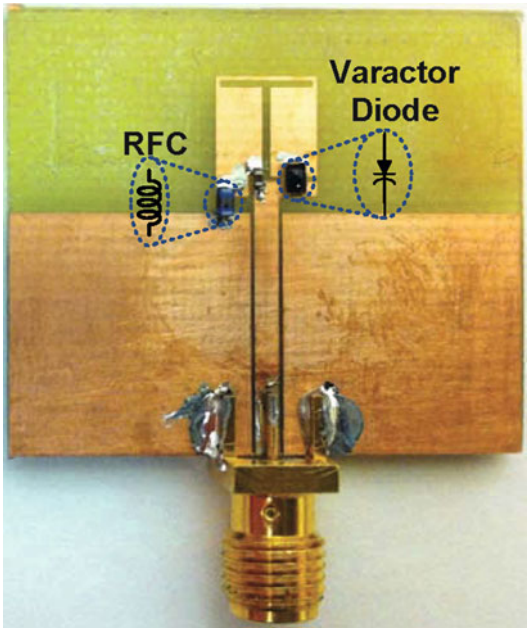

Fig. 43 Example of a metamaterial-inspired frequency-reconfigurable antenna, suited for embedding a non-Foster matching network (Mirzaei and Eleftheriades 2011b) © 2011 IEEE

$X_t = \omega L_t$ versus resonant frequencies ω, which can be measured or simulated over the desired bandwidth in some discrete frequencies for the passive antenna.

For example, a scaled version of the antenna from Fig. 43 and its tuning behavior are demonstrated in Fig. 44. This figure shows a large tuning bandwidth in the lower UHF band. The results in this graph are translated to a $B_t = \omega C_t$ versus ω graph in Fig. 44c, which exhibits a negative slope in accordance with the expected non-Foster behavior.

Step III: Fitting a Synthesizable Reactance Function to the Tuning Data and Calculating the Parameters of the Embedded Matching Network

In this step, an appropriate function has to be fitted to the graph representing the antenna tuning behavior. This function should represent a synthesizable reactance (susceptance function $B_t(\omega)$ or inductance function $X_t(\omega)$) using a combination of Foster and non-Foster elements. The idea here is to replace the tuning element C_t or L_t with a network that satisfies the resonance condition in a broad frequency range. As the sample graph in Fig. 44c illustrates, such a network synthesizes a non-Foster reactance at its terminals; hence, it can be implemented using a combination of non-Foster $-C$ and $-L$ and Foster C and L elements. The following criteria can be used to select the most appropriate non-Foster network among all possible combinations:

- Error function: that is, how closely the synthesized reactance follows the tuning data.
- Complexity: that is, how difficult the implementation of the network is. In particular, implementations with fewer non-Foster components are preferred.

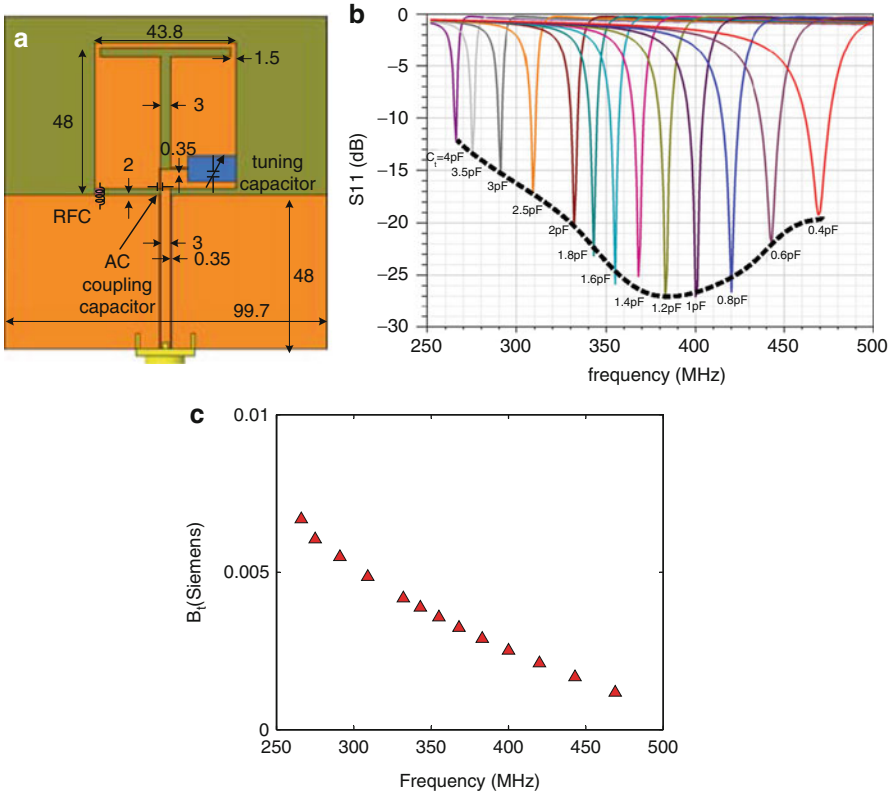

Fig. 44 (**a**) Dimensions of the frequency-reconfigurable antenna suitable for embedding a non-Foster matching network. (**b**) Simulation data using a finite-element field solver demonstrates that the resonant frequency of the antenna can be tuned by tuning the loading capacitor C_t. (**c**) Graph of the tuning susceptance $B_t = \omega C_t$ vs. frequency (Mirzaei and Eleftheriades 2013b) © 2013 IEEE

- Component values: that is, very large or very small values for the capacitors and inductors are not desirable.
- The sensitivity of the fitted curve to the value of the network elements: that is, how the antenna response changes if there exist some variation, dispersion, and error in the implementation of the network elements. This variation is more pronounced for the non-Foster elements, because of the more difficult implementation and limited quality factor.

After finalizing the non-Foster network selection, such a network can be implemented using appropriate NIC or NII circuits. Two implementation examples are shown in Fig. 45, where the antenna in Fig. 45a is the non-Foster version of the passive antennas shown in Figs. 43 and 44a. For the implementations in Fig. 45a, b, a 10 dB fractional bandwidth equal to 8.1 % and 8.2 % for return losses, respectively, around the center frequencies of 465 MHz and 306.7 MHz, has been obtained. For

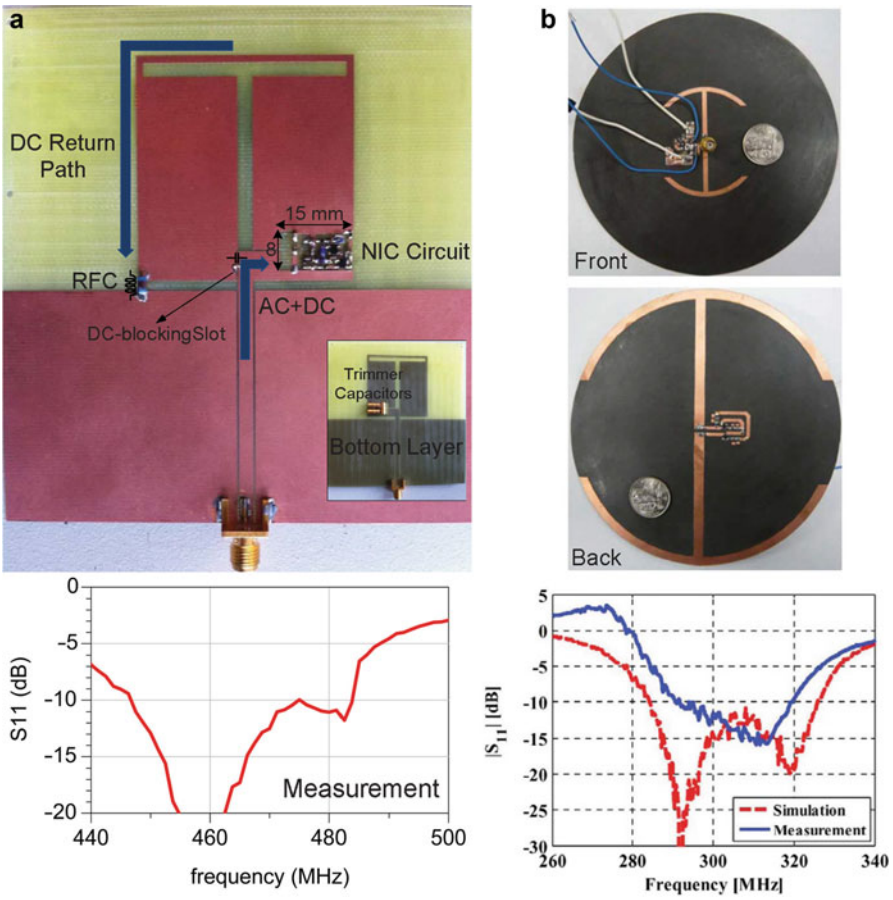

Fig. 45 (**a**) Metamaterial-inspired monopole antenna with an embedded non-Foster matching network (Mirzaei and Eleftheriades 2011a, 2013b), © 2011, 2013 IEEE. (**b**) Near-field resonant parasitic "Egyptian axe dipole" antenna with an embedded non-Foster matching network (Zhu and Ziolkowski 2012a) © 2012 IEEE

these two antennas, *ka* is equal to 0.486 and 0.506 at these center frequencies, where *k* is the free-space wave number and *a* is the radius of the smallest sphere circumscribing the antennas. According to a widely accepted criterion, $ka \approx 0.5$ marks the value below which the antennas can be regarded as electrically small; therefore, these two implementations approximately satisfy the condition for being electrically small. The bandwidth of 8.1 % of the antenna in Fig. 45a should be compared to the original 2.9 % bandwidth of the passive antenna shown in Fig. 44b. However, it should be noted that due to practical limitations (discussed below), a very broad bandwidth, similar to the dashed-line graph in Fig. 44b, cannot be achieved. Nonetheless, the actual implementations, exemplified above, show a

significant improvement in the antenna matching bandwidth (Mirzaei and Eleftheriades 2011a; Mirzaei and Eleftheriades 2013b; Zhu and Ziolkowski 2012a, b; Ziolkowski et al. 2013).

Promises and Challenges of Non-Foster Matching Networks for Antennas

The ideas of antennas with non-Foster matching networks have attracted strong interest over the past few decades; however, the actual implementations have remained challenging due to the difficulty of realizing high-Q reactive non-Foster elements – mainly due to the stability issues which were previously discussed. In practice, an unavoidable dispersion in the implementation of the reactive non-Foster elements, their limited quality factors, and sensitivity of the matching bandwidth to these variations tend to significantly limit the achievable bandwidth (Mirzaei and Eleftheriades 2013b). In addition, in a practical implementation, other relevant issues, including the total power consumption, nonlinearity, and noise, need to be addressed. For example, although a non-Foster matching network for a receiving antenna improves the received signal level by improving the matching bandwidth, it also increases the noise level. For such an application, the achievable signal-to-noise ratio at the antenna terminals, rather than the actual matching bandwidth, will utterly matter.

Some of these challenges, including the stability and dispersion issues, can be addressed by a recently proposed method for implementing reactive non-Foster elements using loss-compensated negative-group-delay (NGD) networks (Mirzaei and Eleftheriades 2013c). In this kind of non-Foster elements, the negative slope of the reactance is synthesized in a lossy NGD network, and the losses are compensated separately by amplification. This is in contrast to the traditional NIC and NII networks where the active and passive parts are intertwined in a circuit with positive feedback loops that tend to destabilize the circuit. The full application of this kind of non-Foster elements is due to further development of bilateral amplification blocks. Nevertheless, when using regular unilateral amplifiers, a special unilateral version of non-Foster reactances can be obtained which can prove useful for specific applications (Mirzaei and Eleftheriades 2013a, c, 2014). For example, a unilateral floating negative capacitor can be useful for matching applications, for which a -2.4 pF implementation is shown in Fig. 46 in the frequency range of 1–1.5 GHz. The experimental results show that a low-dispersion unilateral capacitor with a good quality factor has been obtained in this bandwidth.

Conclusion

In this chapter, the theory and operation of transmission-line-based metamaterials has been presented, and it has been shown how this can be used to design various types of passive and active antennas. The transmission-line-based metamaterial

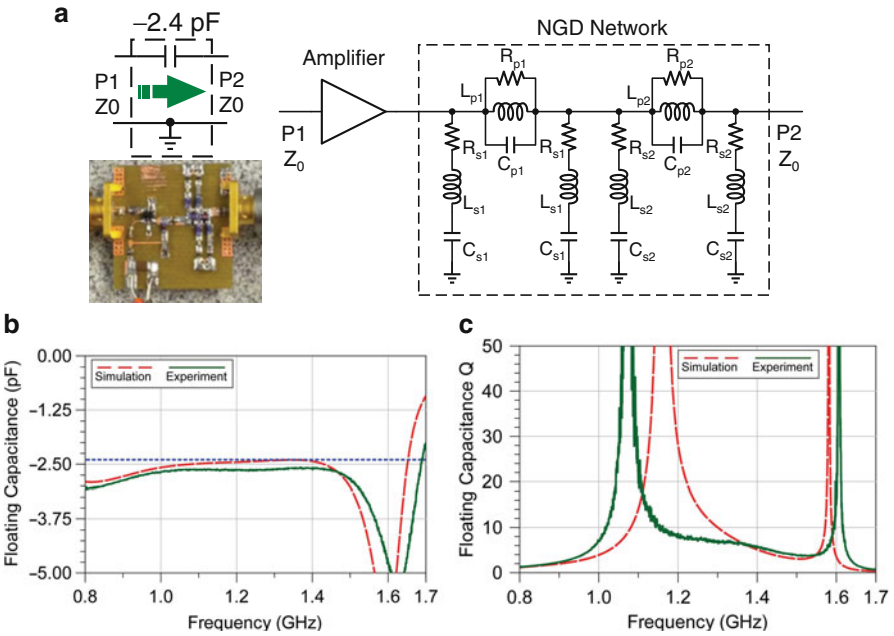

Fig. 46 (**a**) Photograph and schematic of a fabricated unilateral floating capacitor made by cascading an NGD network and an amplifier. (**b**) Floating capacitance value. (**c**) Q, extracted from the S-parameters, shows a low-dispersion capacitance with a good quality factor (Mirzaei and Eleftheriades 2013c) © 2013 IEEE

structure was formed by periodically loading a conventional microwave transmission line with lumped-element series capacitors and shunt inductors. The resulting structure was termed a negative-refractive-index transmission-line (NRI-TL) metamaterial, and it was shown through a dispersion analysis that it can support both backward waves in the left-handed NRI region and forward waves in the right-handed positive-refractive-index (PRI) region. Furthermore, it can support standing waves with a zero propagation constant at the transition point between the NRI and PRI regions.

The rich propagation characteristics of NRI-TL metamaterials form the underlying basis for their use in many antenna applications, including leaky-wave antennas, compact resonant antennas, and multiband antennas. The resonant characteristics of the NRI-TL metamaterial structures were analyzed with the aid of a dispersion diagram, enabling one to clearly visualize how these structures can be designed to offer multiband responses whose resonant frequencies are not harmonically related while offering large degrees of miniaturization.

Specifically, it was outlined how effective radiation can be achieved from a metamaterial structure when its total electrical length is equal to integer multiples of π, including zero and negative integer values, referred to as the zeroth-order and negative-order resonant modes, respectively. The individual resonant frequencies

can be adjusted by changing the values of the reactive loading of the transmission line through a "dispersion engineering" process, therefore allowing the resonances to be placed at multiple nonharmonic frequencies. Subsequently, it was demonstrated how NRI-TL metamaterial antennas can be designed that are independent of their overall physical size, which is in contrast to conventional resonant antennas whose size is on the order of $\lambda/2$. This useful property allows compact metamaterial antenna designs to be achieved at a fraction of the size of conventional antennas by employing the zeroth-order and negative-order modes of the NRI-TL metamaterials.

Design equations for rapid prototyping have been presented, allowing an antenna designer to easily determine the loading-element values required for a metamaterial antenna with certain volume and system impedance constraints. Guidelines have also been provided for the physical realization of the loading elements, either in fully printed form or using off-the-shelf surface-mount chip components.

In order to highlight the advantages that transmission-line metamaterials have to offer in the design of antennas, a number of passive metamaterial antenna applications have been presented. These include examples of zeroth-order resonant antennas, negative-order resonant antennas, epsilon-negative antennas, mu-negative antennas, metamaterial dipole antennas, and metamaterial-inspired antennas.

In the concluding section, active non-Foster matching networks for small antennas have been presented, and it has been demonstrated how these can be applied to metamaterial-inspired antennas. The implementation of reactive non-Foster elements was presented using two networks: negative impedance converters (NICs) and negative impedance inverters (NIIs). The limitations of antennas that employ external non-Foster matching networks were described, followed by the benefits of using antennas with embedded non-Foster matching networks. Subsequently, a practical design procedure for antennas with embedded non-Foster matching networks was presented, and it was shown how this can be applied to a specific metamaterial antenna design.

Finally, in order to overcome some of the limitations faced by conventional reactive non-Foster elements, including stability, dispersion, and achievable bandwidth, a new method of implementing reactive non-Foster elements using loss-compensated negative-group-delay (NGD) networks was presented. Using this method, it was demonstrated that a low-dispersion unilateral negative capacitor with a good quality factor can be achieved over a wide bandwidth.

Cross-References

See also the following chapters in the Handbook of Antenna Technology:

► Metamaterials and Antennas
► Small Antennas

References

Albee TK (1976) Broadband VLF loop antenna system. US Patent 3,953,799

Albert KP (1973) Broadband antennas systems realized by active circuit conjugate impedance matching. Master's thesis, Naval Postgraduate School, Monterey. Acc. No. AD769800

Alu A, Bilotti F, Engheta N, Vegni L (2007) Subwavelength, compact, resonant patch antennas loaded with metamaterials. IEEE Trans Antennas Propag 55(1):13–25

Antoniades MA (2004) Compact linear metamaterial phase shifters for broadband applications. Master's thesis, University of Toronto, Toronto

Antoniades MA (2009) Microwave devices and antennas based on negative-refractive-index transmission-line metamaterials. Ph D thesis, University of Toronto, Toronto

Antoniades MA, Eleftheriades GV (2003) Compact linear lead/lag metamaterial phase shifters for broadband applications. IEEE Antennas Wirel Propag Lett 2(1):103–106

Antoniades MA, Eleftheriades GV (2008a) A CPS leaky-wave antenna with reduced beam squinting using NRI-TL metamaterials. IEEE Trans Antennas Propag 56(3):708–721

Antoniades MA, Eleftheriades GV (2008b) A folded-monopole model for electrically small NRI-TL metamaterial antennas. IEEE Antennas Wirel Propag Lett 7:425–428

Antoniades MA, Eleftheriades GV (2009) A broadband dual-mode monopole antenna using NRI-TL metamaterial loading. IEEE Antennas Wirel Propag Lett 8:258–261

Antoniades MA, Eleftheriades GV (2011a) A multi-band NRI-TL metamaterial-loaded bow-tie antenna. In: Proceedings IEEE AP-S international symposium on antennas and propagation, Spokane, pp 1−4

Antoniades MA, Eleftheriades GV (2011b) A NRI-TL metamaterial-loaded bow-tie antenna. In: Proceedings fifth European conference on antennas and propagation, Rome, pp 1−4

Antoniades MA, Eleftheriades GV (2012) Multiband compact printed dipole antennas using NRI-TL metamaterial loading. IEEE Trans Antennas Propag 60(12):5613–5626

Antoniades MA, Abbosh A, Razali AR (2013) A compact multiband NRI-TL metamaterial-loaded planar antenna for heart failure monitoring. In: Proceedings IEEE AP-S international symposium on antennas and propagation, Orlando, pp 1372−1373

Baek S, Lim S (2009) Miniaturised zeroth-order antenna on spiral slotted ground plane. Electron Lett 45(20):1012–1014

Bahr A (1977) On the use of active coupling networks with electrically small receiving antennas. IEEE Trans Antennas Propag 25(6):841–845

Balanis CA (ed) (2008) Modern antenna handbook. Wiley, Hoboken

Balanis CA (2012) Advanced engineering electromagnetics, 2nd edn. Wiley, New York

Bertin G, Bilotti F, Piovano B, Vallauri R, Vegni L (2012) Switched beam antenna employing metamaterial-inspired radiators. IEEE Trans Antennas Propag 60(8):3583–3593

Best SR (2005) The performance properties of electrically small resonant multiple-arm folded wire antennas. IEEE Antennas Propag Mag 47(4):13–27

Best SR (2014) The significance of composite right/left-handed (CRLH) transmission-line theory and reactive loading in the design of small antennas. IEEE Antennas Propag Mag 56(4):15–33

Bilotti F, Alu A, Vegni L (2008) Design of miniaturized metamaterial patch antennas with μ-negative loading. IEEE Trans Antennas Propag 56(6):1640–1647

Bit-Babik G, Di Nallo C, Svigelj J, Faraone A (2007) Small wideband antenna with non-Foster loading elements. In: Proceedings International conference on electromagnetics in advanced applications (ICEAA), Torino, Italy, pp 105−107

Bode HW (1947) Network analysis and feedback amplifier design. D. Van Nostrand, New York

Brownlie J (1966) On the stability properties of a negative impedance converter. IEEE Trans Circuit Theory 13(1):98–99

Brucher A, Meunier PH, Jarry B, Guilion P, Sussman-Fort SE (1995) Negative resistance monolithic circuits for microwave planar active filter losses compensation. In: Proceedings 25th European microwave conference (EuMC), vol 2, Bologna, Italy, pp 910−915

Caloz C, Itoh T (2003) Novel microwave devices and structures based on the transmission line approach of meta-materials. In: Proceedings IEEE MTT-S international microwave symposium, vol 1, Philadelphia, pp 195–198
Caloz C, Itoh T (2006) Electromagnetic metamaterials: transmission line theory and microwave applications. Wiley, Hoboken
Capolino F (ed) (2009) Metamaterials handbook: applications of metamaterials. CRC Press, Boca Raton
Chu LJ (1948) Physical limitations of omni-directional antennas. J Appl Phys 19(12):1163–1175
Coilcraft Inc (2015) 0402CS (1005) Ceramic chip inductors. http://www.coilcraft.com/0402cs.cfm. Document 198-1. Accessed 1 Feb 2015
Collin RE (1992) Foundations for microwave engineering, 2nd edn. McGraw-Hill, New York
Cui TJ, Smith DR, Liu R (eds) (2010) Metamaterials: theory, design, and applications. Springer, New York
Di Nallo C, Bit-Babik G, Faraone A (2007) Wideband antenna using non-Foster loading elements. In: Proceedings IEEE AP-S international symposium antennas on propagation, Honolulu, HI, USA, pp 4501–4504
Dong Y, Itoh T (2010) Miniaturized substrate integrated waveguide slot antennas based on negative order resonance. IEEE Trans Antennas Propag 58(12):3856–3864
Dong Y, Toyao H, Itoh T (2011) Compact circularly-polarized patch antenna loaded with metamaterial structures. IEEE Trans Antennas Propag 59(11):4329–4333
Eleftheriades GV (2007) Enabling RF/microwave devices using negative-refractive-index transmission-line (NRI-TL) metamaterials. IEEE Antennas Propag Mag 49(2):34–51
Eleftheriades GV (2009) EM transmission-line metamaterials. Mater Today 12:30–41
Eleftheriades GV, Balmain KG (eds) (2005) Negative-refraction metamaterials: fundamental principles and applications. Wiley, Hoboken
Eleftheriades GV, Iyer AK, Kremer PC (2002) Planar negative refractive index media using periodically L-C loaded transmission lines. IEEE Trans Microw Theory Tech 50(12):2702–2712
Eleftheriades GV, Grbic A, Antoniades MA (2004) Negative-refractive-index transmission-line metamaterials and enabling electromagnetic applications. In: Proceedings IEEE AP-S international symposium antennas on propagation, vol 2, Monterey, pp 1399–1402
Eleftheriades GV, Antoniades MA, Qureshi F (2007) Antenna applications of negative-refractive-index transmission-line structures. IET Microw Antennas Propag 1(1):12–22
Elek F, Eleftheriades GV (2005) A two-dimensional uniplanar transmission-line metamaterial with a negative index of refraction. New J Phys 7(163):1–18
Engheta N, Ziolkowski RW (eds) (2006) Metamaterials: physics and engineering explorations. Wiley, Hoboken
Fano RM (1950) Theoretical limitations on the broadband matching of arbitrary impedances. J Franklin Inst 249(1):57–83
Foster RM (1924) A reactance theorem. Bell Syst Tech J 3:259–267
Goubau G (1976) Multi-element monopole antennas. In: Proceedings ECOM-ARO workshop on electrically small antennas, Ft. Monmouth, pp 63–67
Grbic A, Eleftheriades GV (2002) A backward-wave antenna based on negative refractive index L-C networks. In: Proceedings IEEE AP-S international symposium antennas on propagation, vol 4, San Antonio, pp 340–343
Grbic A, Eleftheriades GV (2004) Overcoming the diffraction limit with a planar left-handed transmission-line lens. Phys Rev Lett 92(11):117403
Hakim SS (1965) Some new negative-impedance convertors. Electron Lett 1(1):9–10
Harrington RF (1960) Effect of antenna size on gain, bandwidth and efficiency. J Res Natl Bur Stand 64D(1):1–12
Harris AD, Myers GA (1968) An investigation of broadband miniature antennas. Technical report AD0677320, Naval Postgraduate School, Monterey
Hashemi MRM, Itoh T (2011) Evolution of composite right/left-handed leaky-wave antennas. Proc IEEE 99(10):1746–1754

He Y, Eleftheriades GV (2012) Metamaterial-inspired wideband circular monopole antenna. In: Proceedings IEEE AP-S international symposium antennas on propagation, Chicago, pp 1–2
Herraiz-Martinez FJ, Gonzalez-Posadas V, Garcia-Munoz LE, Segovia-Vargas D (2008a) Multifrequency and dual-mode patch antennas partially filled with left-handed structures. IEEE Trans Antennas Propag 56(8):2527–2539
Herraiz-Martinez FJ, Segovia-Vargas D, Garcia-Munoz LE, Gonzalez-Posadas V (2008b) Dual-frequency printed dipole loaded with meta-material particles. In: Proceedings IEEE AP-S international symposium antennas on propagation, San Diego, pp 1–4
Herraiz-Martinez FJ, Hall PS, Liu Q, Segovia-Vargas D (2011) Left-handed wire antennas over ground plane with wideband tuning. IEEE Trans Antennas Propag 59(5):1460–1471
Iizuka H, Hall PS (2007) Left-handed dipole antennas and their implementations. IEEE Trans Antennas Propag 55(55):1246–1253
Islam R, Eleftheriades GV (2007) Miniaturized microwave components and antennas using negative-refractive-index transmission-line (NRI-TL) metamaterials. Metamaterials (Elsevier) 1:53–61
Islam R, Eleftheriades GV (2012) A review of the microstrip/negative-refractive-index transmission-line coupled-line couplers. IET Microw Antennas Propag 6(1):31–45
Iyer AK, Eleftheriades GV (2004) Leaky-wave radiation from planar negative-refractive-index transmission-line metamaterials. In: Proceedings IEEE MTT-S international microwave symposium, vol 2, Forth Worth, pp 1411–1414
Iyer AK, Kremer PC, Eleftheriades GV (2003) Experimental and theoretical verification of focusing in a large, periodically loaded transmission line negative refractive index metamaterial. Opt Express 11(7):696–708
Jin P, Ziolkowski RW (2010) Linearly and circularly polarized, planar, electrically small, metamaterial-engineered dipole antennas. In: Proceedings IEEE AP-S international symposium antennas on propagation, Toronto, pp 1–4
Kim J, Kim G, Seong W, Choi J (2009) A tunable internal antenna with an epsilon negative zeroth order resonator for DVB-H service. IEEE Trans Antennas Propag 57(12):4014–4017
Kolev S, Delacressonniere B, Gautier J-L (2001) Using a negative capacitance to increase the tuning range of a varactor diode in MMIC technology. IEEE Trans Microw Theory Tech 49(12):2425–2430
Lai A, Itoh T, Caloz C (2004) Composite right/left-handed transmission line metamaterials. IEEE Microw Mag 5(3):34–50
Lai A, Leong KMKH, Itoh T (2007) Infinite wavelength resonant antennas with monopolar radiation pattern based on periodic structures. IEEE Trans Antennas Propag 55(3):868–876
Larky AI (1956) Negative-impedance converter design. Ph D thesis, Stanford University
Larky AI (1957) Negative-impedance converters. IRE Trans Circuit Theory 4(3):124–131
Lee H-M (2011) A compact zeroth-order resonant antenna employing novel composite right/left-handed transmission-line unit-cells structure. IEEE Antennas Wirel Propag Lett 10:1377–1380
Lee J-G, Lee J-H (2007) Zeroth order resonance loop antenna. IEEE Trans Antennas Propag 55(3):994–997
Lee C-J, Leong KMKH, Itoh T (2006) Composite right/left-handed transmission line based compact resonant antennas for RF module integration. IEEE Trans Antennas Propag 54(8):2283–2291
Linvill JG (1953) Transistor negative-impedance converters. Proc IRE 41(6):725–729
Liu Q, Hall PS, Borja AL (2009) Efficiency of electrically small dipole antennas loaded with left-handed transmission lines. IEEE Trans Antennas Propag 57(10):3009–3017
Liu C-C, Chi P-L, Lin Y-D (2012) Compact zeroth-order resonant antenna based on dual-arm spiral configuration. IEEE Antennas Wirel Propag Lett 11:318–321
Liu W, Chen ZN, Qing X (2014) Metamaterial-based low-profile broadband mushroom antenna. IEEE Trans Antennas Propag 62(3):1165–1172
Marques R, Martin F, Sorolla M (2007) Metamaterials with negative parameters: theory, design and microwave applications. Wiley, Hoboken

Mehdipour A, Eleftheriades GV (2014) Leaky-wave antennas using negative-refractive-index transmission-line metamaterial supercells. IEEE Trans Antennas Propag 62(8):3929–3942
Middlebrook RD (1975) Measurement of loop gain in feedback systems. Int J Electron 38(4):485–512
Mirzaei H, Eleftheriades GV (2011a) A wideband metamaterial-inspired compact antenna using embedded non-Foster matching. In: Proceedings IEEE AP-S international symposium antennas on propagation, Spokane, WA, USA, pp 1950–1953
Mirzaei H, Eleftheriades GV (2011b) A compact frequency-reconfigurable metamaterial-inspired antenna. IEEE Antennas Wirel Propag Lett 10:1154–1157
Mirzaei H, Eleftheriades GV (2013a) Unilateral non-Foster elements using loss-compensated negative-group-delay networks for guided-wave applications. In: Proceedings IEEE MTT-S international microwave symposium, Seattle, WA, USA, pp 1–4
Mirzaei H, Eleftheriades GV (2013b) A resonant printed monopole antenna with an embedded non-Foster matching network. IEEE Trans Antennas Propag 61(11):5363–5371
Mirzaei H, Eleftheriades GV (2013c) Realizing non-Foster reactive elements using negative-group-delay networks. IEEE Trans Microw Theory Tech 61(12):4322–4332
Mirzaei H, Eleftheriades GV (2014) Realizing non-Foster reactances using negative-group-delay networks and applications to antennas. In: Proceedings IEEE radio wireless symposium (RWS), Newport Beach, CA, USA, pp 58−60
Myers BR (1965) New subclass of negative-impedance convertors with improved gain-product sensitivities. Electron Lett 1(3):68–70
Nagata M (1965) A simple negative impedance circuit with no internal bias supplies and good linearity. IEEE Trans Circuit Theory 12(3):433–434
Niu B-J, Feng Q-Y (2013) Bandwidth enhancement of CPW-fed antenna based on epsilon negative zeroth- and first-order resonators. IEEE Antennas Wirel Propag Lett 12:1125–1128
Niu B-J, Feng Q-Y, Shu P-L (2013) Epsilon negative zeroth- and first-order resonant antennas with extended bandwidth and high efficiency. IEEE Trans Antennas Propag 61(12):5878–5884
Park B-C, Lee J-H (2011) Omnidirectional circularly polarized antenna utilizing zeroth-order resonance of epsilon negative transmission line. IEEE Trans Antennas Propag 59(7):2717–2721
Park J-H, Ryu Y-H, Lee J-G, Lee J-H (2007) Epsilon negative zeroth-order resonator antenna. IEEE Trans Antennas Propag 55(12):3710–3712
Park JH, Ryu Y-H, Lee J-H (2010) Mu-zero resonance antenna. IEEE Trans Antennas Propag 58(6):1865–1875
Pendry JB (2000) Negative refraction makes a perfect lens. Phys Rev Lett 85(18):3966–3969
Pendry JB, Schurig D, Smith DR (2006) Controlling electromagnetic fields. Science 312:1780–1782
Platzker A, Struble W (1994) Rigorous determination of the stability of linear n-node circuits from network determinants and the appropriate role of the stability factor K of their reduced two-ports. In: Proceedings 3rd international workshop on integrated nonlinear microwave and millimeterwave circuits, Duisburg, Germany, pp 93−107
Qureshi F, Antoniades MA, Eleftheriades GV (2005) A compact and low-profile metamaterial ring antenna with vertical polarization. IEEE Antennas Wirel Propag Lett 4:333–336
Ryan CGM, Eleftheriades GV (2012) Two compact, wideband, and decoupled meander-line antennas based on metamaterial concepts. IEEE Antennas Wirel Propag Lett 11:1277–1280
Sanada A, Caloz C, Itoh T (2004) Planar distributed structures with negative refractive index. IEEE Trans Microw Theory Tech 52(4):1252–1263
Sandberg IW (1960) Synthesis of driving-point impedances with active RC networks. Bell Syst Tech J 39(4):947–962
Schelkunoff SA, Friis HT (1952) Antennas: theory and practice. Wiley, New York, p 309
Schussler M, Freese J, Jakoby R (2004a) Design of compact planar antennas using LH-transmission lines. In: Proceedings IEEE MTT-S international microwave symposium, vol 1, Forth Worth, pp 209−212

Schussler M, Oertel M, Fritsche C, Freese J, Jakoby R (2004b) Design of periodically L-C loaded patch antennas. In: Proceedings 27th ESA antenna technology workshop on innovative periodic antennas, Santiago de Compostela

Sievenpiper D, Lijun Z, Broas RFJ, Alexopoulos NG, Yablonovitch E (1999) High-impedance electromagnetic surfaces with a forbidden frequency band. IEEE Trans Microw Theory Tech 47(11):2059–2074

Skahill G, Rudish RM, Piero JA (1998) Electrically small, efficient, wideband, low-noise antenna elements. In: Proceedings antenna application symposium, Monticello, IL, USA, pp 214−231

Stearns SD (2011) Non-Foster circuits and stability theory. In: Proceedings IEEE AP-S international symposium antennas on propagation, Spokane, WA, USA, pp 1942–1945

Stearns SD (2012) Incorrect stability criteria for non-Foster circuits. In: Proceedings IEEE AP-S international symposium antennas on propagation, Chicago, IL, USA, pp 1–4

Stearns SD (2013) Circuit stability theory for non-Foster circuits. In: Proceedings IEEE MTT-S international microwave symposium, Seattle, WA, USA, pp 1–4

Struble W, Platzker A (1993) A rigorous yet simple method for determining stability of linear N-port networks [and MMIC application]. In: Proceedings GaAs IC symposium digest, San Jose, CA, USA, pp 251−254

Sussman-Fort SE (1998) Gyrator-based biquad filters and negative impedance converters for microwaves. Int J RF Microw Comput Aided Eng 8(2):86–101

Sussman-Fort SE, Rudish RM (2009) Non-Foster impedance matching of electrically-small antennas. IEEE Trans Antennas Propag 57(8):2230–2241

Tian M, Visvanathan V, Hantgan J, Kundert K (2001) Striving for small-signal stability. IEEE Circuits Devices Mag 17(1):31–41

Tretyakov SA, Ermutlu M (2005) Modeling of patch antennas partially loaded with dispersive backward-wave materials. IEEE Antennas Wirel Propag Lett 4:266–269

Vaughan R, Bach-Andersen J (2003) Channels, propagation and antennas for mobile communications. IEE, London

Veselago VG (1968) The electrodynamics of substances with simultaneously negative values of $\in$ and μ. Soviet Phys Uspekhi 10(4):509–514

Volakis JL (2007) Antenna engineering handbook, 4th edn. McGraw-Hill Professional, New York

Volakis JL, Chen C-C, Fujimoto K (2010) Small antennas: miniaturization techniques & applications. McGraw-Hill Professional, New York

Wang C, Hu B-J, Zhang X-Y (2010) Compact triband patch antenna with large scale of frequency ratio using CRLH-TL structures. IEEE Antennas Wirel Propag Lett 9:744–747

Wei K, Zhang Z, Feng Z (2012a) Design of a wideband horizontally polarized omnidirectional printed loop antenna. IEEE Antennas Wirel Propag Lett 11:49–52

Wei K, Zhang Z, Feng Z, Iskander MF (2012b) A MNG-TL loop antenna array with horizontally polarized omnidirectional patterns. IEEE Trans Antennas Propag 60(6):2702–2710

Wheeler HA (1947) Fundamental limitations of small antennas. Proc IRE 35(12):1479–1484

White CR, Colburn JS, Nagele RG (2012) A non-Foster VHF monopole antenna. IEEE Antennas Wirel Propag Lett 11:584–587

Xu ZA, White CR, Yung MW, Yoon YJ, Hitko DA, Colburn JS (2012) Non-Foster circuit adaptation for stable broadband operation. IEEE Microw Wirel Compon Lett 22(11):571–573

Yanagisawa T (1957) RC active networks using current inversion type negative impedance converters. IRE Trans Circuit Theory 4(3):140–144

Zedler M, Eleftheriades GV (2011) Anisotropic transmission-line metamaterials for 2-D transformation optics applications. Proc IEEE 99(10):1634–1645

Zhu J, Eleftheriades GV (2009a) Dual-band metamaterial-inspired small monopole antenna for WiFi applications. Electron Lett 45(22):1104–1106

Zhu J, Eleftheriades GV (2009b) A compact transmission-line metamaterial antenna with extended bandwidth. IEEE Antennas Wireless Propag Lett 8:295–298

Zhu J, Eleftheriades GV (2010) A simple approach for reducing mutual coupling in two closely spaced metamaterial-inspired monopole antennas. IEEE Antennas Wireless Propag Lett 9:379–382

Zhu N, Ziolkowski RW (2012a) Broad-bandwidth, electrically small antenna augmented with an internal non-Foster element. IEEE Antennas Wireless Propag Lett 11:1116–1120

Zhu N, Ziolkowski RW (2012b) Design and measurements of an electrically small, broad bandwidth, non-Foster circuit-augmented protractor antenna. Appl Phys Lett 101(2):024107

Zhu J, Antoniades MA, Eleftheriades GV (2010) A compact tri-band monopole antenna with single-cell metamaterial loading. IEEE Trans Antennas Propag 58(4):1031–1038

Ziolkowski RW, Erentok A (2006) Metamaterial-based efficient electrically small antennas. IEEE Trans Antennas Propag 54(7):2113–2130

Ziolkowski RW, Tang M-C, Zhu N (2013) An efficient, broad bandwidth, high directivity, electrically small antenna. Microw Opt Tech Lett 55(6):1430–1434

Zobel OJ (1923) Theory and design of uniform and composite electric wave-filters. Bell Syst Tech J 2(1):1–46